SEARCH FOR PRODUCTION OF A HIGGS BOSON AND A SINGLE TOP QUARK IN MULTILEPTON FINAL STATES IN pp COLLISIONS AT $\sqrt{s} = 13$ TeV.

by

Jose Andres Monroy Montañez

A DISSERTATION

Presented to the Faculty of

The Graduate College at the University of Nebraska

In Partial Fulfilment of Requirements

For the Degree of Doctor of Philosophy

Major: Physics and Astronomy

Under the Supervision of Kenneth Bloom and Aaron Dominguez

Lincoln, Nebraska

July, 2018

SEARCH FOR PRODUCTION OF A HIGGS BOSON AND A SINGLE TOP QUARK IN MULTILEPTON FINAL STATES IN pp COLLISIONS AT $\sqrt{s} = 13$ TeV.

Jose Andres Monroy Montañez, Ph.D.

University of Nebraska, 2018

Adviser: Kenneth Bloom and Aaron Dominguez

Table of Contents

List of Figures

List of Tables

Chapter 1

INTRODUCTION

Chapter 2

Theoretical approach

2.1 Introduction

The physical description of the universe is a challenge that physicists have faced by making theories that refine existing principles and proposing new ones in an attempt to embrace emerging facts and phenomena.

At the end of 1940s Julian Schwinger [1] and Richard P. Feynman [2], based in the work of Sin-Itiro Tomonaga [3], developed an electromagnetic theory consistent with special relativity and quantum mechanics that describes how matter and light interact; the so-called “quantum eletrodynamics” (QED) had born.

QED has become the guide in the development of theories that describe the universe. It was the first example of a quantum field theory (QFT), which is the theoretical framework for building quantum mechanical models that describes particles and their interactions. QFT is composed of a set of mathematical tools that combines classical fields, special relativity and quantum mechanics, while keeping the quantum point particles and locality ideas.

This chapter gives an overview of the standard model of particle physics, starting with a description of the particles and interactions that compose it, followed by a description of the electroweak interaction, the Higgs boson and the associated production of Higgs boson and a single top quark (tH). The description contained in this chapter is based on references [4–6].

2.2 Standard model of particle physics

Particle physics at the fundamental level is modeled in terms of a collection of interacting particles and fields in a theory known as the "standard model of particle physics (SM)"[1].

The full picture of the SM is composed of three fields[2], whose excitations are interpreted as particles called mediators or force-carriers; a set of fields, whose excitations are interpreted as elementary particles, interacting through the exchange of those mediators and a field that gives the mass to elementary particles. Figure 2.1 shows an scheme of the SM particles organization. In addition to the particles in the scheme (but not listed in it), their corresponding anti-particles, with opposite quantum numbers, are also part of the picture; some particles are their own anti-particles, like photon or Higgs, or anti-particle is already listed like in the W^+ and W^- case.

The mathematical formulation of the SM is based on group theory and the use of Noether's theorem [8] which states that for a physical system modeled by a Lagrangian

[1] The formal and complete treatment of the SM is out of the scope of this document, however a plenty of textbooks describing it at several levels are available in the literature. The treatment in references [**?**] is quite comprehensive and detailed.

[2] Note that gravitational field is not included in the standard model formulation

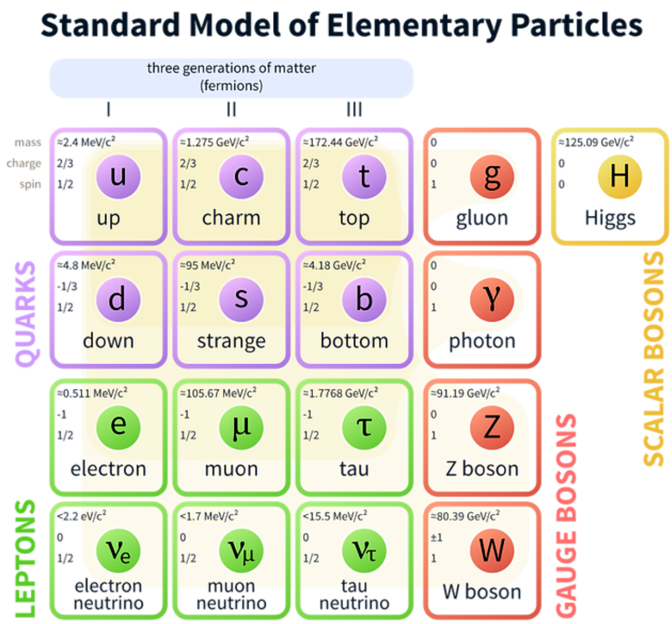

Figure 2.1: Schematic representation of the Standard model of particle physics. SM is a theoretical model intended to describe three of the four fundamental forces of the universe in terms of a set of particles and their interactions. [7].

that is invariant under a group of transformations a conservation law is expected. For instance, a system described by a time-independent Lagrangian is invariant (symmetric) under time changes (transformations) with the total energy conservation law as the expected conservation law. In QED, the charge operator (Q) is the generator of the U(1) symmetry which according to the Noether's theorem means that there is a conserved quantity; this conserved quantity is the electric charge and thus the law conservation of electric charge is established.

In the SM, the symmetry group $SU(3)_C \otimes SU(2)_L \otimes U(1)_Y$ describes three of the four fundamental interactions in nature(see section 2.2.2): strong interaction(SI), weak interaction(WI) and electromagnetic interactions (EI) in terms of symmetries associated to physical quantities:

- Strong: $SU(3)_C$ associated to color charge
- Weak: $SU(2)_L$ associated to weak isospin and chirality
- Electromagnetic: $U(1)_Y$ associated to weak hypercharge and electric charge

It will be shown that the electromagnetic and weak interactions are combined in the so-called electroweak interaction where chirality, hypercharge, weak isospin and electric charge are the central concepts.

2.2.1 Fermions

The basic constituents of the ordinary matter at the lowest level, which form the set of elementary particles in the SM formulation, are quarks and leptons. All of them have spin 1/2, therefore they are classified as fermions since they obey Fermi-Dirac statistics. There are six "flavors" of quarks and three of leptons organized in three generations, or families, as shown in table 2.1.

		Generation		
	Type	1st	2nd	3rd
Leptons	Charged	Electron (e)	Moun(μ)	Tau (τ)
	Neutral	Electron neutrino (ν_e)	Muon neutrino (ν_μ)	Tau neutrino (ν_τ)
Quarks	Up-type	Up (u)	Charm (c)	Top (t)
	Down-type	Down (d)	Strange (s)	Bottom (b)

Table 2.1: Fermions of the SM. There are six flavors of quarks and three of leptons, organized in three generations, or families, composed of two pairs of closely related particles. The close relationship is motivated by the fact that WI between leptons is limited to the members of the same generation; WI between quarks is not limited but greatly favoured, to same generation members.

There is a mass hierarchy between generations (see table 2.2), where the higher generation particles decays to the lower one, which can explain why the ordinary matter is made of particles in the first generation. In the SM, neutrinos are modeled as massless particles so they are not subject to this mass hierarchy; however, today it is known that neutrinos are massive so the hierarchy could be restated. The reason behind this mass hierachy is one of the most important open questions in particle physics, and it becomes more puzzling when noticing that the mass difference between first and second generation fermions is small compared to the mass difference with respect to the third generation.

Lepton	Mass (MeV/c^2)	Quark	Mass (MeV/c^2)
e	0.51	u	2.2
μ	105.65	c	1.28×10^3
τ	1776.86	t	173.1×10^3
ν_e	Unknown	d	4.7
ν_μ	Unknown	s	96
τ_μ	Unknown	b	4.18×10^3

Table 2.2: Fermion masses [9]. Generations differ by mass in a way that have been interpreted as a masss hierarchy. Approximate values with no uncertainties are used, for comparison purpose.

Usually, the second and third generation fermions are produced in high energy processes, like the ones recreated in particle accelerators.

2.2.1.1 Leptons

A lepton is an elementary particle that is not subject to the SI. As seen in table 2.1, there are two types of leptons, the charged ones (electron, muon and tau) and the neutral ones (the three neutrinos). The electric charge (Q) is the property that gives leptons the ability to participate in the EI. From the classical point of view, Q plays a central role determining, among others, the strength of the electric field through which the electromagnetic force is exerted. It is clear that neutrinos are not affected by EI because they don't carry electric charge.

Another feature of the leptons that is fundamental in the mathematical description of the SM is the chirality, which is closely related to spin and helicity. Helicity defines the handedness of a particle by relating its spin and momentum such that if they are parallel then the particle is right-handed; if spin and momentum are antiparallel the particle is said to be left-handed. The study of parity conservation (or violation) in β-decay has shown that only left-handed electrons/neutrinos or right-handed positrons/anti-neutrinos are created [10]; the inclusion of that feature in the theory was achieved by using projection operators for helicity, however, helicity is frame dependent for massive particles which makes it not Lorentz invariant and then another related attribute has to be used: *chirality*.

Chirality is a purely quantum attribute which makes it not so easy to describe in graphical terms but it defines how the wave function of a particle transforms under certain rotations. As with helicity, there are two chiral states, left-handed chiral (L) and right-handed chiral (R). In the highly relativistic limit where $E \approx p \gg m$ helicity and chirality converge, becoming exactly the same for massless particles.

In the following, when referring to left-handed (right-handed) it will mean left-handed chiral (right-handed chiral). The fundamental fact about chirality is that while EI and SI are not sensitive to chirality, in WI left-handed and right-handed fermions are treated asymmetrically, such that only left handed fermions and right-handed anti-fermions are allowed to couple to WI mediators, which is a violation of parity. The way to translate this statement in a formal mathematical formulation is based on the isospin symmetry group $SU(2)_L$.

Each generation of leptons is seen as a weak isospin doublet.[3] The left-handed charged lepton and its associated left-handed neutrino are arranged in doublets of weak isospin T=1/2 while their right-handed partners are singlets:

$$\begin{pmatrix}\nu_l\\ l\end{pmatrix}_L, l_R := \begin{pmatrix}\nu_e\\ e\end{pmatrix}_L, \begin{pmatrix}\nu_\mu\\ \mu\end{pmatrix}_L, \begin{pmatrix}\nu_\tau\\ \tau\end{pmatrix}_L, e_R, \mu_R, \tau_R, \nu_{eR}, \nu_{\mu R}, \nu_{\tau R} \tag{2.1}$$

The isospin third component refers to the eigenvalues of the weak isospin operator which for doublets is $T_3 = \pm 1/2$, while for singlets it is $T_3 = 0$. The physical meaning of this doublet-singlet arrangement falls in that the WI couples the two particles in the doublet by exchanging the interaction mediator while the singlet member is not involved in WI. The main properties of the leptons are summarized in table 2.3.

Altough all three flavor neutrinos have been observed, their masses remain unknown and only some estimations have been made [11]. The main reason is that the flavor eigenstates are not the same as the mass eigenstates which implies that when a neutrino is created its mass state is a linear combination of the three mass eigenstates and experiments can only probe the squared difference of the masses. The Pontecorvo-Maki-Nakagawa-Sakata (PMNS) mixing matrix encode the relationship between flavor and mass eigenstates.

2.2.1.2 Quarks

Quarks are the basic constituents of protons and neutrons. The way quarks join to form bound states, called "hadrons", is through the SI. Quarks are affected by all the

[3] The weak isospin is an analogy of the isospin symmetry in strong interaction where neutron and proton are affected equally by strong force but differ in their charge.

Lepton	Q(e)	T_3	L_e	L_μ	L_τ	Lifetime (s)
Electron (e)	-1	-1/2	1	0	0	Stable
Electron neutrino(ν_e)	0	1/2	1	0	0	Unknown
Muon (μ)	-1	-1/2	0	1	0	2.19×10^{-6}
Muon neutrino (ν_μ)	0	1/2	0	1	0	Unknown
Tau (τ)	-1	-1/2	0	0	1	290.3×10^{-15}
Tau neutrino (τ_μ)	0	1/2	0	0	1	Unknown

Table 2.3: Leptons properties [9]. Q: electric charge, T_3: weak isospin. Only left-handed leptons and right-handed anti-leptons participate in the WI. Anti-particles with inverted T_3, Q and lepton number complete the leptons set but are not listed. Right-handed leptons and left-handed anti-leptons, neither listed, form weak isospin singlets with $T_3 = 0$ and do not take part in the weak interaction.

fundamental interactions which means that they carry all the four types of charges: color, electric charge, weak isospin and mass.

Flavor	Q(e)	I_3	T_3	B	C	S	T	B'	Y	Color
Up (u)	2/3	1/2	1/2	1/3	0	0	0	0	1/3	r,b,g
Charm (c)	2/3	0	1/2	1/3	1	0	0	0	4/3	r,b,g
Top(t)	2/3	0	1/2	1/3	0	0	1	0	4/3	r,b,g
Down(d)	-1/3	-1/2	-1/2	1/3	0	0	0	0	1/3	r,b,g
Strange(s)	-1/3	0	-1/2	1/3	0	-1	0	0	-2/3	r,b,g
Bottom(b)	-1/3	0	-1/2	1/3	0	0	0	-1	-2/3	r,b,g

Table 2.4: Quarks properties [9]. Q: electric charge, I_3: isospin, T_3: weak isospin, B: baryon number, C: charmness, S: strangeness, T: topness, B': bottomness, Y: hypercharge. Anti-quarks posses the same mass and spin as quarks but all charges (color, flavor numbers) have opposite sign.

Table 2.4 summarizes the features of quarks, among which the most particular is their fractional electric charge. Note that fractional charge is not a problem, given that quarks are not found isolated, but serves to explain how composed particles are formed out of two or more valence quarks[4].

[4] Hadrons can contain an indefinite number of virtual quarks and gluons, known as the quark and gluon sea, but only the valence quarks determine hadrons' quantum numbers.

Color charge is the responsible for the SI between quarks and is the symmetry ($SU(3)_C$) that defines the formalism to describe SI. There are three colors: red (r), blue(b) and green(g) and their corresponding three anti-colors; thus each quark carries one color unit while anti-quarks carries one anti-color unit. As said above, quarks are not allowed to be isolated due to the color confinement effect, therefore their features have been studied indirectly by observing their bound states created when:

- one quark with a color charge is attracted by an anti-quark with the corresponding anti-color charge forming a colorless particle called a "meson."
- three quarks (anti-quarks) with different color (anti-color) charges are attracted among them forming a colorless particle called a "baryon(anti-baryon)."

In practice, when a quark is left alone isolated a process called "hadronization" occurs where the quark emits gluons (see section 2.2.3) which eventually will generate new quark-antiquark pairs and so on; those quarks will recombine to form hadrons that will decay into leptons. This proliferation of particles looks like a "jet" coming from the isolated quark. More details about the hadronization process and jet structure will be given in chapter4.

In the first version of the quark model (1964), M. Gell-Mann [12] and G. Zweig [13, 14] developed a consistent way to classify hadrons according to their properties. Only three quarks (u, d, s) were involved in a scheme in which all baryons have baryon number B=1 and therefore quarks have B=1/3; non-baryons have B=0. The scheme organizes baryons in a two-dimensional space (I_3 - Y); Y (hypercharge) and I_3 (isospin) are quantum numbers related by the Gell-Mann-Nishijima formula [15, 16]:

$$Q = I_3 + \frac{Y}{2} \tag{2.2}$$

where $Y = B+S+C+T+B'$ are the quantum numbers listed in table 2.4. Baryon number is conserved in SI and EI which means that single quarks cannot be created but in pairs $q-\bar{q}$.

There are six quark flavors organized in three generations (see table 2.1) following a mass hierarchy which, again, implies that higher generations decay to first generation quarks.

	Quarks			T_3	Y_W	Leptons			T_3	Y_W
Doublets	$\binom{u}{d'}_L$	$\binom{c}{s'}_L$	$\binom{t}{b'}_L$	$\binom{1/2}{-1/2}$	1/3	$\binom{\nu_e}{e}_L$	$\binom{\nu_\mu}{\mu}_L$	$\binom{\nu_\tau}{\tau}_L$	$\binom{1/2}{-1/2}$	-1
Singlets	u_R	c_R	t_R	0	4/3	ν_{eR}	$\nu_{\mu R}$	$\nu_{\tau R}$		
	d'_R	s'_R	b'_R	0	-2/3	e_R	μ_R	τ_R	0	-2

Table 2.5: Fermion weak isospin and weak hypercharge multiplets. Weak hypercharge is calculated through the Gell-Mann-Nishijima formula 2.2 but using the weak isospin and charge for quarks.

Isospin doublets of quarks are also defined (see table 2.5) and as for neutrinos, the mass eigenstates are not the same as the WI eigenstates which means that members of different quark generations are connected by the WI mediator; thus, up-type quarks are coupled not to down-type quarks directly but to a superposition of down-type quarks (q'_d) via WI according to:

$$
\begin{gathered}
q'_d = V_{CKM}\; q_d \\
\begin{pmatrix} d' \\ s' \\ b' \end{pmatrix} = \begin{pmatrix} V_{ud} & V_{us} & V_{ub} \\ V_{cd} & V_{cs} & V_{cb} \\ V_{td} & V_{ts} & V_{tb} \end{pmatrix} \begin{pmatrix} d \\ s \\ b \end{pmatrix}
\end{gathered}
\tag{2.3}
$$

where V_{CKM} is known as Cabibbo-Kobayashi-Maskawa (CKM) mixing matrix [17,18].

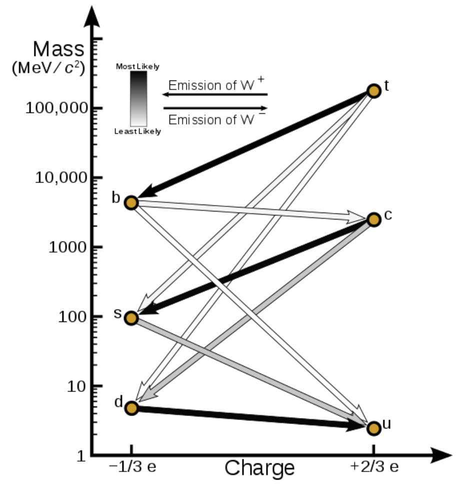

Figure 2.2: Transformations between quarks through the exchange of a WI. Higher generations quarks decay to first generation quarks by emitting a W boson. The arrow color indicates the likelihood of the transition according to the grey scale in the top left side which represent the CKM matrix parameters [19].

The weak decays of quarks are represented in the diagram of figure 2.2; again the CKM matrix plays a central role since it contains the probabilities for the different quark decay channels, in particular, note that quark decays are greatly favored between generation members.

CKM matrix is a 3×3 unitary matrix parametrized by three mixing angles and the *CP-mixing phase*; the latter is the parameter responsible for the Charge-Parity symmetry violation (CP-violation) in the SM. The fact that the b quark decays almost all the times to a top quark is exploided in this thesis when making the selection of the signal events by requiring the presence of a jet tagged as a jet comming from a b quark in the final state. The effect of the *CP-mixing phase* on the cross section of associated production of Higss boson and a single top process is also explored in this thesis.

2.2.2 Fundamental interactions

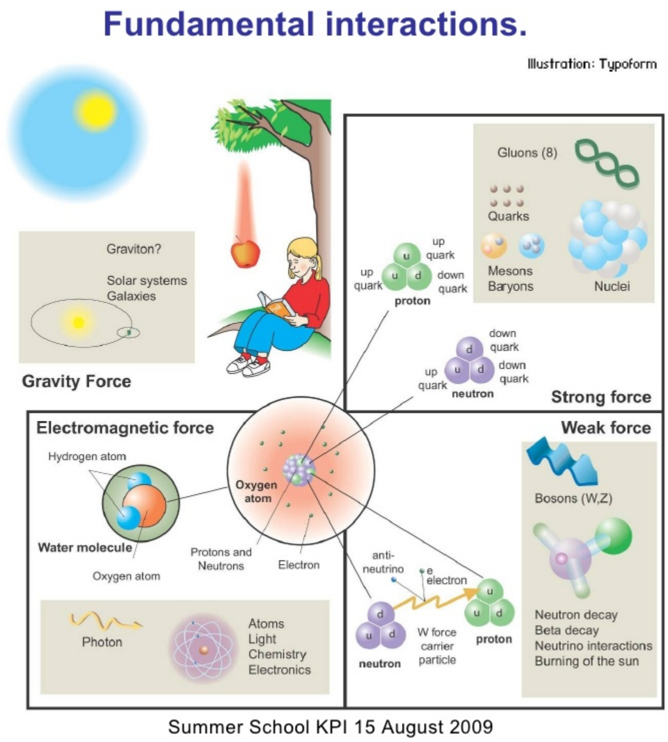

Figure 2.3: Fundamental interactions in nature. Despite the many manifestations of forces in nature, we can track all of them back to one of the fundamental interactions. The most common forces are gravity and electromagnetic given that all of us are subject and experience them in everyday life.

Even though there are many manifestations of force in nature, like the ones represented in figure 2.3, we can classify all of them into one of four fundamental interactions:

- *Electromagnetic interaction (EI)* affects particles that are "electrically charged," like electrons and protons. It is described by QED combining quantum mechanics, special relativity and electromagnetism in order to explain how particles with electric charge interact through the exchange of photons, therefore, one says that "Electomagnetic Force" is mediated by "photons". Figure 2.4a. shows a graphical representation, known as "feynman diagram", of electron-electron scattering.

- *Strong interaction (SI)* described by Quantum Chromodynamics (QCD). Hadrons like proton and neutron have internal structure given that they are composed of two or more valence quarks[5]. Quarks have fractional electric charge which means that they are subject to electromagnetic interaction and in the case of the proton they should break appart due to electrostatic repulsion; however, quarks are held together inside the hadrons against their electrostatic repulsion by the "Strong Force" through the exchange of "gluons." The analog to the electric charge is the "color charge". Electrons and photons are elementary particles as quarks but they don't carry color charge, therefore they are not subject to SI. The feynman diagram for gluon exchange between quarks is shown in figure 2.4b.

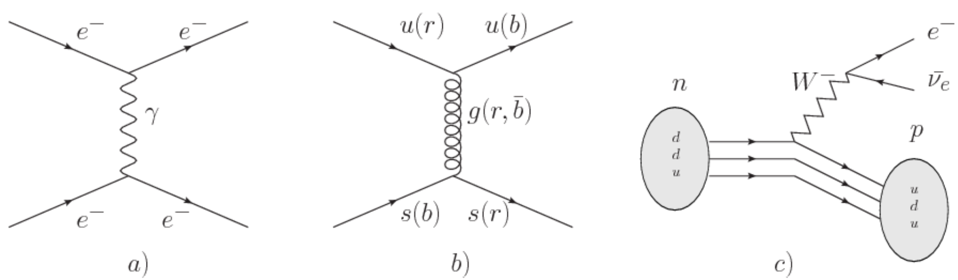

Figure 2.4: Feynman diagrams representing the interactions in SM; a) EI: e-e scattering; b) SI: gluon exchange between quarks ; c) WI: β-decay

- *Weak interaction (WI)* described by the weak theory (WT), is responsible, for instance, for the radioactive decay in atoms and proton-proton (pp) fusion within the sun. Quarks and leptons are the particles affected by the weak interaction; they possess a property called "flavor charge" (see 2.2.1) which can be changed by emitting or absorbing one weak force mediator. There are three

[5] particles made of four and five quarks are exotic states not so common.

mediators of the "weak force" known as "Z" boson in the case of electrically neutral changes and "$W^{\pm}$" bosons in the case of electrically charged changes. The "weak isospin" is the WI analog to electric charge in EI, and color charge in SI, and defines how quarks and leptons are affected by the weak force. Figure 2.4c. shows the feynman diagram of β-decay where a newtron (n) is transformed in a proton (p) by emmiting a W^{-} particle. Since this thesis is in the frame of the electroweak interaction, a more detailed description of it will be given in section 2.3

- *Gravitational interaction (GI)* described by General Theory of Relativity (GR). It is responsible for the structure of galaxies and black holes as well as the expansion of the universe. As a classical theory, in the sense that it can be formulated without even appeal to the concept of quantization, it implies that the spacetime is a continuum and predictions can be made without limitation to the precision of the measurement tools. The latter represent a direct contradiction of the quantum mechanics principles. Gravity is deterministic while quantum mechanics is probabilistic; despite that, efforts to develop a quantum theory of gravity have predicted the "graviton" as mediator of the Gravitational force[6].

Interaction	Acts on	Relative strength	Range (m)	Mediators
Electromagnetic (QED)	Electrically charged particles	10^{-2}	Infinite	Photon
Strong (QCD)	Quarks and gluons	1	10^{-15}	Gluon
Weak (WI)	Leptons and quarks	10^{-6}	10^{-18}	$W^{\pm}$, Z
Gravitational (GI)	Massive particles	10^{-39}	Infinite	Graviton

Table 2.6: Fundamental interactions features [20].

[6] Actually a wide variety of theories have been developed in an attempt to describe gravity; some famous examples are string theory and supergravity.

Table 2.6 sumarizes the main features of the fundamental interactions. The relative strength of the fundamental forces reveals the meaning of strong and weak; in a context where the relative strength of the SI is 1, the EI is about hundred times weaker and WI is about million times weaker thant the SI. A good description on how the relative strenght and range of the fundamental intreractions are calculated can be found in references [20, 21]. In the everyday life, only EI and GI are explicitly experienced due to the range of these interactions; i.e., at the human scale distances only EI and GI have appreciable effects, in contrast to SI which at distances greater than 10^{-15}m become negligible.

QED was built successfully on the basis of the classical electrodynamics theory (CED) of Maxwell and Lorentz, following theoretical and experimental requirements imposed by

- lorentz invariance: independence on the reference frame.
- locallity: interacting fields are evaluated at the same space-time point to avoid action at a distance.
- renormalizability: physical predictions are finite and well defined
- particle spectrum, symmetries and conservation laws already known must emerge from the theory.
- gauge invariance.

The gauge invariance requirement reflects the fact that the fundamental fields cannot be directly measured but associated fields which are the observables. Electric (**"E"**) and magnetic (**"B"**) fields in CED are associated with the electric scalar potential

"V" and the vector potential **"A"**. In particular, **E** can be obtained by measuring the change in the space of the scalar potential (ΔV); however, two scalar potentials differing by a constant "f" correspond to the same electric field. The same happens in the case of the vector potential **"A"**; thus, different configurations of the associated fields result in the same set of values of the observables. The freedom in choosing one particular configuration is known as "gauge freedom"; the tranformation law connecting two configurations is known as "gauge transformation" and the fact that the observables are not affected by a gauge transformation is called "gauge invariance".

When the gauge tranformation:

$$\begin{aligned} \mathbf{A} \to & \mathbf{A} - \Delta f \\ V \to & V - \frac{\partial f}{\partial t} \end{aligned} \tag{2.4}$$

is applied to Maxwell equations, they are still satisfied and the fields remain invariant. Thus, CED is invariant under gauge transformations and is called a "gauge theory". The set of all gauge transformations form the "symmetry group" of the theory, which according to the group theory, has a set of "group generators". The number of group generators determine the number of "gauge fields" of the theory.

As mentioned in the first lines of section 2.2, QED has one symmetry group (U(1)) with one group generator (the Q operator) and one gauge field (the electromagnetic field A^{μ}). In CED there is not a clear definition, beyond the historical convention, of which fields are the fundamental and which are the associated, but in QED it is clear that the fundamental field is A^{μ}. When a gauge theory is quantized, the gauge field is quantized and its quanta is called “gauge boson”. The word boson characterizes particles with integer spin which obvey Bose-einstein statistics.

As will be detailed in section 2.3, interactions between partcles in a system can be obtained by considering first the Lagrangian density of free particles in the system, which of course is incomplete because the interaction terms have been left out, and demanding global phase transformation invariance. Global phase transformation invariance means that a gauge transformation is performed identically to every point in the space[7] and the Lagrangian remains invariant. Then, the global transformation is promoted to a local phase transformation (this time the gauge transformation depends on the position in space) and again invariance is required.

Due to the space dependence of the local tranformation, the Lagrangian density is not invariant anymore. In order to restate the gauge invariance, the gauge covariant derivative is introduced in the Lagrangian and with it the gauge field responsible for the interaction between particles in the system. The new Lagrangian density is gauge invariant, includes the interaction terms needed to account for the interactions and provides a way to explain the interaction between particles through the exchange of the gauge boson.

This recipe was used to build QED and the theories that aim to explain the fundamental interactions.

2.2.3 Gauge bosons

The importance of the gauge bosons comes from the fact that they are the force mediators or force carriers. The features of the gauge bosons reflect those of the

[7] Here space corresponds to the 4-dimensional space i.e. space-time.

fields they represent and they are extracted from the Lagrangian density used to describe the interactions. In section 2.3, it will be shown how the gauge bosons of the EI and WI emerge from the electroweak Lagrangian. The SI gauge bosons features are also extracted from the SI Lagrangian but it is not detailed in this document. The main features of the SM gauge bosons will be briefly presented below and summarized in table 2.7.

- **Photon**. EI occurs when the photon couples to (is exchanged between) particles carrying electric charge; however, the photon itself does not carry electric charge, therefore, there is no coupling between photons. Given that the photon is massless the EI is of infinite range, i.e., electrically charged particles interact even if they are located far away one from each other; this also implies that photons always move with the speed of light.

- **Gluon**. SI is mediated by gluons which, same as photons, are massless. They carry one unit of color charge and one unit of anticolor charge which means that gluons couple to other gluons. As a result, the range of the SI is not infinite but very short due to the attraction between gluons, giving rise to the "color confinement" which explains why color charged particles cannot be isolated but live within composited particles, like quarks inside protons.

- **W, Z**. The WI mediators, $W^{\pm}$ and Z, are massive which explains their short-range. Given that the WI is the only interaction that can change the flavor of the interacting particles, the W boson is the responsible for the nuclear transmutation where a neutron is converted in a proton or vice versa with the involvement of an electron and a neutrino (see figure 2.4c). The Z boson is the responsible of the neutral weak processes like neutrino elastic scattering where no electric charge but momentum transference is involved. WI gauge bosons carry isospin charge which makes posible the interaction between them.

Interaction	Mediator	Electric charge (e)	Color charge	Weak Isospin	mass (GeV/c^2)
Electromagnetic	Photon (γ)	0	No	0	0
Strong	Gluon (g)	0	Yes -octet	No	0
Weak	$W^{\pm}$	±1	No	±1	80.385 $\pm$ 0.015
	Z	0	No	0	91.188 $\pm$ 0.002

Table 2.7: SM gauge bosons main features [9].

2.3 Electroweak unification and the Higgs mechanism

Physicists dream of building a theory that contains all the interactions in one single interaction, i.e., showing that at some scale in energy all the four fundamental interactions are unified and only one interaction emerges in a "Theory of everything". The first sign of the feasibility of such unification comes from success in the construction of the CED. Einstein spent years trying to reach that dream, which by 1920 only involved electromagnetism and gravity, with no success; however, a new partial unification was achieved in the 1960's, when S.Glashow [22], A.Salam [23] and S.Weinberg [24] independently proposed that electromagnetic and weak interactions are two manifestations of a more general interaction called "electroweak interaction (EWT)". Both, QCD and EWT, were developed in parallel and following the useful prescription provided by QED and the gauge invariance principles.

The theory of weak interactions was capable of explaining the β-decay and in general the processes mediated by $W^{\pm}$ bosons. However, there were some processes like the

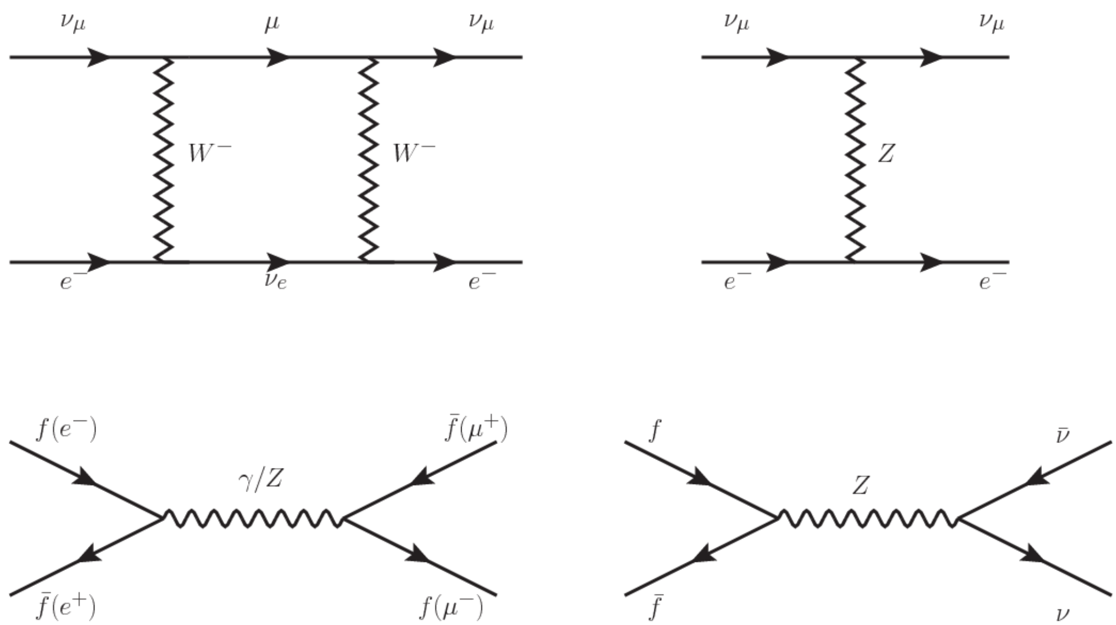

Figure 2.5: Top: $\nu_\mu - e^-$ scattering going through charged currents (left) and neutral currents (right). Bottom: neutral current processes for charged fermions (left) and involving neutrinos (right). While neutral current processes involving only charged fermions can proceed through EI or WI, those involving neutrinos can only proceed via WI.

"$\nu_\mu - e$ scattering" which would require the exchange of two W bosons (see figure 2.5 top diagrams) giving rise to divergent loop integrals and then non finite predictions. By including neutral currents involving fermions via the exchange of neutral bosons Z, those divergences are compensated and the predictions become realistic.

Neutral weak interaction vertices conserve flavor in the same way as the electromagnetic vertices do, but additionally, the Z boson can couple to neutrinos which implies that processes involving charged fermions can proceed through EI or WI but processes involving neutrinos can proceed only through WI.

The prescription to build a gauge theory of the WI consists of proposing a free field Lagrangian density that includes the particles involved; next, by requesting invariance under global phase transformations first and generalizing to local phase transformations invariance later, the conserved currents are identified and interactions are generated by introducing gauge fields. Given that the goal is to include the EI and WI in a single theory, the group symmetry considered should be a combination of $SU(2)_L$ and $U(1)_{em}$, however the latter cannot be used directly because the EI treats left and right-handed particles indistinctly in contrast to the former. Fortunately, the weak hypercharge, which is a combination of the weak isospin and the electric charge (eqn 2.2) is suitable to be used since it is conserved by the EI and WI. Thus, the symmetry group to be considered is

$$G \equiv SU(2)_L \otimes U(1)_Y \tag{2.5}$$

The following treatment applies to any of the fermion generations, but for simplicity the first generation of leptons will be considered [5, 6, 25, 26].

Given the first generation of leptons

$$\psi_1 = \begin{pmatrix} \nu_e \\ e^- \end{pmatrix}_L, \qquad \psi_2 = \nu_{eR}, \qquad \psi_3 = e^-_R \tag{2.6}$$

the charged fermionic currents are given by

$$J_\mu \equiv J^+_\mu = \bar{\nu}_{eL}\gamma_\mu e_L, \qquad J^\dagger_\mu \equiv J^-_\mu = \bar{e}_L\gamma_\mu \nu_{eL} \tag{2.7}$$

and the free Lagrangian is given by

$$\mathcal{L}_0 = \sum_{j=1}^{3} i\overline{\psi}_j(x)\gamma^\mu\partial_\mu\psi_j(x). \tag{2.8}$$

Mass terms are included directly in the QED and QCD free Lagrangians since they preserve the invariance under the symmetry transformations involved which treat left-handed and right-handed similarly, however mass terms of the form

$$m_W^2 W_\mu^\dagger(x) W^\mu(x) + \frac{1}{2} m_Z^2 Z_\mu(x) Z^\mu(x) - m_e \bar{\psi_e}(x) \psi_e(x) \tag{2.9}$$

which represent the mass of $W^\pm$, Z and electrons, are not invariant under G transformations, therefore the gauge fields described by the EWI are in principle massless.

Experiments have shown that the gauge fields are not massless; however, they have to acquire mass through a mechanism compatible with the gauge invariance; that mechanism is known as the "Higgs mechanism" and will be considered later in this section. The global transformations in the combined symmetry group G can be written as

$$\begin{aligned} \psi_1(x) &\xrightarrow{G} \psi_1'(x) \equiv U_Y U_L \psi_1(x), \\ \psi_2(x) &\xrightarrow{G} \psi_2'(x) \equiv U_Y \psi_2(x), \\ \psi_3(x) &\xrightarrow{G} \psi_3'(x) \equiv U_Y \psi_3(x) \end{aligned} \tag{2.10}$$

where U_L represent the $SU(2)_L$ transformation acting only on the weak isospin doublet and U_Y represent the $U(1)_Y$ transformation acting on all the weak isospin multiplets. Explicitly

$$U_L \equiv \exp\left(i\frac{\sigma_i}{2}\alpha^i\right), \qquad U_Y \equiv \exp(iy_i\beta) \qquad (i = 1,2,3) \tag{2.11}$$

with σ_i the Pauli matrices and y_i the weak hypercharges. In order to promote the transformations from global to local while keeping the invariance, it is required that

$\alpha^i = \alpha^i(x)$, $\beta = \beta(x)$ and the replacement of the ordinary derivatives by the covariant derivatives

$$\begin{aligned} D_\mu\psi_1(x) &\equiv \left[\partial_\mu + ig\sigma_i W_\mu^i(x)/2 + ig' y_1 B_\mu(x)\right]\psi_1(x) \\ D_\mu\psi_2(x) &\equiv \left[\partial_\mu + ig' y_2 B_\mu(x)\right]\psi_2(x) \\ D_\mu\psi_3(x) &\equiv \left[\partial_\mu + ig' y_3 B_\mu(x)\right]\psi_3(x) \end{aligned} \tag{2.12}$$

introducing in this way four gauge fields, $W_\mu^i(x)$ and $B_\mu(x)$, in the process. The covariant derivatives (eqn 2.12) are required to transform in the same way as fermion fields $\psi_i(x)$ themselves, therefore, the gauge fields transform as:

$$\begin{aligned} B_\mu(x) &\xrightarrow{G} B'_\mu(x) \equiv B_\mu(x) - \frac{1}{g'}\partial_\mu\beta(x) \\ W_\mu^i(x) &\xrightarrow{G} W_\mu^{i\prime}(x) \equiv W_\mu^i(x) - \frac{i}{g}\partial_\mu\alpha_i(x) - \varepsilon_{ijk}\alpha_i(x)W_\mu^i(x). \end{aligned} \tag{2.13}$$

The G invariant version of the Lagrangian density 2.8 can be written as

$$\mathcal{L}_0 = \sum_{j=1}^{3} i\overline{\psi}_j(x)\gamma^\mu D_\mu\psi_j(x) \tag{2.14}$$

where free massless fermion and gauge fields and fermion-gauge boson interactions are included. The EWI Lagrangian density must additionally include kinetic terms for the gauge fields ($\mathcal{L}_G$) which are built from the field strengths, according to

$$B_{\mu\nu}(x) \equiv \partial_\mu B_\nu - \partial_\nu B_\mu \tag{2.15}$$

$$W^i_{\mu\nu}(x) \equiv \partial_\mu W^i_\nu(x) - \partial_\nu W^i_\mu(x) - g\varepsilon^{ijk} W^j_\mu W^k_\nu \tag{2.16}$$

the last term in eqn. 2.16 is added in order to hold the gauge invariance; therefore,

$$\mathcal{L}_G = -\frac{1}{4} B_{\mu\nu}(x) B^{\mu\nu}(x) - \frac{1}{4} W^i_{\mu\nu}(x) W_i^{\mu\nu}(x) \tag{2.17}$$

which contains not only the free gauge fields contributions, but also the gauge fields self-interactions and interactions among them.

The three weak isospin conserved currents resulting from the $SU(2)_L$ symmetry are given by

$$J^i_\mu(x) = \frac{1}{2} \bar{\psi}_1(x) \gamma_\mu \sigma^i \psi_1(x) \tag{2.18}$$

while the weak hypercharge conserved current resulting from the $U(1)_Y$ symmetry is given by

$$J^Y_\mu = \sum_{j=1}^{3} \overline{\psi}_j(x) \gamma_\mu y_j \psi_j(x) \tag{2.19}$$

In order to evaluate the electroweak interactions modeled by an isotriplet field W^i_μ which couples to isospin currents J^i_μ with strength g and additionally the singlet field B_μ which couples to the weak hypercharge current J^Y_μ with strength $g'/2$. The interaction Lagrangian density to be considered is

$$\mathcal{L}_I = -gJ^{i\mu}(x)W^i_\mu(x) - \frac{g'}{2}J^{Y\mu}(x)B_\mu(x) \tag{2.20}$$

Note that the weak isospin currents are not the same as the charged fermionic currents that were used to describe the WI (eqn 2.7), since the weak isospin eigenstates are not the same as the mass eigenstates, but they are closely related

$$J_\mu = \frac{1}{2}(J^1_\mu + iJ^2_\mu), \qquad J^\dagger_\mu = \frac{1}{2}(J^1_\mu - iJ^2_\mu). \tag{2.21}$$

The same happens with the gauge fields W^i_μ which are related to the mass eigenstates $W^\pm$ by

$$W^+_\mu = \frac{1}{\sqrt{2}}(W^1_\mu - iW^2_\mu), \qquad W^-_\mu = \frac{1}{\sqrt{2}}(W^1_\mu + iW^2_\mu). \tag{2.22}$$

The fact that there are three weak isospin conserved currents is an indication that in addition to the charged fermionic currents, which couple charged to neutral leptons, there should be a neutral fermionic current that does not involve electric charge exchange; therefore, it couples neutral fermions or fermions of the same electric charge. The third weak isospin current contains a term that is similar to the electromagnetic current (j^{em}_μ), indicating that there is a relation between them and resembling the Gell-Mann-Nishijima formula 2.2 adapted to electroweak interactions

$$Q = T_3 + \frac{Y_W}{2}. \tag{2.23}$$

Just as Q generates the $U(1)_{em}$ symmetry, the weak hypercharge generates the $U(1)_Y$ symmetry as said before. It is possible to write the relationship in terms of the currents as

$$j_\mu^{em} = J_\mu^3 + \frac{1}{2} J_\mu^Y . \tag{2.24}$$

The neutral gauge fields W_μ^3 and B_μ cannot be directly identified with the Z and the photon fields since the photon interacts similarly with left and right-handed fermions; however, they are related through a linear combination given by

$$\begin{aligned} A_\mu =& B_\mu \cos\theta_W + W_\mu^3 \sin\theta_W \\ Z_\mu =& -B_\mu \sin\theta_W + W_\mu^3 \cos\theta_W \end{aligned} \tag{2.25}$$

where θ_W is known as the "Weinberg angle." The interaction Lagrangian is now given by

$$\mathcal{L}_I = -\frac{g}{\sqrt{2}}(J^\mu W_\mu^+ + J^{\mu\dagger} W_\mu^-) - \left(g \sin\theta_W J_\mu^3 + g' \cos\theta_W \frac{J_\mu^Y}{2} \right) A^\mu - \left(g \cos\theta_W J_\mu^3 - g' \sin\theta_W \frac{J_\mu^Y}{2} \right) Z^\mu \tag{2.26}$$

the first term is the weak charged current interaction, while the second term is the electromagnetic interaction under the condition

$$g \sin\theta_W = g' \cos\theta_W = e, \qquad \frac{g'}{g} = tan\theta_W \tag{2.27}$$

contained in the eqn.2.24; the third term is the neutral weak current.

Note that the neutral fields transformation given by the eqn. 2.25 can be written in terms of the coupling constants g and g' as:

$$A_\mu = \frac{g' W_\mu^3 + g B_\mu}{\sqrt{g^2 + g'^2}}, \qquad Z_\mu = \frac{g W_\mu^3 - g' B_\mu}{\sqrt{g^2 + g'^2}} \tag{2.28}$$

So far, the Lagrangian density describing the non-massive EWI is:

$$\mathcal{L}_{nmEWI} = \mathcal{L}_0 + \mathcal{L}_G \tag{2.29}$$

where fermion and gauge fields have been considered massless because their regular mass terms are manifestly non invariant under G transformations; therefore, masses have to be generated in a gauge invariant way. The mechanism by which this goal is achieved is known as the "Higss mechanism" and is closely connected to the concept of "spontaneous symmetry breaking."

2.3.1 Spontaneous symmetry breaking (SSB)

Figure 2.6 left shows a steel nail (top) which is subject to an external force; the form of the potential energy is also shown (bottom).

Before reaching the critical force value, the system has rotational symmetry with respect to the nail axis; however, after the critical force value is reached the nail buckles (top right). The form of the potential energy (bottom right) changes, preserving its rotational symmetry although its minima does not exhibit that rotational symmetry any longer. Right before the nail buckles there is no indication of the direction the nail will bend because any of the directions are equivalent, but once the nail bends, choosing a direction, an arbitrary minimal energy state (ground state) is selected and it does not share the system's rotational symmetry. This mechanism for reaching an asymmetric ground state is known as *"spontaneous symmetry breaking"*.
The lesson from this analysis is that the way to introduce the SSB mechanism into a system is by adding the appropriate potential to it.

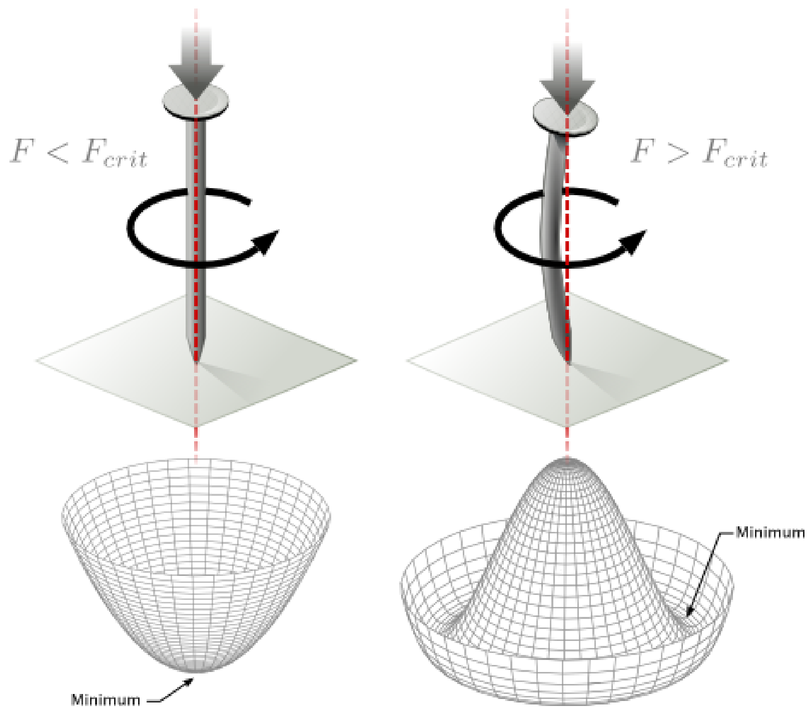

Figure 2.6: Spontaneous symmetry breaking mechanism. The steel nail, subject to an external force (top left), has rotational symmetry with respect to its axis. When the external force overcomes a critical value the nail buckles (top right) choosing a minimal energy state (ground state) and thus *"breaking spontoaneously the rotational symmetry"*. The potential energy (bottom) changes but holds the rotational symmetry; however, an infinite number of asymmetric ground states are generated and circularly distributed in the bottom of the potential [27].

Figure 2.7 shows a plot of the potential $V(\phi)$ in the case of a scalar field ϕ

$$V(\phi) = \mu^2 \phi^\dagger \phi + \lambda(\phi^\dagger \phi)^2 \tag{2.30}$$

If $\mu^2 > 0$ the potential has only one minimum at $\phi = 0$ and describes a scalar field with mass μ. If $\mu^2 < 0$ the potential has a local maximum at $\phi = 0$ and two minima at $\phi = \pm\sqrt{-\mu^2/\lambda}$ which enables the SSB mechanism to work.

In the case of a complex scalar field $\phi(x)$

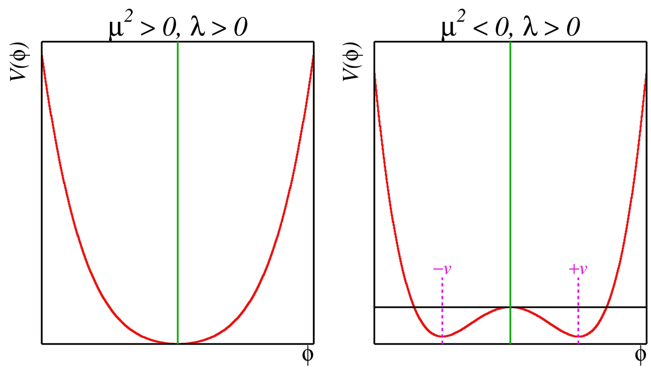

Figure 2.7: Shape of the potential $V(\phi)$ for $\lambda > 0$ and: $\mu^2 > 0$ (left) and $\mu^2 < 0$ (right). The case $\mu^2 < 0$ corresponds to the potential suitable for introducing the SSB mechanism by choosing one of the two ground states which are connected via refletion symmetry. [27].

$$\phi(x) = \frac{1}{\sqrt{2}}(\phi_1 + i\phi_2) \tag{2.31}$$

the Lagrangian (invariant under global $U(1)$ transformations) is given by

$$\mathcal{L} = (\partial_\mu \phi)^\dagger (\partial^\mu \phi) - V(\phi), \qquad V(\phi) = \mu^2 \phi^\dagger \phi + \lambda(\phi^\dagger \phi)^2 \tag{2.32}$$

where an appropiate potential has been added in order to introduce the SSB.

As seen in figure 2.8, the potential has now an infinite number of minima circularly distributed along the ξ-direction which makes possible the occurence of the SSB by choosing an arbitrary ground state; for instance, $\xi = 0$, i.e. $\phi_1 = v, \phi_2 = 0$

$$\phi_0 = \frac{v}{\sqrt{2}} \exp(i\xi) \quad \xrightarrow{SSB} \quad \phi_0 = \frac{v}{\sqrt{2}} \tag{2.33}$$

As usual, excitations over the ground state are studied by making an expansion about

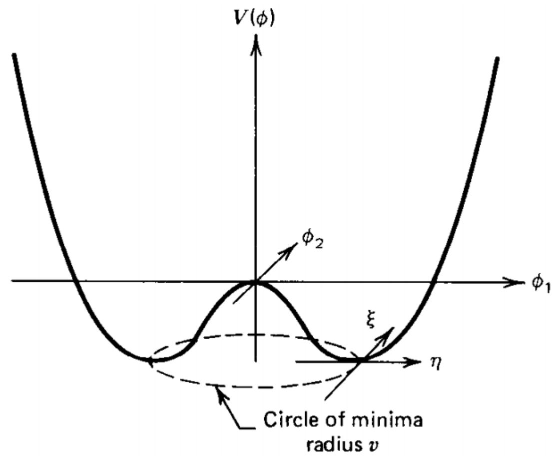

Figure 2.8: Potential for complex scalar field. There is a circle of minima of radius v along the ξ-direction [6].

it; thus, the excitation can be parametrized as:

$$\phi(x) = \frac{1}{\sqrt{2}}(v + \eta(x) + i\xi(x)) \tag{2.34}$$

which when substituted into eqn. 2.32 produces a Lagrangian in terms of the new fields η and ξ

$$\mathcal{L}' = \frac{1}{2}(\partial_\mu \xi)^2 + \frac{1}{2}(\partial_\mu \eta)^2 + \mu^2\eta^2 - V(\phi_0) - \lambda v \eta(\eta^2 + \xi^2) - \frac{\lambda}{4}(\eta^2 + \xi^2)^2 \tag{2.35}$$

where the last two terms represent the interactions and self-interaction between the two fields η and ξ. The particular feature of the SSB mechanism is revealed when looking to the first three terms of $\mathcal{L}'$. Before the SSB, only the massless ϕ field is present in the system; after the SSB there are two fields of which the η-field has acquired mass $m_\eta = \sqrt{-2\mu^2}$ while the $\xi - field$ is still massless (see figure 2.9).

Thus, *the SSB mechanism serves as a method to generate mass but as a side effect a*

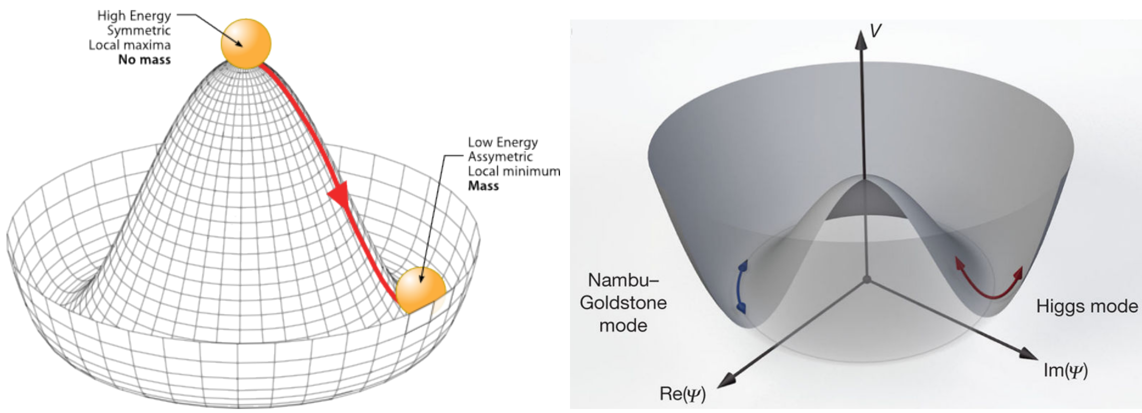

Figure 2.9: SSB mechanism for a complex scalar field [27, 28].

massless field is introduced in the system. This fact is known as the Goldstone theorem and states that a massless scalar field appears in the system for each continuous symmetry spontaneously broken. Another version of the Goldstone theorem states that *"if a Lagrangian is invariant under a continuous symmetry group G, but the vacuum is only invariant under a subgroup $H \subset G$, then there must exist as many massless spin-0 particles (Nambu-Goldstone bosons) as broken generators."* [26] The Nambu-Goldstone boson can be understood considering that the potential in the ξ-direction is flat so excitations in that direction are not energy consuming and thus represent a massless state.

2.3.2 Higgs mechanism

When the SSB mechanism is introduced in the formulation of the EWI in an attempt to generate the mass of the so far massless gauge bosons and fermions, an interesting effect is revealed. In order to keep the G symmetry group invariance and generate the mass of the EW gauge bosons, a G invariant Lagrangian density ($\mathcal{L}_S$) has to be added to the non massive EWI Lagrangian (eqn. 2.29)

$$\mathcal{L}_S = (D_\mu \phi)^\dagger (D^\mu \phi) - \mu^2 \phi^\dagger \phi - \lambda(\phi^\dagger \phi)^2, \qquad \lambda > 0, \mu^2 < 0 \tag{2.36}$$

$$D_\mu \phi = \left(i\partial_\mu - g\frac{\sigma_i}{2} W^i_\mu - g' \frac{Y}{2} B_\mu \right) \phi \tag{2.37}$$

ϕ has to be an isospin doublet of complex scalar fields so it preserves the G invariance; thus ϕ can be defined as:

$$\phi = \begin{pmatrix} \phi^+ \\ \phi^0 \end{pmatrix} \equiv \frac{1}{\sqrt{2}} \begin{pmatrix} \phi_1 + i\phi_2 \\ \phi_3 + i\phi_4 \end{pmatrix}. \tag{2.38}$$

The minima of the potential are defined by

$$\phi^\dagger \phi = \frac{1}{2}(\phi_1^2 + \phi_2^2 + \phi_3^2 + \phi_1^4) = -\frac{\mu^2}{2\lambda}. \tag{2.39}$$

The choice of the ground state is critical. By choosing a ground state, invariant under $U(1)_{em}$ gauge symmetry, the photon will remain massless and the $W^\pm$ and Z bosons masses will be generated which is exactly what is needed. In that sense, the best choice corresponds to a weak isospin doublet with $T_3 = -1/2$, $Y_W = 1$ and $Q = 0$ which defines a ground state with $\phi_1 = \phi_2 = \phi_4$ and $\phi_3 = v$:

$$\phi_0 \equiv \frac{1}{\sqrt{2}} \begin{pmatrix} 0 \\ v \end{pmatrix}, \qquad v^2 \equiv -\frac{\mu^2}{\lambda}. \tag{2.40}$$

where the vacuum expectation value v is fixed by the Fermi coupling G_F according to $v = (\sqrt{2} G_F)^{1/2} \approx 246$ GeV.

The G symmetry has been broken and three Nambu-Goldstone bosons will appear.

The next step is to expand ϕ about the chosen ground state as:

$$\phi(x) = \frac{1}{\sqrt{2}} \exp\left(\frac{i}{v}\sigma_i\theta^i(x)\right)\begin{pmatrix} 0 \\ v+H(x) \end{pmatrix} \approx \frac{1}{\sqrt{2}}\begin{pmatrix} \theta_1(x)+i\theta_2(x) \\ v+H(x)-i\theta_3(x) \end{pmatrix} \tag{2.41}$$

to describe fluctuations from the ground state ϕ_0. The fields $\theta_i(x)$ represent the Nambu-Goldstone bosons while $H(x)$ is known as "higgs field." The fundamental feature of the parametrization used is that the dependence on the $\theta_i(x)$ fields is factored out in a global phase that can be eliminated by taking the physical "unitary gauge" $\theta_i(x) = 0$. Therefore the expansion about the ground state is given by:

$$\phi(x)\frac{1}{\sqrt{2}}\begin{pmatrix} 0 \\ v+H(x) \end{pmatrix} \tag{2.42}$$

which when substituted into $\mathcal{L}_S$ (eqn. 2.36) results in a Lagrangian containing the now massive three gauge bosons $W^{\pm}, Z$, one massless gauge boson (photon) and the new Higgs field (H). The three degrees of freedom corresponding to the Nambu-Goldstone bosons are now integrated into the massive gauge bosons as their longitudinal polarizations which were not available when they were massless particles. The effect by which vector boson fields acquire mass after an spontaneous symmetry breaking, but without an explicit gauge invariance breaking is known as the *"Higgs mechanism"*.

The mechanism was proposed by three independent groups: F.Englert and R.Brout in August 1964 [29], P.Higgs in October 1964 [30] and G.Guralnik, C.Hagen and T.Kibble in November 1964 [31]; however, its importance was not realized until S.Glashow [22], A.Salam [23] and S.Weinberg [24], independently, proposed that electromagnetic and weak interactions are two manifestations of a more general interaction called "electroweak interaction" in 1967.

2.3.3 Masses of the gauge bosons

The mass of the gauge bosons is extracted by evaluating the kinetic part of Lagrangian $\mathcal{L}_S$ in the ground state (known also as the vacuum expectation value), i.e.,

$$\left|\left(\partial_\mu - ig\frac{\sigma_i}{2}W^i_\mu - i\frac{g'}{2}B_\mu\right)\phi_0\right|^2 = \left(\frac{1}{2}vg\right)^2 W^+_\mu W^{-\mu} + \frac{1}{8}v^2(W^3_\mu, B_\mu)\begin{pmatrix} g^2 & -gg' \\ -gg' & g'^2 \end{pmatrix}\begin{pmatrix} W^{3\mu} \\ B^\mu \end{pmatrix} \tag{2.43}$$

comparing with the typical mass term for a charged boson $M_W^2 W^+W^-$

$$M_W = \frac{1}{2}vg. \tag{2.44}$$

The second term in the right side of the eqn.2.43 comprises the masses of the neutral bosons, but it needs to be written in terms of the gauge fields Z_μ and A_μ in order to be compared to the typical mass terms for neutral bosons, therefore using eqn. 2.28

$$\begin{aligned} \frac{1}{8}v^2[g^2(W^3_\mu)^2 - 2gg'W^3_\mu B^\mu + g'^2 B^2_\mu] =& \frac{1}{8}v^2[gW^3_\mu - g'B_\mu]^2 + 0[g'W^3_\mu + gB_\mu]^2 \\ =& \frac{1}{8}v^2[\sqrt{g^2+g'^2}Z_\mu]^2 + 0[\sqrt{g^2+g'^2}A_\mu]^2 \end{aligned} \tag{2.45}$$

and then

$$M_Z = \frac{1}{2}v\sqrt{g^2+g'^2}, \qquad M_A = 0 \tag{2.46}$$

2.3.4 Masses of the fermions

The lepton mass terms can be generated by introducing a gauge invariant Lagrangian term describing the Yukawa coupling between the lepton field and the Higgs field

$$\mathcal{L}_{Yl} = -G_l \left[(\bar{\nu}_l, \bar{l})_L \begin{pmatrix} \phi^+ \\ \phi^0 \end{pmatrix} l_R + \bar{l}_R (\phi^-, \bar{\phi}^0) \begin{pmatrix} \nu_l \\ l \end{pmatrix}_L \right], \qquad l = e, \mu, \tau. \tag{2.47}$$

After the SSB and replacing the usual field expansion about the ground state (eqn.2.40) into $\mathcal{L}_{Yl}$, the mass term arises

$$\mathcal{L}_{Yl} = -m_l(\bar{l}_L l_R + \bar{l}_R l_L) - \frac{m_l}{v}(\bar{l}_L l_R + \bar{l}_R l_L)H = -m_l \bar{l} l \left(1 + \frac{H}{v}\right) \tag{2.48}$$

$$m_l = \frac{G_l}{\sqrt{2}} v \tag{2.49}$$

where the additional term represents the lepton-Higgs interaction. The quark masses are generated in a similar way as lepton masses but for the upper member of the quark doublet a different Higgs doublet is needed:

$$\phi_c = -i\sigma_2 \phi * = \begin{pmatrix} -\bar{\phi}^0 \\ \phi^- \end{pmatrix}. \tag{2.50}$$

Additionally, given that the quark isospin doublets are not constructed in terms of the mass eigenstates but in terms of the flavor eigenstates, as shown in table2.5, the coupling parameters will be related to the CKM matrix elements; thus the quark Lagrangian is given by:

$$\mathcal{L}_{Yq} = -G_d^{i,j} (\bar{u}_i, \bar{d}'_i)_L \begin{pmatrix} \phi^+ \\ \phi^0 \end{pmatrix} d_{jR} - G_u^{i,j} (\bar{u}_i, \bar{d}'_i)_L \begin{pmatrix} -\bar{\phi}^0 \\ \phi^- \end{pmatrix} u_{jR} + h.c. \tag{2.51}$$

with i,j=1,2,3. After SSB and expansion about the ground state, tha diagonal form of $\mathcal{L}_{Yq}$ is:

$$\mathcal{L}_{Yq} = -m_d^i \bar{d}_i d_i \left(1 + \frac{H}{v}\right) - m_u^i \bar{u}_i u_i \left(1 + \frac{H}{v}\right) \tag{2.52}$$

Fermion masses depend on arbitrary couplings G_l and $G_{u,d}$ and are not predicted by the theory.

2.3.5 The Higgs field

After the characterization of the fermions and gauge bosons as well as their interactions, it is necessary to characterize the Higgs field itself. The Lagrangian $\mathcal{L}_S$ in eqn. 2.36 written in terms of the gauge bosons is given by

$$\mathcal{L}_S = \frac{1}{4}\lambda v^4 + \mathcal{L}_H + \mathcal{L}_{HV} \tag{2.53}$$

$$\mathcal{L}_H = \frac{1}{2}\partial_\mu H \partial^\mu H - \frac{1}{2}m_H^2 H^2 - \frac{1}{2v}m_H^2 H^3 - \frac{1}{8v^2}m_H^2 H^4 \tag{2.54}$$

$$\mathcal{L}_{HV} = m_H^2 W_\mu^+ W^{\mu-}\left(1 + \frac{2}{v}H + \frac{2}{v^2}H^2\right) + \frac{1}{2}m_Z^2 Z_\mu Z^\mu \left(1 + \frac{2}{v}H + \frac{2}{v^2}H^2\right) \tag{2.55}$$

The mass of the Higgs boson is deduced as usual from the mass term in the Lagrangian resulting in:

$$m_H = \sqrt{-2\mu^2} = \sqrt{2\lambda}v \tag{2.56}$$

however, it is not predicted by the theory either. The experimental efforts to find the Higgs boson, carried out by the "Compact Muon Solenoid (CMS)" experiment and the "A Toroidal LHC AppartuS (ATLAS)" experiments at the "Large Hadron Collider(LHC)", gave great results by July of 2012 when the discovery of a new particle compatible with the Higgs boson predicted by the electroweak theory [32,33] was announced. Although at the announcement time there were some reservations about calling the new particle the "Higgs boson", today this name is widely accepted.

The Higgs mass measurement, reported by both experiments [34], is in table 2.8.

Property	Value
Electric charge	0
Colour charge	0
Spin	0
Weak isospin	-1/2
Weak hypercharge	1
Parity	1
Mass (GeV/c^2)	125.09$\pm$0.21 (stat.)$\pm$0.11 (syst.)

Table 2.8: Higgs boson properties. Higgs mass is not predicted by the theory and the value here corresponds to the experimental measurement.

2.3.6 Production of Higgs bosons at LHC

At LHC, Higgs boson is produced as a result of the collision of two counter-rotating protons beams. A detailled description of the LHC machine will be presented in chapter 3. “The total cross section” is a parameter that quantifies the number of pp collisions that happen when a number of protons are fired at each other. Different results can be obtained after a pp collision and for each one the “cross section” is defined as the number of pp collisions that conclude in that particular result with respect to the number of protons fired at each other.

Protons are composed of quarks and these quarks are bound by gluons; however, what is commonly called the quark content of the proton makes reference to the valence quarks. A sea of quarks and gluons is also present inside the proton as represented in figure 2.10. In a proton-proton (pp) collision, the constituents (quarks and gluons) are those who collide. The pp cross section depends on the momentum of the colliding particles, reason for which it is needed to know how the momentum is distributed inside the proton. Quarks and gluons are known as partons and the functions that describe how the proton momentum is distributed among partons inside it

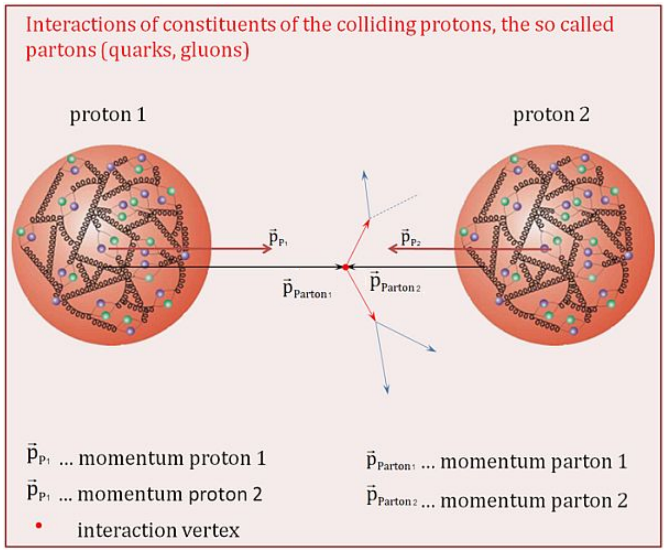

Figure 2.10: Proton-proton collision. Protons are composed of 3 valence quarks, a sea of quarks and gluons; therefore in a proton-proton collision, quarks and gluons are those who collide. [35].

are called "parton distribution functions (PDFs)"; PDFs are determined from experimental data obtanied in experiments where the internal structure of hadrons is tested.

In addition, in physics, a common approach to study complex systems consists in starting with a simpler version of them, for which a well known description is available, and add an additional "perturbation" which represents a small deviation from the known behavior. If the perturbation is small enough, the physical quanties associated with the perturbed system are expressed as a series of corrections to those of the simpler system; therefore, the more terms are considered in the series (the higher order in the perturbation series), the more precise is the the description of the complex system.

This thesis explores the Higgs production at LHC; therefore the overview presented here will be oriented specifically to the production mechanisms after pp collisions at

LHC.

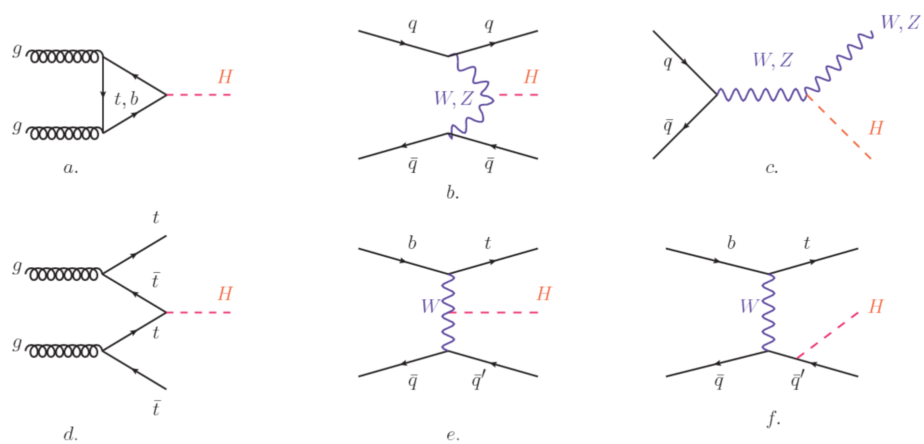

Figure 2.11: Main Higgs boson production mechanism Feynman diagrams. a. gluon-gluon fusion, b. vector boson fusion (VBF), c. Higgs-strahlung, d. Associated production with a top or bottom quark pair, e-f. associated production with a single top quark.

Figure 2.11 shows the Feynman diagrams for the leading order (first order) Higgs production processes at LHC, while the cross section for Higgs production as a function of the center of mass-energy ($\sqrt{s}$) for pp collisions is showed in figure 2.12 left. The tags NLO (next to leading order), NNLO (next to next to leading order) and N3LO (next to next to next to leading order) make reference to the order at which the pertubation series have been considered.

As shown in eqns 2.47, 2.51 and 2.55, the strength of the Higgs-fermion interaction is proportional to the fermion mass while the strength of the Higgs-gauge boson interaction is proportional to the square of the gauge boson mass, which implies that the Higgs production and decay mechanisms are dominated by couplings $H-(W,Z,t,b,\tau)$.

The main production mechanism is the gluon fusion (figure 2.11a and $pp \to H$ in figure 2.12) given that gluons carry the highest fraction of momentum of the protons in pp colliders. Since the Higgs boson does not couple to gluons, the mechanism proceeds through the exchange of a virtual top-quark loop given that for it the coupling is

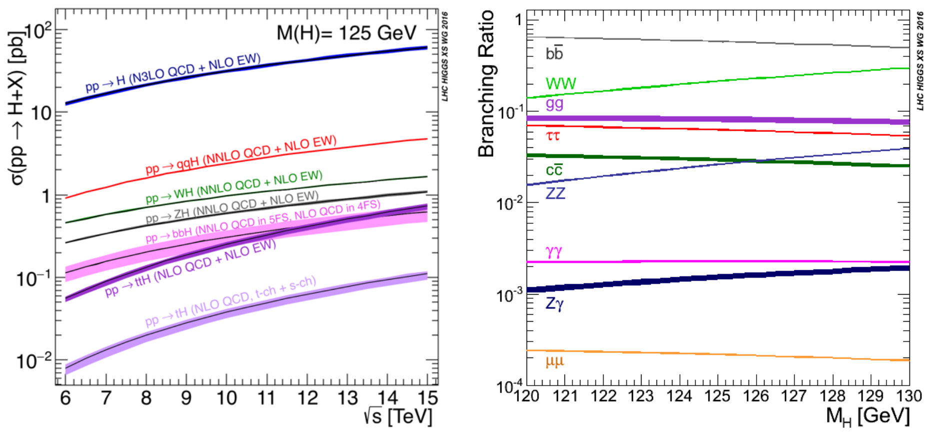

Figure 2.12: Higgs boson production cross sections (left) and decay branching ratios (right) for the main mechanisms. The VBF is indicated as qqH [36].

the biggest. Note that in this process, the Higgs boson is produced alone, which makes this mechanism experimentally clean when combined with the two-photon or the four-lepton decay channels (see section 2.3.7).

Vector boson fusion (figure 2.11b and $pp \to qqH$ in figure 2.12) has the second largest production cross section. The scattering of two fermions is mediated by a weak gauge boson which later emits a Higgs boson. In the final state, the two fermions tend to be located in a particular region of the detector which is used as a signature when analyzing the datasets provided by the experiments. More details about how to identify events of interest in an analysis will be given in chapter 6.

The next production mechanism is Higgs-strahlung (figure 2.11c and $pp \to WH, pp \to ZH$ in figure 2.12) where two fermions annihilate to form a weak gauge boson. If the initial fermions have enough energy, the emergent boson eventually will emit a Higgs boson.

The associated production with a top or bottom quark pair and the associated production with a single top quark (figure 2.11d-f and $pp \to bbH, pp \to t\bar{t}H, pp \to tH$ in figure 2.12) have a smaller cross section than the main three mechanisms above, but they provide a good opportunity to test the Higgs-top coupling. The analysis reported in this thesis is developed using these production mechanisms. A detailed description of the tHmechanism will be given in section 2.4.

2.3.7 Higgs boson decay channels

When a particle can decay throught several modes, also known as channels, the probability of decaying throught a given channel is quantified by the "branching ratio (BR)" of the decay channel; thus, the BR is defined as the ratio of number of decays going throught that given channel to the total number of decays. In regard to the Higgs boson decay, the BR can be predicted with accuracy once the Higgs mass is known [37, 38]. In figure 2.12 right, a plot of the BR as a function of the Higgs mass is presented. The largest predicted BR corresponds to the $b\bar{b}$ pair decay channel (see table 2.9).

Decay channel	Branching ratio	Rel. uncertainty
$H \to b\bar{b}$	5.84×10^-1	$+3.2\% - 3.3\%$
$H \to W^+W^-$	2.14×10^-1	$+4.3\% - 4.2\%$
$H \to \tau^+\tau^-$	6.27×10^-2	$+5.7\% - 5.7\%$
$H \to ZZ$	2.62×10^-2	$+4.3\% - 4.1\%$
$H \to \gamma\gamma$	2.27×10^-3	$+5.0\% - 4.9\%$
$H \to Z\gamma$	1.53×10^-3	$+9.0\% - 8.9\%$
$H \to \mu^+\mu^-$	2.18×10^-4	$+6.0\% - 5.9\%$

Table 2.9: Predicted branching ratios and the relative uncertainty for a SM Higgs boson with $m_H = 125 GeV/c^2$. [9]

2.4 Associated production of a Higgs boson and a single Top quark.

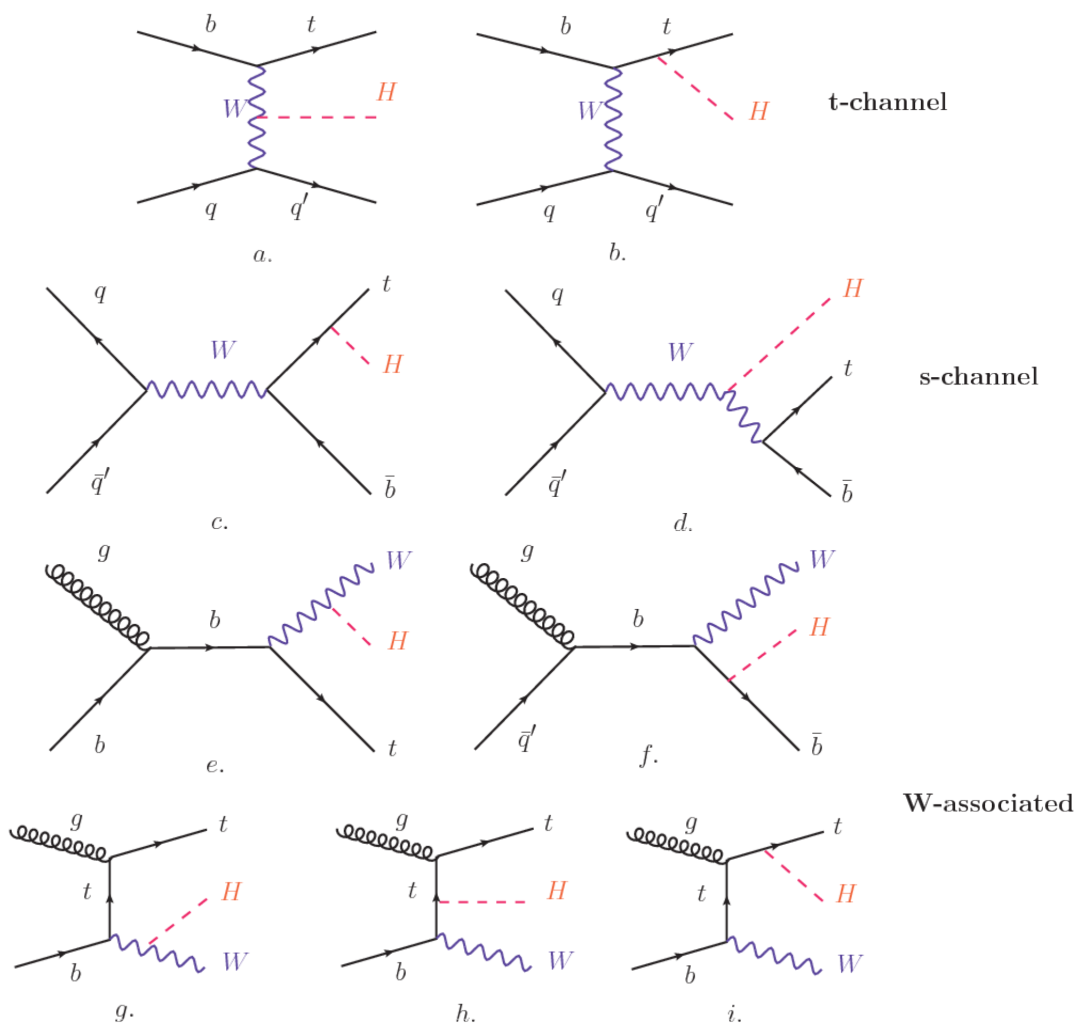

Figure 2.13: Associated Higgs boson production mechanism Feynman diagrams. a.,b. t-channel (tHq), c.,d. s-channel (tHb), e-i. W-associated.

Associated production of Higgs boson has been extensively studied [39–43]. While measurements of the main Higgs production mechanisms rates are sensitive to the strength of the Higgs coupling to W boson or top quark, they are not sensitive to the relative sign between the two couplings. In this thesis, the Higgs boson production mechanism explored is the associated production with a single top quark (tH) which offers sensitiveness to the relative sign of the Higgs couplings to W boson and to top quark. The description given here is based on the reference [41]

A process where two incoming particles interact and produce a final state with two particles can proceed in three ways also called channels (see, for instance, figure 2.13 ommiting the red line). The t-channel represents processes where an intermediate particle is emited by one of the incoming particles and absorbed by the other. The s-channel represents processes where the two incoming particles merge into an intermediate particle which eventually will split into the particles in the final state. The third channel, u-channel, is similar to the t-channel but the two outgoing particles interchange their roles.

The tHproduction, where Higgs boson can be radiated either from the top quark or from the W boson, is represented by the leading order Feynman diagrams in figure **??**. The cross section for the tHprocess is calculated, as usual, summing over the contributions from the different feynman diagrams; therefore it depends on the interference between the contributions. In the SM, the interference for t-channel (tHq process) and W-associated (tHW process) production is destructive [39] resulting in the small cross sections presented in table 2.10.

tH production channel	Cross section (fb)
t-channel ($pp \to tHq$)	$70.79^{+2.99}_{-4.80}$
W-associated ($pp \to tHW$)	$15.61^{+0.83}_{-1.04}$
s-channel($pp \to tHb$)	$2.87^{+0.09}_{-0.08}$

Table 2.10: Predicted SM cross sections for tHproduction at $\sqrt{s} = 13$ TeV [44, 45].

While the s-channel contribution can be neglected, it will be shown that a deviation from the SM destructive interference would result in an enhancement of the tHcross section compared to that in SM, which could be used to get information about the sign of the Higgs-top coupling [41, 42]. In order to describe tHproduction processes, Feynman diagram 2.13b will be considered; there, the W boson is radiated by a quark in the proton and eventually it will interact with the b quark. In the high energy regime, the effective W approximation [46] allows to describe the process as the emmision of an approximately on-shell W and its hard scattering with the b quark; i.e. $Wb \to th$. The scattering amplitude for the process is given by

$$\mathcal{A} = \frac{g}{\sqrt{2}} \left[(\kappa_t - \kappa_V) \frac{m_t \sqrt{s}}{m_W v} A\left(\frac{t}{s}, \varphi; \xi_t, \xi_b\right) + \left(\kappa_V \frac{2m_W}{v} \frac{s}{t} + (2\kappa_t - \kappa_V) \frac{m_t^2}{m_W v}\right) B\left(\frac{t}{s}, \varphi; \xi_t, \xi_b\right) \right], \tag{2.57}$$

where $\kappa_V \equiv g_{HVV}/g_{HVV}^{SM}$ and $\kappa_t \equiv g_{Ht}/g_{Ht}^{SM} = y_t/y_t^{SM}$ are scaling factors that quantify possible deviations of the couplings, Higgs-Vector boson (H-W) and Higgs-top (H-t) respectively, from the SM couplings; $s = (p_W + p_b)^2$, $t = (p_W - p_H)^2$, φ is the Higgs azimuthal angle around the z axis taken parallel to the direction of motion of the incoming W; A and B are funtions describing the weak interaction in terms of the chiral states of the quarks b and t. Terms that vanish in the high energy limit have been neglected as well as the Higgs and b quark masses[8].

The scattering amplitude grows with energy like $\sqrt{s}$ for $\kappa_V \neq \kappa_t$, in contrast to the SM ($\kappa_t = \kappa_V = 1$), where the first term in 2.57 cancels out and the amplitude is constant for large s; therefore, a deviation from the SM predictions represents an enhancement in the tHq cross section. In particular, for a SM H-W coupling and a H-t

[8] A detailed explanation of the structure and approximations used to derive $\mathcal{A}$ can be found in reference [41]

coupling of inverted sigh with respect to the SM ($\kappa_V = -\kappa_t = 1$) the tHq cross section is enhanced by a factor greater 10 as seen in the figure 2.14 taken from reference [41]; reference [47] has reported similar enhancement results.

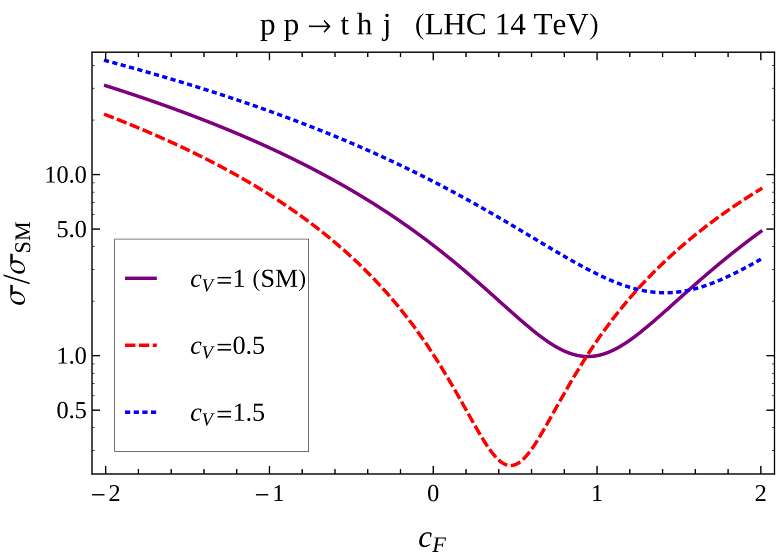

Figure 2.14: Cross section for tHq process as a function of κ_t, normalized to the SM, for three values of κ_V. In the plot c_f refers to the Higgs-fermion coupling which is dominated by the H-t coupling and represented here by κ_t. Solid, dashed and dotted lines correspond to $c_V \to \kappa_V = 1, 0.5, 1.5$ respectively. Note that for the SM ($\kappa_V = \kappa_t = 1$), the destructive effect of the interference is maximal.

A similar analysis is valid for the W-associated channel but, in that case, the interference is more complicated since there are more than two contributions and an additional interference with the production of Higgs boson and a top pair process($t\bar{t}H$). The calculations are made using the so-called Diagram Removal (DR) technique where interfering diagrams are removed (or added) from the calculations in order to evaluate the impact of the removed contributions. DR1 was defined to neglect $t\bar{t}H$ interference while DR2 was defined to take $t\bar{t}H$ interference into account [48]. As shown in figure 2.15, the tHW cross section is enhanced from about 15 fb (SM: $\kappa_{Htt} = 1$) to about 150 fb ($\kappa_{Htt} = -1$). Differences between curves for DR1 and DR2 help to gauge the impact of the interference with $t\bar{t}H$.

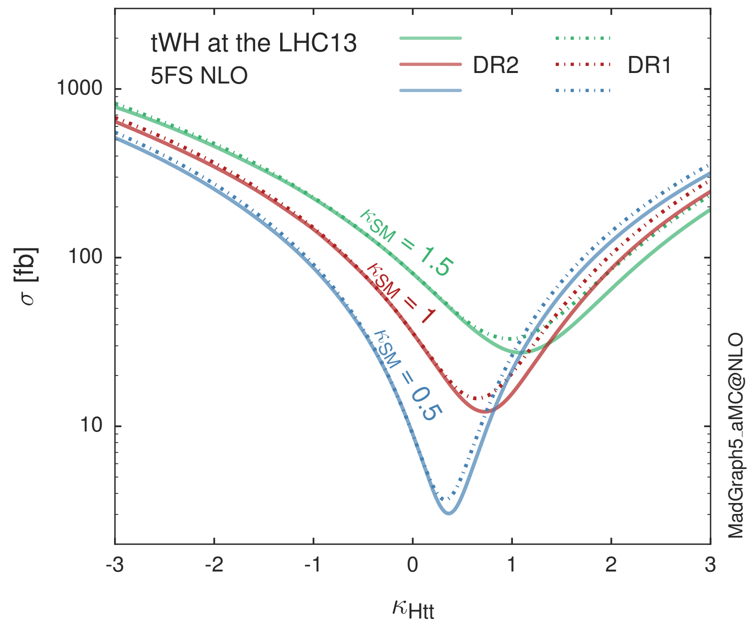

Figure 2.15: Cross section for tHW process as a function of κ_{Htt}, for three values of κ_{SM} at $\sqrt{s} = 13$ TeV. $\kappa^2_{Htt} = \sigma_{Htt}/\sigma^{SM}_{Htt}$ is a simple rescaling of the SM Higgs interactions.

Results of the calculations of the tHq and tHW cross sections at $\sqrt{s} = 13$ TeV can be found in reference [49] and a summary of the results is presented in table 2.11.

2.5 The CP-mixing in tH processes

In addition to the sensitivity to sign of the H-t coupling, tHq and tHW processes have been proposed as a tool to investigate the possibility of a H-t coupling that does not conserve CP [43, 48, 50]. Current experimental results are consistent with SM H-V and H-t couplings; however, negative H-t coupling is not excluded completely [53].

In this thesis, the sensitivity of tH processes to CP-mixing is also studied in the effective field theory framework and based in references [43, 48]; a generic particle

	$\sqrt{s}$ TeV	$\kappa_t = 1$	$\kappa_t = -1$
$\sigma^{LO}(tHq)$(fb) [41]	8	≈ 17.4	≈ 252.7
	14	≈ 80.4	≈ 1042
$\sigma^{NLO}(tHq)$(fb) [41]	8	$18.28^{+0.42}_{-0.38}$	$233.8^{+4.6}_{-0.0}$
	14	$88.2^{+1.7}_{-0.0}$	$982.8^{+28}_{-0.0}$
$\sigma^{LO}(tHq)$(fb) [47]	14	≈ 71.8	≈ 893
$\sigma^{LO}(tHW)$(fb) [47]	14	≈ 16.0	≈ 139
$\sigma^{NLO}(tHq)$(fb) [49]	8	$18.69^{+8.62\%}_{-17.13\%}$	-
	13	$74.25^{+7.48\%}_{-15.35\%}$	$848^{+7.37\%}_{-13.70\%}$
	14	$90.10^{+7.34\%}_{-15.13\%}$	$1011^{+7.24\%}_{-13.39\%}$
$\sigma^{LO}(tHW)$(fb) [48]	13	$15.77^{+15.91\%}_{-15.76\%}$	-
$\sigma^{NLO}DR1(tHW)$(fb) [48]	13	$21.72^{+6.52\%}_{-5.24\%}$	≈ 150
$\sigma^{NLO}DR2(tHW)$(fb) [48]	13	$16.28^{+7.34\%}_{-15.13\%}$	≈ 150

Table 2.11: Predicted enhancement of the tHq and tHWcross sections at LHC for $\kappa_V = 1$ and $\kappa_t = \pm 1$ at LO and NLO; the cross section enhancement of more that a factor of 10 is due to the flippling in the sign of the H-t coupling with respect to the SM one.

(X_0) of spin-0 and a general CP violating interaction with the top quark, can couple to scalar and pseudoscalar fermionic densities. The H-W interaction is assumed to be SM-like. The Lagrangian modeling the H-t interaction is given by

$$\mathcal{L}_0^t = -\bar{\psi}_t \left(c_\alpha \kappa_{Htt} g_{Htt} + i s_\alpha \kappa_{Att} g_{Att} \gamma_5\right) \psi_t X_0, \tag{2.58}$$

where α is the CP-mixing phase, $c_\alpha \equiv \cos\alpha$ and $s_\alpha \equiv \sin\alpha$, κ_{Htt} and κ_{Att} are real dimensionless rescaling parameters[9], $g_{Htt} = g_{Att} = m_t/v = y_t/\sqrt{2}$ and $v \sim 246$ GeV is the Higgs vacuum expectation value. In this parametrization, it is easy to recover three special cases

- CP-even coupling $\rightarrow \alpha = 0^o$
- CP-odd coupling $\rightarrow \alpha = 90^o$
- SM coupling $\rightarrow \alpha = 0^o$ and $\kappa_{Htt} = 1$

[9] analog to κ_t and κ_V

The loop induced X_0 coupling to gluons can also be described in terms of the parametrization above, according to

$$\mathcal{L}_0^g = -\frac{1}{4}\left(c_\alpha \kappa_{Hgg} g_{Hgg} G^a_{\mu\nu} G^{a,\mu\nu} + s_\alpha \kappa_{Agg} g_{Agg} G^a_{\mu\nu} \widetilde{G}^{a,\mu\nu}\right) X_0. \tag{2.59}$$

where $g_{Hgg} = -\alpha_s/3\pi v$ and $g_{Agg} = \alpha_s/2\pi v$. Under the assumption that the top quark dominates the gluon-fusion process at LHC energies, $\kappa_{Hgg} \to \kappa_{Htt}$ and $\kappa_{Agg} \to \kappa_{Att}$, so that the ratio between the gloun-gluon fusion cross section for X_0 and for the SM Higgs prediction can be written as

$$\frac{\sigma^{gg\to X_0}_{NLO}}{\sigma^{gg\to H}_{NLO,SM}} = c_\alpha^2 \kappa_{Htt}^2 + s_\alpha^2 \left(\kappa_{Att} \frac{g_{Agg}}{g_{Hgg}}\right)^2. \tag{2.60}$$

If the rescaling parameters are set to

$$\kappa_{Htt} = 1, \qquad \kappa_{Att} = \left|\frac{g_{Hgg}}{g_{Agg}}\right| = \frac{2}{3}. \tag{2.61}$$

the gluon-fusion SM cross section is reproduced for every value of the CP-mixing angle α; therefore, by imposing that condition to the Lagrangian density 2.58, the CP-mixing angle is not constrained by current data. Figure 2.16 shows the NLO cross sections for t-channel tX_0(blue) and $t\bar{t}X_0$ (red) associated production processses as a function of the CP-mixing angle α. X_0 is a generic spin-0 particle with top quark CP-violating coupling. Rescaling factors κ_{Htt} and κ_{Att} have been set to reproduce the SM gluon-fusion cross sections.

It is interesting to notice that the tX_0 croos section is enhanced, by a factor of about 10, when a continuous rotation in the scalar-pseudoscalar plane is applied; this enhancement is similar to the enhancement produced when the H-t coupling is flipped in sign with respect to the SM ($y_t = -y_{t,SM}$ in the plot), as showed in section 2.4. In

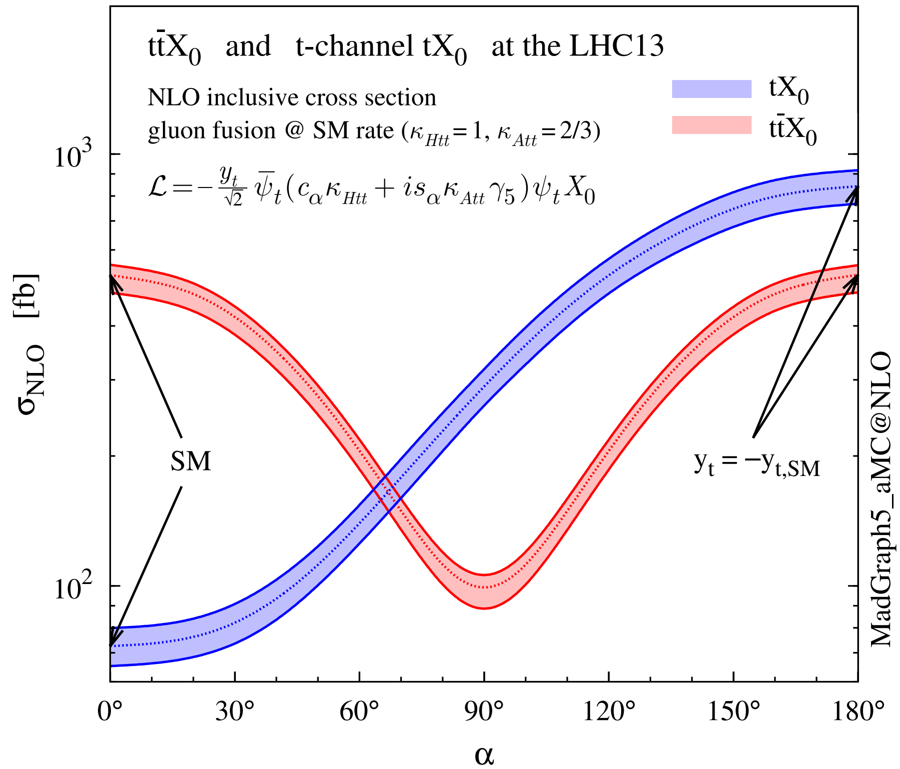

Figure 2.16: NLO cross sections for t-channel tX_0(blue) and $t\bar{t}X_0$ (red) associated production processses as a function of the CP-mixing angle α. X_0 is a generic spin-0 particle with top quark CP-violating coupling [43].

contrast, the degeneracy in the $t\bar{t}X_0$ cross section is still present given that it depends quadratically on the H-t coupling, but more insterting is to notice that $t\bar{t}X_0$ cross section is exceeded by tX_0 cross section after $\alpha \sim 60^o$.

A similar parametrization can be used to investigate the tHW process sensitivity to CP-violating H-t coupling. As said in 2.4, the interference in the W-associated channel is more complicated because there are more than two contributions and also there is interference with the $t\bar{t}H$ production process.

Figure 2.17 shows the NLO cross sections for t-channel tX_0(blue), $t\bar{t}X_0$ (red) associated production and for the combined $tWX_0 + t\bar{t}X_0+$ interference (orange) as a

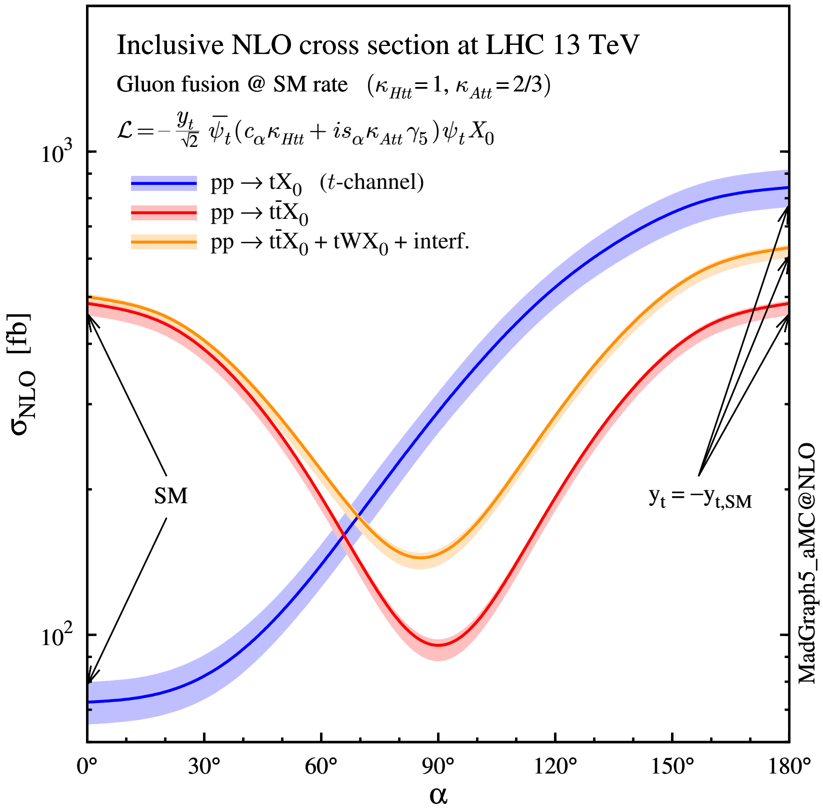

Figure 2.17: NLO cross sections for t-channel tX_0(blue), $t\bar{t}X_0$ (red) associated production processses and combined $tWX_0 + t\bar{t}X_0$ (including interference) production as a function of the CP-mixing angle α [43].

function of the CP-mixing angle. It is clear that the effect of the interference in the combined case is the lifting of the degeneracy present in the $t\bar{t}X_0$ production. The constructive interference enhances the cross section from about 500 fb at SM ($\alpha = 0$) to about 600 fb ($\alpha = 180^o \rightarrow y_t = -y_{t,SM}$).

An analysis combining tHq and tHWprocesses will be made in this thesis taking advantage of the sensitivity improvement.

2.6 Experimantal status of the anomalous Higg-fermion coupling.

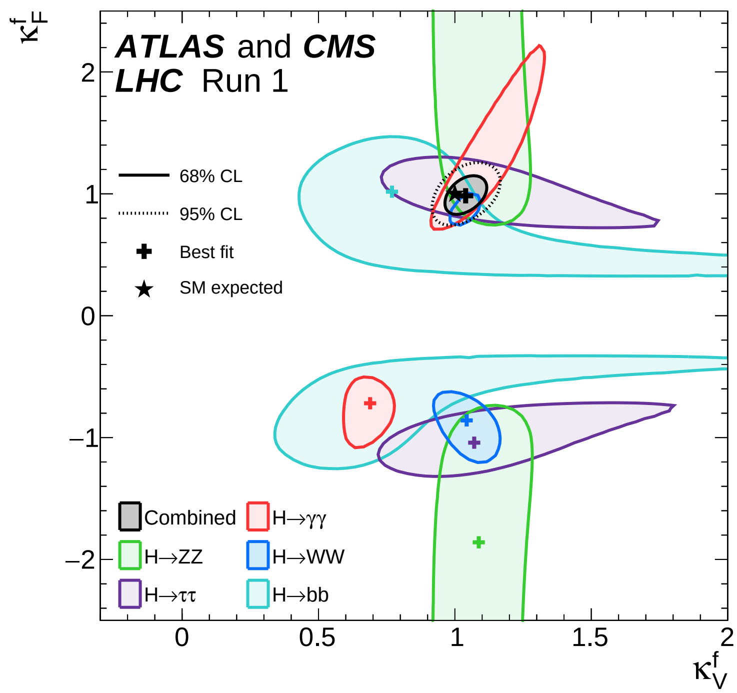

Figure 2.18: Combination of the ATLAS and CMS fits for coupling modifiers κ_t-κ_V; also shown the individual decay channels combination and their global combination. No assumptions have been made on the sign of the coupling modifiers [53].

ATLAS and CMS have performed analysis of the anomalous H-f coupling by making likelihood scans for the two coupling modifiers, κ_t and κ_V, under the assumption that $\kappa_Z = \kappa_W = \kappa_V$ and $\kappa_t = \kappa_\tau = \kappa_b = \kappa_f$. Figure2.18 shows the result of the combination of ATLAS and CMS fits; also the individual decay channels combination and the global combination results are shown.

While all the channels are compatible for positive values of the modifiers, for negative values of κ_t there is no compatibility. The best fit for individual channels is compatible with negative values of κ_t except for the $H \to bb$ channel which is expected to be the most sensitive channel; therefore, the best fit for the global fit yields $\kappa_t \geq 0$. Thus, the anomaluos H-t coupling cannot be excluded completely.

Chapter 3

The CMS experiment at the LHC

3.1 Introduction

Located on the Swiss-French border, the European Council for Nuclear Research (CERN) is the largest scientific organization leading the particle physics research. About 13000 people in a broad range of fields including users, students, scientists, engineers, among others, contribute to the data taking and analysis, with the goal of unveiling the secrets of nature and revealing the fundamental structure of the universe. CERN is also the home of the Large Hadron Collider (LHC), the largest circular particle accelerator around the world, where protons (or heavy ions) traveling close to the speed of light, are made to collide. These collisions open a window to investigate how particles (and their constituents if they are composite) interact with each other, providing clues about the laws of nature. This chapter presents an overview of the LHC structure and operation. A detailed description of the CMS detector is offered, given that the data used in this thesis have been taken with this detector.

3.2 The LHC

With 27 km of circumference, the LHC is currently the largest and most powerful circular accelerator in the world. It is installed in the same tunnel where the Large Electron-Positron (LEP) collider was located, taking advantage of the existing infrastructure. The LHC is also the larger accelerator in the CERN's accelerator complex and is assisted by several successive accelerating stages before the particles are injected into the LHC ring where they reach their maximum energy (see figure 3.1).

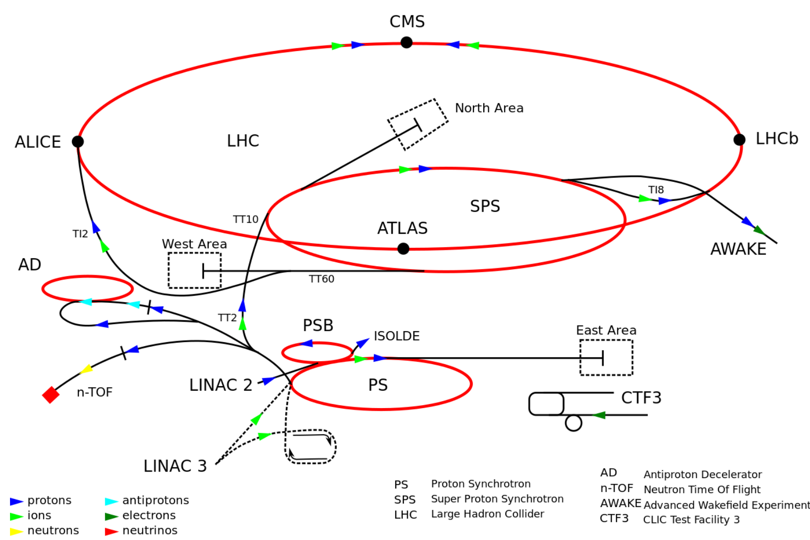

Figure 3.1: CERN accelerator complex. Blue arrows show the path followed by protons along the acceleration process [54].

LHC runs in three modes depending on the particles being accelerated

- Proton-Proton collisions (*pp*) for multiple physics experiments.
- Lead-Lead collisions (Pb-Pb) for heavy ion experiments.
- Proton-Lead collisions (p-Pb) for quark-gluon plasma experiments.

In this thesis only *pp* collisions will be considered.

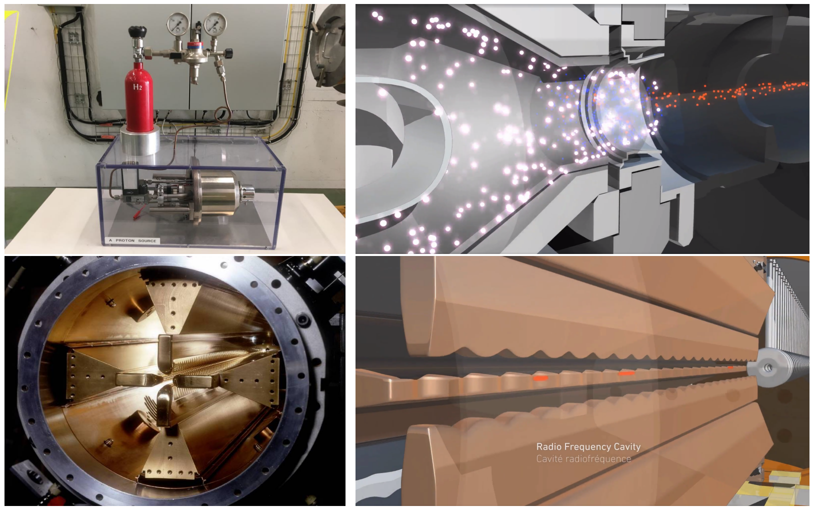

Figure 3.2: LHC protons source and the first acceleration stage. Top: the bottle contains hydrogen gas (white dots) which is injected into the metal cylinder to be broken down into electrons(blue dots) and protons(red dots); Bottom: the obtained protons are directed towards the radio frequency quadrupole which perform the first acceleration, focus the beam and create the bunches of protons. [58, 59]

Collection of protons starts with hydrogen atoms taken from a bottle, containing hydrogen gas, and injecting them in a metal cylinder; hydrogen atoms are broken down into electrons and protons by an intense electric field (see figure3.2 top). The resulting protons leave the metal cylinder towards a radio frequency quadrupole (RFQ) that focus the beam, accelerates the protons and creates the packets of protons called bunches. In the RFQ, an electric field is generated by a RF wave at a frequency that matches the resonance frequency of the cavity where the electrodes are contained. The beam of protons traveling on the RFQ axis experiences an alternating electric field gradient that generates the focusing forces.

In order to accelerate the protons, a longitudinal time-varying electric field component is added to the system; it is done by giving the electrodes a sinus-like profile as shown in figure 3.2 bottom. By matching the speed and phase of the protons with the longitudinal electric field the bunching is performed; protons synchronized with the

RFQ (synchronous proton) do not feel an accelerating force, but those protons in the beam that have more (or less) energy than the synchronous proton (asynchronous protons) will feel a decelerating (accelerating) force; therefore, asynchronous protons will oscillate around the synchronous ones forming bunches of protons [56]. From the RFQ protons emerge with energy 750 keV in bunches of about 1.15×10^{11} protons [57].

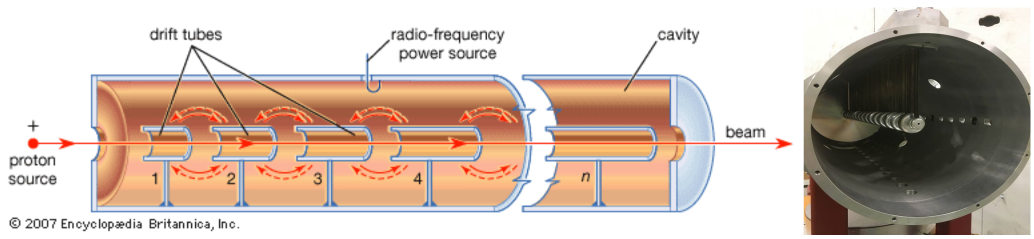

Figure 3.3: The LINAC2 accelerating system at CERN. Electric fields generated by radio frequency (RF) create acceleration and deceleration zones inside the cavity; deceleration zones are blocked by drift tubes where quadrupole magnets focus the proton beam. [60]

Proton bunches coming from the RFQ go to the linear accelerator 2 (LINAC2) where they are accelerated to reach 50 MeV energy. In the LINAC2 stage, acceleration is performed using electric fields generated by radio frequency which create zones of acceleration and deceleration as shown in figure 3.3. In the deceleration zones, the electric field is blocked using drift tubes where protons are free to drift while quadrupole magnets focus the beam.

The beam coming from LINAC2 is injected into the proton synchrotron booster (PSB) to reach 1.4 GeV in energy. The next acceleration is provided at the proton synchrotron (PS) up to 26 GeV, followed by the injection into the super proton synchrotron (SPS) where protons are accelerated to 450 GeV. Finally, protons are injected into the LHC where they are accelerated to the target energy of 6.5 TeV. PSB, PS, SPS and LHC accelerate protons using the same RF acceleration technique described before.

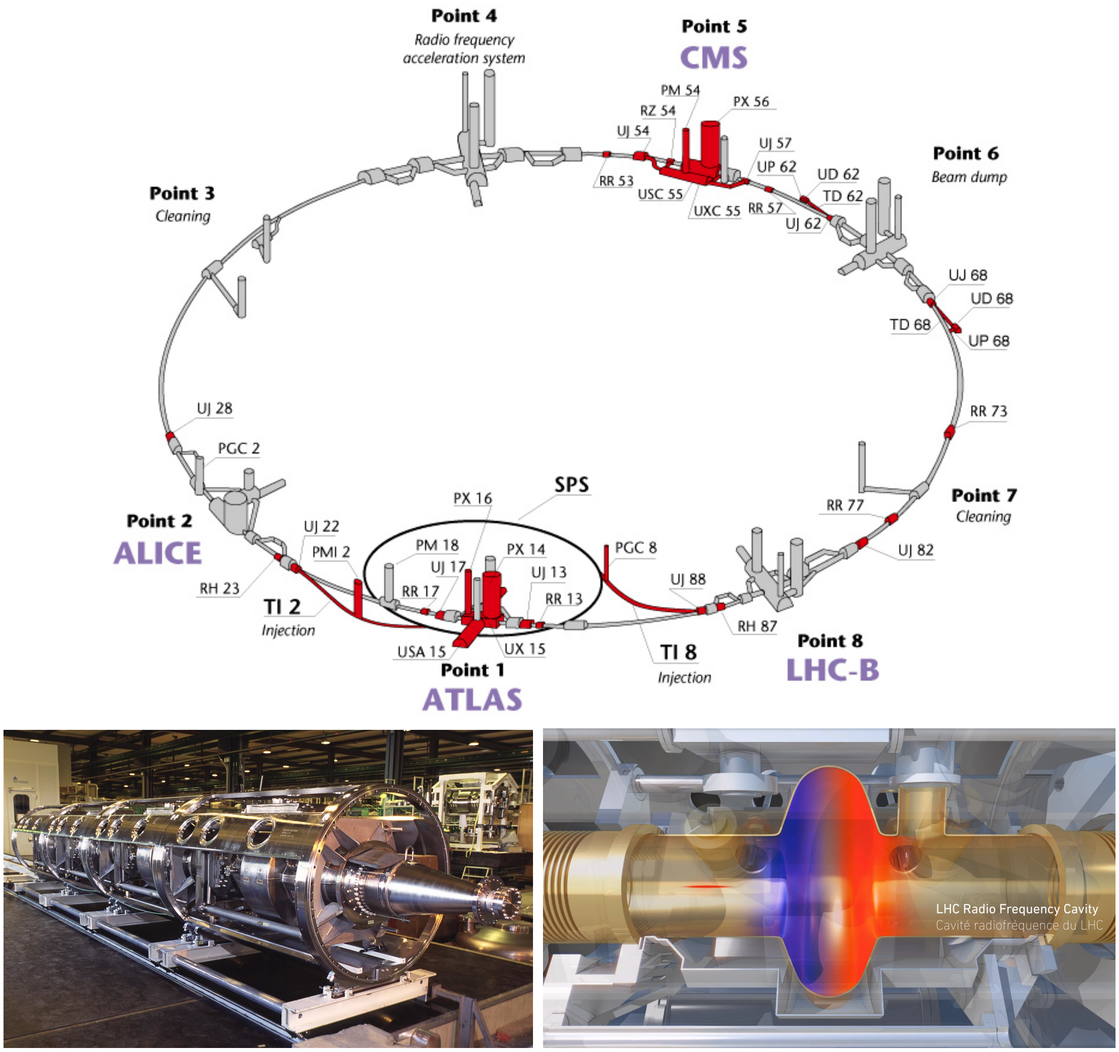

Figure 3.4: Top: LHC layout. The red zones indicate the infrastructure additions to the LEP installations, built to accommodate the ATLAS and CMS experiments which exceed the size of the former experiments located there [55]. Bottom: LHC RF cavities. A module accommodates 4 cavities that accelerate protons and preserve the bunch structure of the beam. [59, 61]

LHC has a system of 16 RF cavities located in the so-called point 4, as shown in figure 3.4 top, tuned at a frequency of 400 MHz and the protons are carefully timed, so in addition to the acceleration effect the bunch structure of the beam is preserved. Bottom side of figure 3.4 shows a picture of a RF module composed of 4 RF cavities working in a superconducting state at 4.5 K; also is showed a representation of the accelerating electric field that accelerates the protons in the bunch.

While protons are accelerated in one section of the LHC ring, where the RF cavities are located, in the rest of their path they have to be kept in the curved trajectory defined by the LHC ring. Technically, LHC is not a perfect circle; RF, injection, beam dumping, beam cleaning and sections before and after the experimental points where protons collide are all straight sections. In total, there are 8 arcs 2.45 Km long each and 8 straight sections 545 m long each. In order to curve the proton's trajectory in the arc sections, superconducting dipole magnets are used.

Inside the LHC ring, there are two proton beams traveling in opposite directions in two separated beam pipes; the beam pipes are kept at ultra-high vacuum ($\sim 10^{-9}$ Pa) to ensure that there are no particles that interact with the proton beams. The superconducting dipole magnets used in LHC are made of a NbTi alloy, capable of transporting currents of about 12000 A when cooled at a temperature below 2K using liquid helium (see figure 3.5).

Protons in the arc sections of LHC feel a centripetal force exerted by the dipole magnets which is perpendicular to the beam trajectory; The magnitude of magnetic field needed can be found assuming that protons travel at $v \approx c$, using the standard values for proton mass and charge and the LHC radius, as

$$F_m = \frac{mv^2}{r} = qBv \quad \rightarrow B = 8.33T \tag{3.1}$$

which is about 100000 times the Earth's magnetic field. A representation of the magnetic field generated by the dipole magnets is shown on the bottom left side of figure

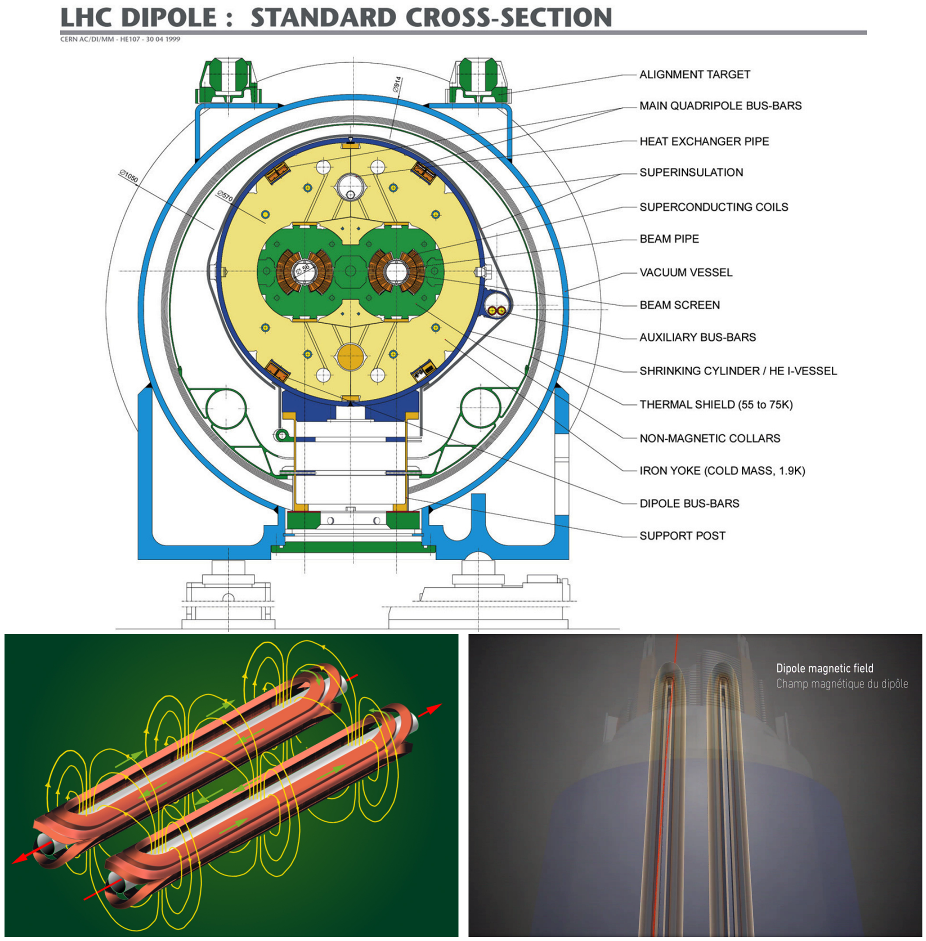

Figure 3.5: Top: LHC dipole magnet transverse view; cooling, shielding and mechanical support are indicated. Bottom left: Magnetic field generated by the dipole magnets; note that the direction of the field inside one beam pipe is opposite with respect to the other beam pipe which guarantee that both proton beams are curved in the same direction towards the center of the ring. The effect of the dipole magnetic field on the proton beam is represented on the bottom right side [59, 62, 63].

3.5. The bending effect of the magnetic field on the proton beam is shown on the bottom right side of figure 3.5. Note that the dipole magnets are not curved; the arc section of the LHC ring is composed of straight dipole magnets of about 15 m. In total there are 1232 dipole magnets along the LHC ring.

In addition to bending the beam trajectory, the beam has to be focused so it stays inside the beam pipe. The focusing is performed by quadrupole magnets installed in a different straight section; in total 858 quadrupole magnets are installed along the LHC ring. Other effects like electromagnetic interaction among bunches, interaction with electron clouds from the beam pipe, the gravitational force on the protons, differences in energy among protons in the same bunch, among others, are corrected using sextupole and other magnetic multipoles.

The two proton beams inside the LHC ring are made of bunches with a cylindrical shape of about 7.5 cm long and about 1 mm in diameter; when bunches are close to the collision point (CP), the beam is focused up to a diameter of about 16 μm in order to maximize the number of collisions per unit area and per second, known as luminosity (L). Luminosity can be calculated using

$$L = fn\frac{N_1 N_2}{4\pi\sigma_x\sigma_y} \tag{3.2}$$

where f is the revolution frequency, n is the number of bunches per beam, N_1 and N_2 are the numbers of protons per bunch (1.5×10^{11}), σ_x and σ_y are the gaussian transverse sizes of the bunches. The expected luminosity is about

$$\begin{aligned} f =& \frac{v}{2\pi r_{LHC}} \approx \frac{3\times10^{8}\mathrm{m/s}}{27\mathrm{km}} \approx 11.1\mathrm{kHz}, \\ n =& 2808 \\ N_1 =& N_2 = 1.5\times10^{11} \\ \sigma_x =& \sigma_y = 16\mu\mathrm{m} \end{aligned}$$

$$L = 1.28\times10^{34}\mathrm{cm}^{-2}\mathrm{s}^{-1} = 1.28\times10^{-5}\mathrm{fb}^{-1}\mathrm{s}^{-1} \tag{3.3}$$

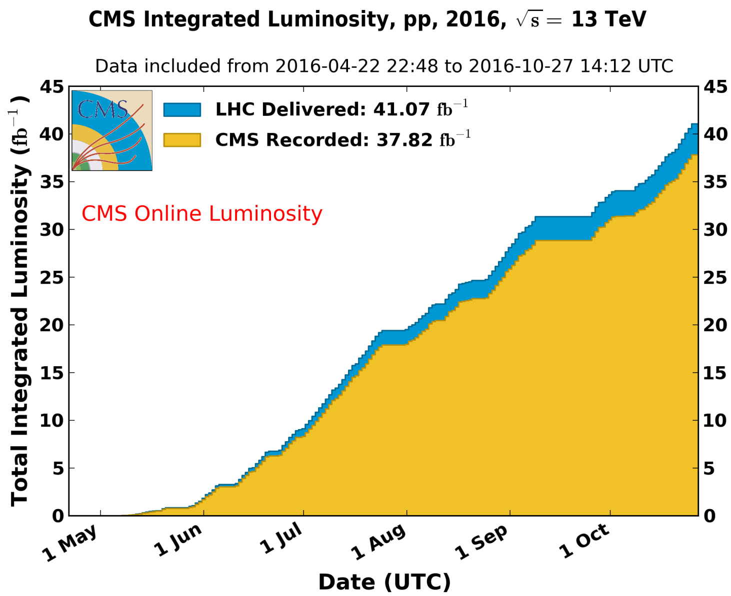

Figure 3.6: Integrated luminosity delivered by LHC and recorded by CMS during 2016. The difference between the delivered and the recorded luminosity is due to fails and issues occurred during the data taking in the CMS experiment [64].

Luminosity is a fundamental aspect of LHC given that the bigger luminosity the bigger number of collisions, which means that for processes with a very small cross section the number of expected occurrences is increased and so the chances of being detected. The integrated luminosity, i.e., the total luminosity, collected by the CMS experiment during 2016 is shown in figure 3.6; the data analyzed in this thesis corresponds to an integrated luminosity of 35.9 fb^{-1} at a center of mass-energy $\sqrt{s} = 13$ TeV.

A way to increase L is increasing the number of bunches in the beam. Currently, the separation between two consecutive bunches in the beam is 7.5 m which corresponds to a time separation of 25 ns. In the full LHC ring the allowed number of bunches is $n = 27\text{km}/7.5\text{m} = 3600$; however, there are some gaps in the bunch pattern intended for preparing the dumping and injection of the beam, thus, the proton beams are composed of 2808 bunches.

Once the proton beams reach the desired energy, they are brought to cross each other producing proton-proton collisions. The bunch crossing happens in precise places where the four LHC experiments are located, as seen in the top of figure 3.7. In 2008, the first set of collisions involved protons with $\sqrt{s} = 7$ TeV; the energy was increased to 8 TeV in 2012 and to 13 TeV in 2015.

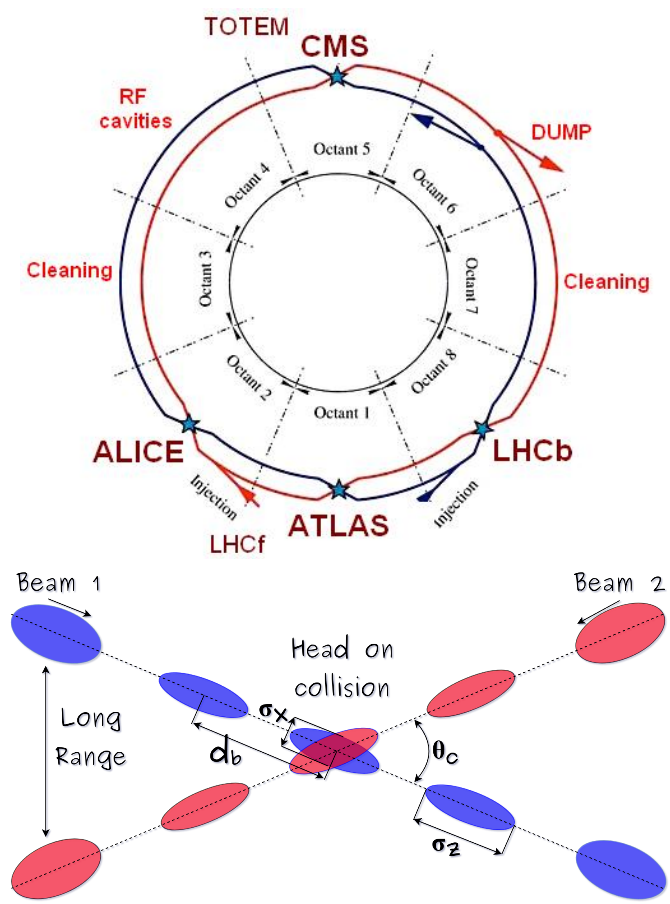

Figure 3.7: Top: LHC interaction points. Bunch crossing occurs where the LHC experiments are located [65]. Sections indicated as cleaning are dedicated to collimate the beam in order to protect the LHC ring from collisions with protons in very spreaded bunches. Bottom: bunch crossing scheme. Since the bunch crossing is not perfectly head-on, the luminosity is reduced in a factor of 17%; adapted from reference [77].

CMS and ATLAS experiments, which are multi-purpose experiments, are enabled to explore physics in any of the collision modes. LHCb experiment is optimized to explore bottom quark physics, while ALICE is optimized for heavy ion collisions searches; TOTEM and LHCf are dedicated to forward physics studies; MoEDAL (not indicated in the figure) is intended for monopoles or massive pseudo stable particles searches.

At the CP there are two interesting details that need to be addressed. The first one is that the bunch crossing does not occur head-on but at a small crossing angle "θ_c" (280 μrad in CMS and ATLAS) as shown in the bottom side of figure 3.7, affecting the overlapping between bunches; the consequence is a reduction of about 17% in the luminosity (represented by a factor not included in eqn: 3.2). The second one is the occurrence of multiple pp collisions in the same bunch crossing; this effect is called pile-up (PU). A fairly simple estimation of the PU follows from estimating the probability of collision between two protons, one from each of the bunches in course of collision; it depends roughly on the ratio of proton size and the cross section of the bunch in the interaction point, i.e.,

$$P(pp-collision) \sim \frac{d^2_{proton}}{\sigma_x \sigma_y} = \frac{(1\text{fm})^2}{(16\mu\text{m})^2} \sim 4\times 10^{-21} \qquad (3.4)$$

however, there are $N = 1.15\times 10^{11}$ protons in a bunch, thus the estimated number of collisions in a bunch crossing is

$$PU = N^2 * P(pp-collision) \sim 50\ pp\text{-collision per bunch crossing,} \qquad (3.5)$$

about 20 of those pp collisions are inelastic. Each collision generates a vertex, but only the most energetic is considered as a primary vertex; the rest are considered as

PU vertices. A multiple *pp* collision event in a bunch crossing at CMS is showed in figure3.8. Unstable particles outgoing from the primary vertex will eventually decay; this decay vertex is known as a secondary vertex.

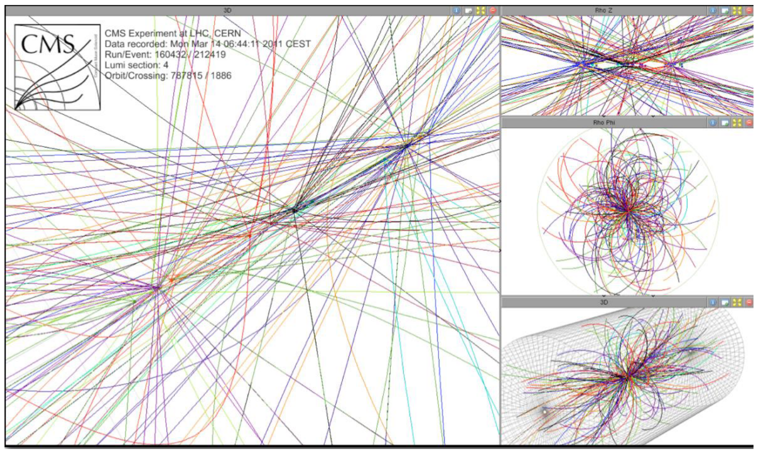

Figure 3.8: Multiple *pp* collision bunch crossing at CMS. Only the most energetic vertex is considered and the rest are cataloged as PU vertices [66].

Next section presents a description of the CMS detector which it is the detector used to collect the data used in this thesis.

3.3 The CMS experiment

CMS is a general-purpose detector designed to conduct research in a wide range of physics from the standard model to new physics like extra dimensions and dark matter. Located at the point 5 in the LHC layout as shown in figure 3.4, CMS is composed of several detection systems distributed in a cylindrical structure; in total, CMS weights about 12500 tons in a very compact 21.6 m long and 14.6 m diameter cylinder. It was built in 15 separate sections at the ground level and lowered to the cavern individually to be assembled. A complete and detailed description of the CMS detector and its components is given in reference [67] on which this section is based on.

Figure 3.9 shows the layout of the CMS detector. The design is driven by the requirements on the identification, momentum resolution and unambiguous charge determination of the muons; therefore, a large bending power is provided by the solenoid magnet made of superconducting cable capable to generate a 3.8 T magnetic field. The detection system is composed of (from the innermost to the outermost)

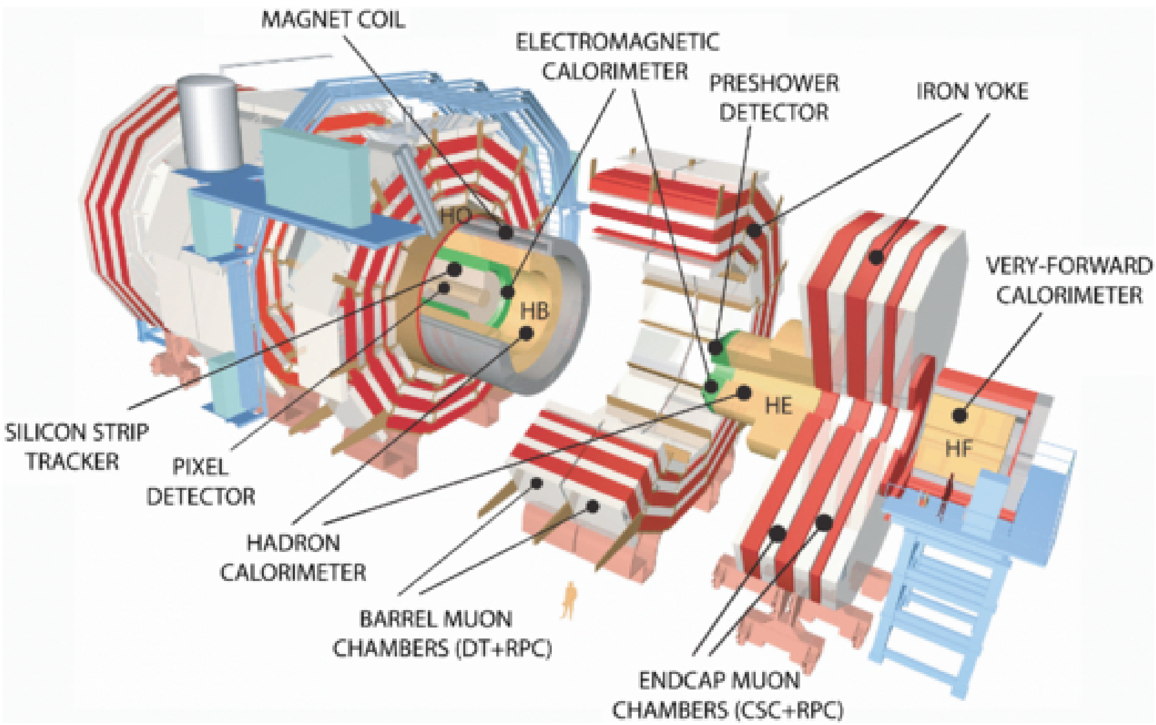

Figure 3.9: Layout of the CMS detector. The several subdetectors are indicated. The central region of the detector is referred as the Barrel section while the endcaps are referred as the forward sections. [68].

- Pixel detector.
- Silicon strip tracker.
- Preshower detector.

- Electromagnetic calorimeter.
- Hadronic calorimeter.
- Muon chambers (Barrel and endcap)

The central region of the detector is commonly referred as the barrel section while the endcaps are referred as the forward sections of the detector; thus, each subdetector is composed of a barrel section and a forward section.

3.3.1 Coordinate system

The coordinate system used by CMS is centered in the geometrical center of the detector which is the same as the CP as shown in figure3.10. The z-axis is parallel to the beam direction, while the Y-axis pointing vertically upward, and the X-axis pointing radially inward toward the center of the LHC.

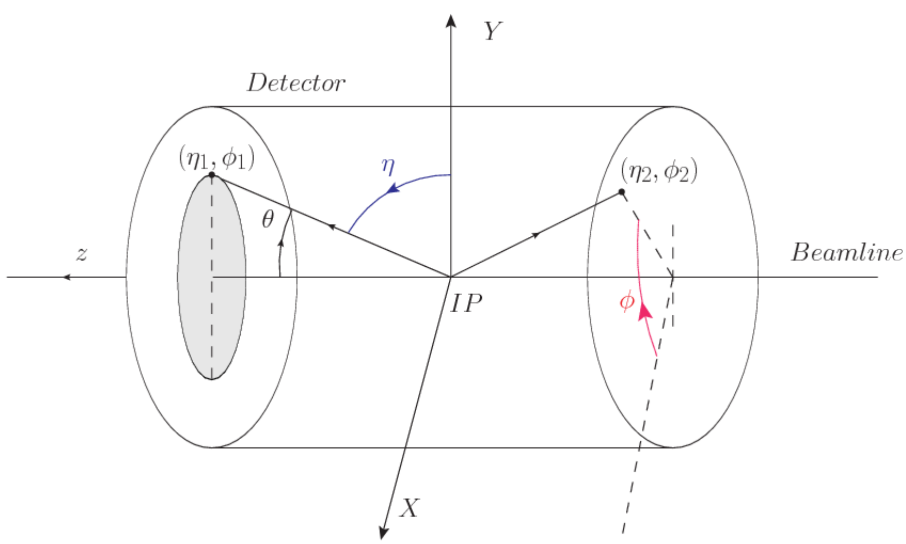

Figure 3.10: CMS detector coordinate system.

In addition to the common cartesian and cylindrical coordinate systems, two coordinates are of particular utility in particle physics: rapidity(y) and pseudorapidity(η), defined in connection to the polar angle θ, energy and longitudinal momentum component (momentum along the z-axis) according to

$$y = \frac{1}{2} ln \frac{E + p_z}{E - p_z} \qquad \eta = -ln\left(tan\frac{\theta}{2}\right) \tag{3.6}$$

Rapidity is related to the angle between the XY-plane and the direction in which the products of a collision are emitted; it has the nice property that the difference between the rapidities of two particles is invariant with respect to Lorentz boosts along the z-axis. Thus, data analysis becomes more simple when based on rapidity; however, it is not simple to measure the rapidity of highly relativistic particles, as those produced after pp collisions. Under the highly relativistic motion approximation, y can be rewritten in terms of the polar angle, concluding that rapidity is approximately equal to the pseudorapidity defined above, i.e., $y \approx \eta$. Note that η is easier to measure that y given the direct relationship between the former and the polar angle. Angular distance between two objects in the detector (ΔR) is defined in terms of their coordinates (η_1, ϕ_1), (η_2, ϕ_2) as

$$\Delta R = \sqrt{(\Delta\eta)^2 - (\Delta\phi)^2} \tag{3.7}$$

3.3.2 Pixels detector

The CMS tracking system is designed to provide a precise measurement of the trajectory (*track*) followed by the charged particles created after the pp collisions; also, the precise reconstruction of the primary and secondary origins (*vertices*) is expected in an environment where, each 25 ns, the bunch crossing produce about 20 inelastic collisions and about 1000 particles. An increment in the luminosity is ongoing which implies that the PU will increase accordingly.

The pixel detector was replaced during the 2016-2017 extended year-end technical stop, due to the increasingly challenging operating conditions like the higher particle flow and more radiation harsh environment, among others. The new one is responding as expected, reinforcing its crucial role in the successful way to fulfill the new LHC physics objectives after the discovery of the Higgs boson. The last chapter of this thesis is dedicated to describe my contribution to the " Forward Pixel Phase 1 upgrade".

The current pixel detector is composed of 1856 silicon pixel detector modules organized in four-barrel layers in the central region and three disks in the forward region; it is designed to record efficiently and with high precision, up to 10μm in the XY-plane and 20μm in the z-direction, the first four space-points (*hits*) near to the CP region (see figure 3.11 left side) in the range $|\eta| \leq 2.5$. The first barrel layer is located at a radius of 30 mm from the beamline, while the fourth layer is located at a radius of 160 mm closer to the strip tracker inner barrel layer (see section 3.3.3) in order to reduce the rate of fake tracks. The high granularity of the detector is represented in its about 123 Mpixels, each of size $100 \times 150 \mu\text{m}^2$, which is almost twice the channels of the old detector. The transverse momentum resolution of tracks can be measured with a resolution of 1-2% for muons of $p_T = 100$ GeV.

Some of the improvements with respect to the previous pixel detector include a higher average tracking efficiency and lower average fake rate as well as higher track impact parameter resolution which is fundamental in order to increase the efficiency in the identification of jets originating from b quarks (b-tagging). A significant source of improvement comes from the overall reduction in the material budget of the detector which results in fewer photon conversions and less multiple scattering from charged

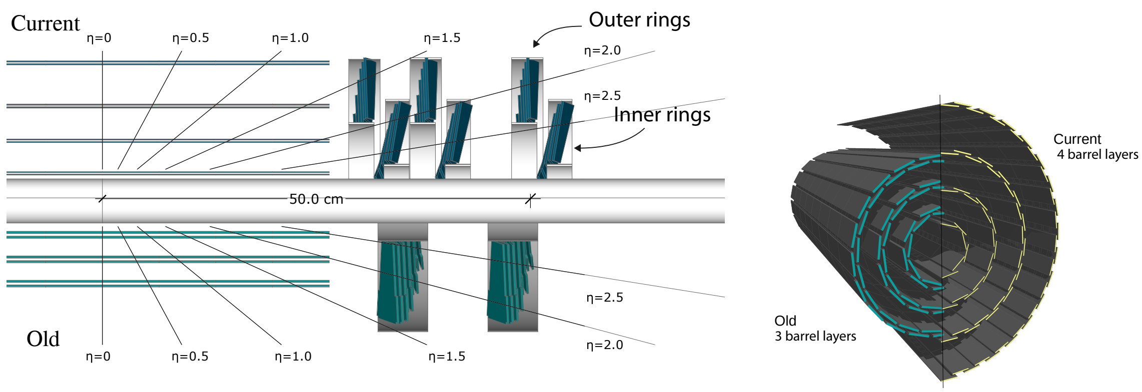

Figure 3.11: CMS pixel detector schematic view. Left: layout comparing the layers and disks in the old and current pixel detectors. Right: Transverse-oblique view comparing the pixel barrel layers in the two [70].

particles.

3.3.3 Silicon strip tracker

The silicon strip tracker (SST) is the second stage in the CMS tracking system. The top side of figure 3.12 shows a schematic of the SST. The inner tracker region is composed of the tracker inner barrel (TIB) and the tracker inner disks (TID) covering the region $r < 55$ cm and $|z| < 118$ cm. The TIB is composed of 4 layers while the TID is composed of 3 disks at each end. The silicon sensors in the inner tracker are 320 μm thick, providing a resolution of about 13-38 μm in the $r\phi$ position measurement.

The modules indicated in blue in the schematic view of figure 3.12 are two modules mounted back-to-back and rotated in the plane of the module by a “stereo” angle of 100 mrad; the hits from these two modules, known as “stereo hits”, are combined to provide a measurement of the second coordinate (z in the barrel and r on the disks) allowing the reconstruction of hit positions in 3-D.

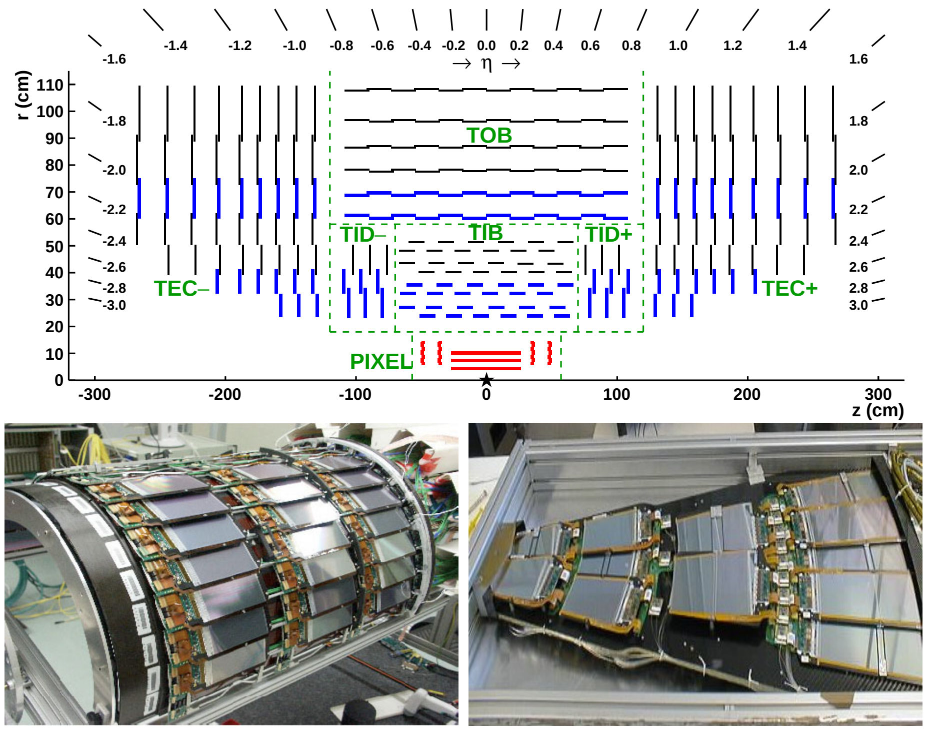

Figure 3.12: Top: CMS Silicon Strip Tracker (SST) schematic view. The SST is composed of the tracker inner barrel (TIB), the tracker inner disks (TID), the tracker outer barrel (TOB) and the tracker endcaps (TEC). Each part is made of silicon strip modules; the modules in blue represent two modules mounted back-to-back and rotated in the plane of the module by a stereo angle of 120 mrad in order to provide a 3-D reconstruction of the hit positions. Bottom: pictures of the TIB (left) and TEC (right) modules [71–73].

The outer tracker region is composed of the tracker outer barrel (TOB) and the tracker endcaps (TEC). The six layers of the TOB offer coverage in the region $r > 55$ cm and $|z| < 118$ cm, while the 9 disks of the TEC cover the region $124 < |z| < 282$ cm. The resolution offered by the outer tracker is about 13-38 μm in the $r\phi$ position measurement. The inner four TEC disks use silicon sensors 320 μm thick; those in the TOB and the outer three TEC disks use silicon sensors of 500 μm thickness. The silicon strips run parallel to the z-axis and the distance between strips varies from 80 μm in the inner TIB layers to 183 μm in the inner TOB layers; in the endcaps the wedge-shaped sensors with radial strips, whose pitch range between 81 μm at small radii and 205 μm at large radii.

The whole SST has 15148 silicon modules, 9.3 million silicon strips and cover a total active area of about 198 m^2.

3.3.4 Electromagnetic calorimeter

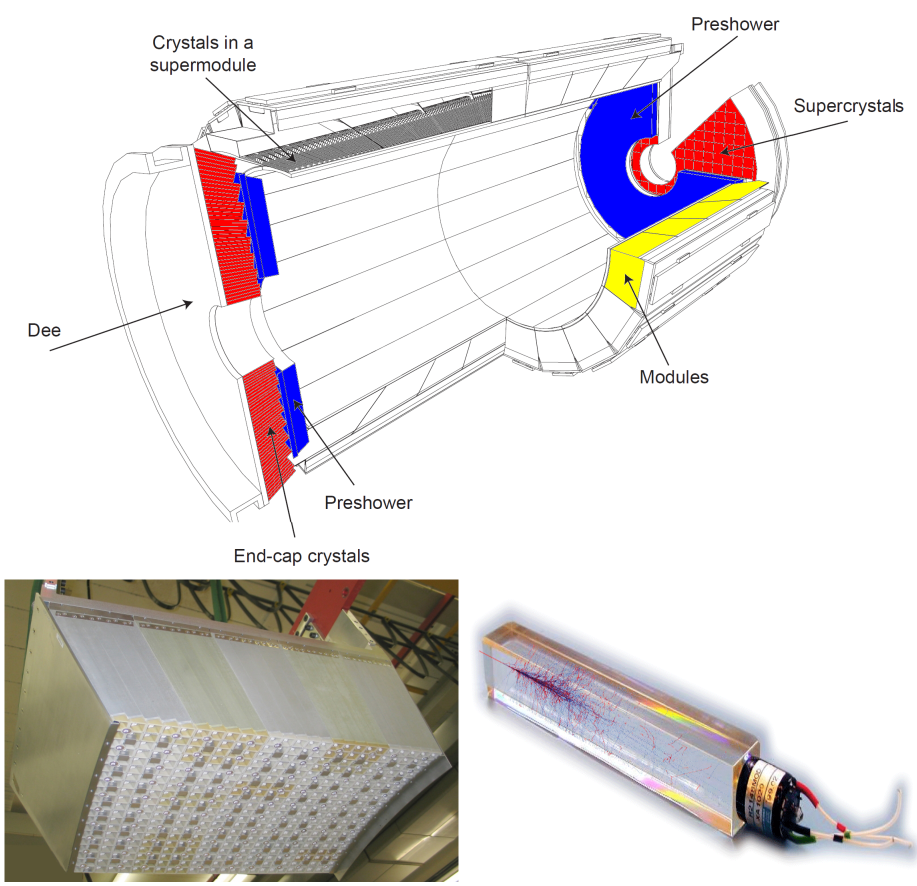

Figure 3.13: Top: CMS ECAL schematic view. Bottom: Module equipped with the crystals (left); ECAL crystal(right).

The CMS electromagnetic calorimeter (ECAL) is designed to measure the energy of electrons and photons. It is composed of 75848 lead tungstate crystals which have a short radiation length (0.89 cm) and fast response, since 80% of the light is emitted within 25 ns; however, they are combined with Avalanche photodiodes (APDs) as photodetectors given that crystals themselves have a low light yield (30γ/MeV). A schematic view of the ECAL is shown in figure 3.13.

Energy is measured when electrons and photons are absorbed by the crystals which generates an electromagnetic "shower", as seen in bottom right picture of the figure3.13; the shower is seen as a *cluster* of energy which depending on the amount of energy deposited can involve several crystals. The ECAL barrel (EB) covers the region $|\eta| < 1.479$, using crystals of depth of 23 cm and 2.2×2.2 cm^2 transverse section; the ECAL endcap (EE) covers the region $1.479 < |\eta| < 3.0$ using crystals of depth 22 cm and transverse section of 2.86×2.86 cm^2; the photodetectors used are vacuum phototriodes (VPTs). Each EE is divided in two structures called "Dees".

In front of the EE, it is installed the preshower detector (ES) which covers the region $1.653 < |\eta| < 2.6$. The ES provides a precise measurement of the position of electromagnetic showers, which allows to distinguish electrons and photons signals from π^0 decay signals. The ES is composed of a layer of lead absorber followed by a layer of plastic scintillators

3.3.5 Hadronic calorimeter

Hadrons are not absorbed by the ECAL but by the hadron calorimeter (HCAL), which is made of a combination of alternating brass absorber layers and silicon photomultiplier(SiPM) layers; therefore, particles passing through the scintillator material produce showers, as in the ECAL, as a result of the inelastic scattering of the hadrons with the detector material. Since the particles are not absorbed in the scintillator, their energy is sampled; therefore the total energy is not measured but estimated from

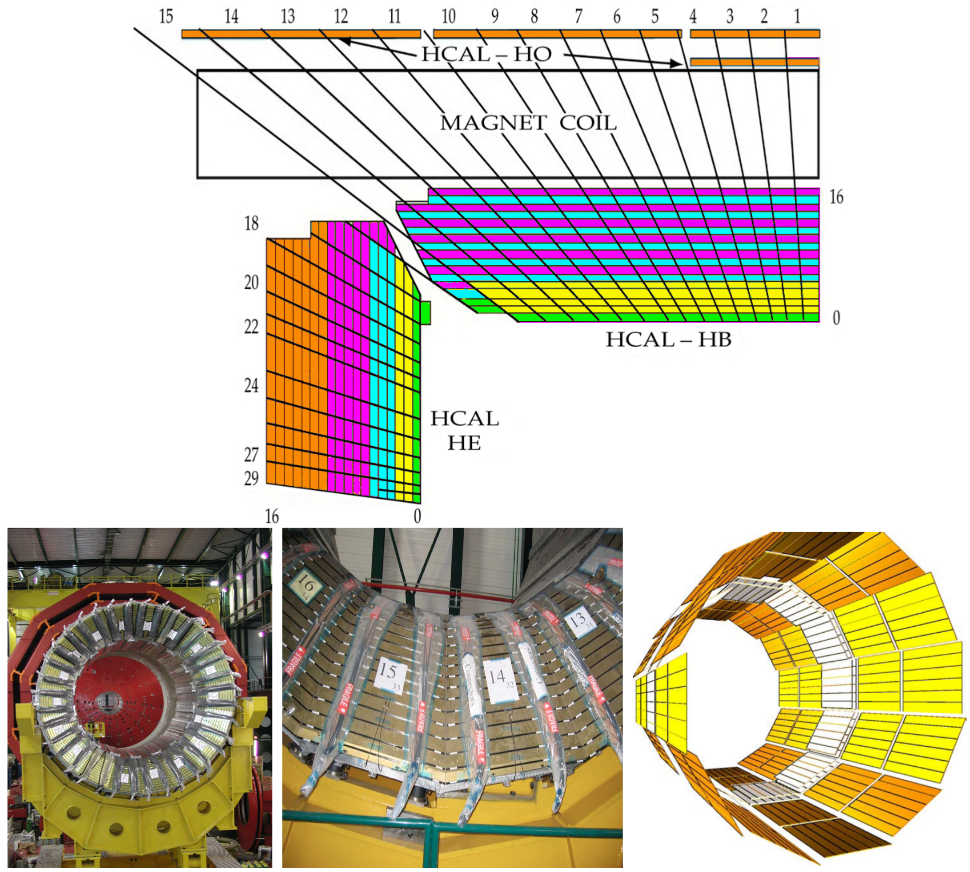

Figure 3.14: Top: CMS HCAL schematic view, the colors indicate the layers that are grouped into the same readout channels. Bottom: picture of a section of the HB; the absorber material is the golden region and scintillators are placed in between the absorber material (left and center). Schematic view of the HO (right). [74, 75]

the energy clusters, which reduce the resolution of the detector. Brass was chosen as the absorber material due to its short interaction length ($\lambda_I = 16.42$cm) and its non-magnetivity. Figure 3.14 shows a schematic view of the CMS HCAL.

The HCAL is divided into four sections; the Hadron Barrel (HB), the Hadron Outer (HO), the Hadron Endcap (HE) and the Hadron Forward (HF) sections. The HB covers the region $0 < |\eta| < 1.4$, while the HE covers the region $1.3 < |\eta| < 3.0$. The HF, made of quartz fiber scintillator and steel as absorption material, covers the forward region $3.0 < |\eta| < 5.2$. Both the HB and HF are located inside the solenoid. The HO is placed outside the magnet as an additional layer of scintillators with the purpose of measure the energy tails of particles passing through the HB and the magnet (see figure 3.14 top and bottom right). The upgrades made to the HCAL during the technical stop 2016-2017 consisted in the replacement of the photo transducer, in order to improve the efficiency.

3.3.6 Superconducting solenoid magnet

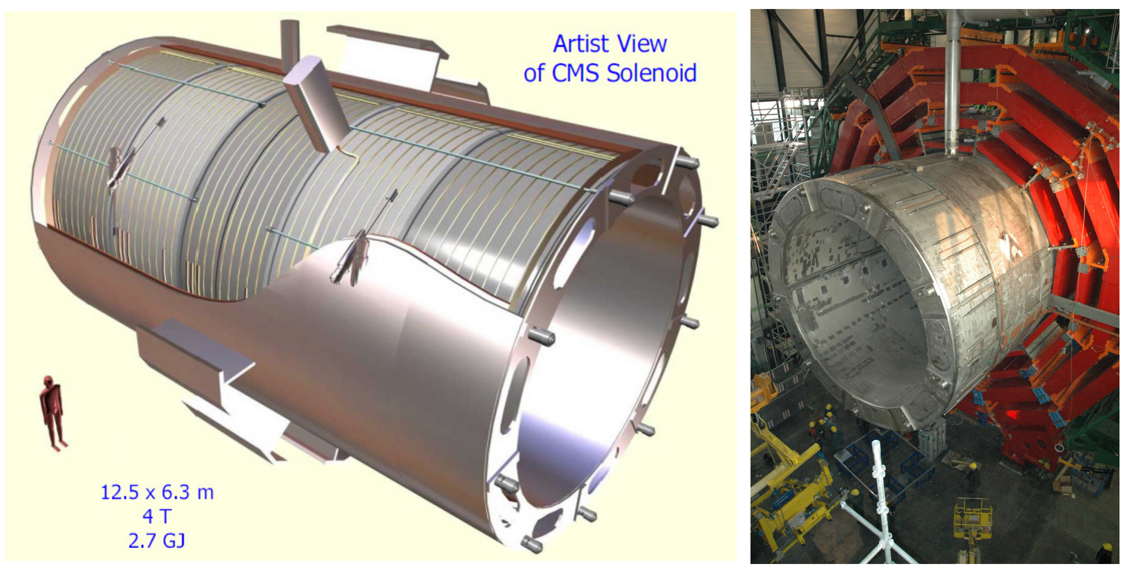

Figure 3.15: Artistic representation of the CMS solenoid magnet(left). The magnet is supported on an iron yoke (right) which also serves as the house of the muon detector and as mechanical support for the whole CMS detector [69].

The superconducting magnet installed in the CMS detector is designed to provide an intense and highly uniform magnetic field in the central part of the detector. In fact, the tracking system takes advantage of the bending power of the magnetic field to measure with precision the momentum of the particles that traverse it; the unambiguous determination of the sign for high momentum muons was a driven principle during the design of the magnet. The magnet has a diameter of 6.3 m, a length of 12.5

m and a cold mass of 220 t; the generated magnetic field reaches a strength of 3.8T. Since it is made of Ni-Tb superconducting cable it has to operate at a temperature of 4.7 K by using a helium cryogenic system; the current circulating in the cables reaches 18800 A under normal running conditions. The left side of figure 3.15 shows an artistic view of the CMS magnet, while the right side shows a transverse view of the cold mass where the winding structure is visible.

The yoke (see figure 3.15), composed of 5 barrel wheels and 6 endcap disks made of iron, serves not only as the media for magnetic flux return but also provides the house for the muon detector system and structural stability to the full detector.

3.3.7 Muon system

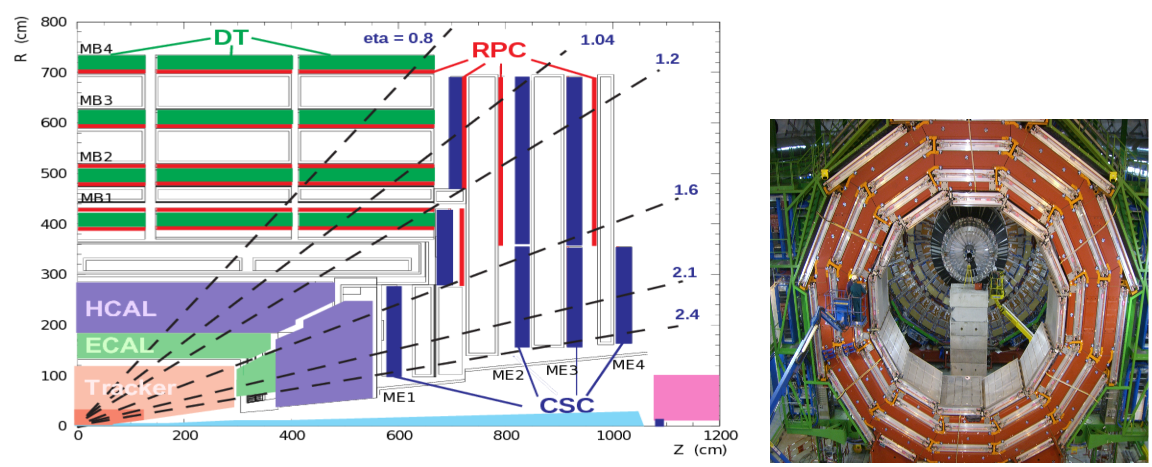

Figure 3.16: Left: CMS muon system schematic view; Right: one of the yoke rings with the muon DTs and RPCs installed; in the back it is possible to see the muon endcap [76].

Muons are the only charged particles able to pass through all the CMS detector due to their low ionization energy loss; thus, muons can be separated easily from the high amount of particles produced in a *pp* collision. Also, muons are expected to be produced in the decay of several new particles; therefore, a good detection of muons was on the leading principles when designing the CMS detector.

The CMS muon detection system (muon spectrometer) is embedded in the return yoke as seen in figure 3.16. It is composed of three different detector types, the drift tube chambers (DT), Cathode strip chambers (CSC), and resistive plate chambers (RPC); DT are located in the central region $\eta < 1.2$ arranged in four layers of drift chambers filled with an Ar/CO_2 gas mixture.

The muon endcaps are made of CSCs covering the region $\eta < 2.4$ and filled with a mixture of $Ar/CO_2/CF_4$. The reason behind using a different detector type lies on the different conditions in the forward region like the higher muon rate and higher residual magnetic field compared to the central region.

The third type of detector used in the muon system is a set of four disks of RPCs working in avalanche mode. The RPCs provide good spatial and time resolutions. The track of $high - p_T$ muon candidates is built combining information from the tracking system and the signal from up to six RPCs and four DT chambers.
The muon tracks are reconstructed from the hits in the several layers of the muon system.

3.3.8 CMS trigger system

Under normal conditions, CMS expects *pp* collisions every 25 ns, i.e., an interaction rate of 40 MHz for which it is not possible to store the recorded data in full. In order to handle this high event rate data, an online event selection, known as triggering, is performed; triggering reduce the event rate to 100 Hz for storage and further offline analysis.

The trigger system starts with a reduction of the event rate to 100 kHz in the so-called "level 1 trigger (L1)". L1 is based on dedicated programmable hardware like Field Programmable Gate Arrays (FPGAs) and Application Specific Integrated Circuits (ASICs), partly located in the detector itself; another portion is located in the CMS under-ground cavern. Hit patterns information from the muon chambers and the energy deposits in the calorimeter are used to decide if an event is accepted or rejected, according to selection requirements previously defined, which reflect the interesting physics processes. Figure 3.17 shows the L1 trigger architecture.

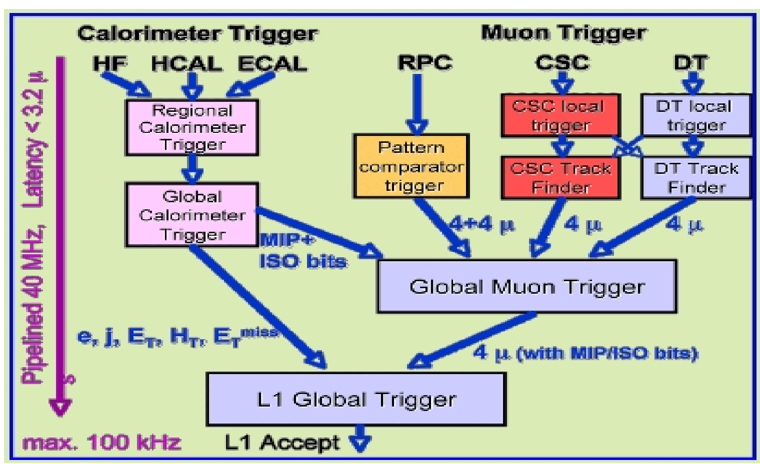

Figure 3.17: CMS Level-1 trigger architecture [77].

The second stage in the trigger system is called " high-level trigger (HLT)"; events accepted by L1 are passed to HLT in order to make an initial reconstruction of them. HLT is software based and runs on a dedicated server farm, using selection algorithms and high-level object definitions; the event rate at HLT is reduced to 100 Hz. The first HLT stage takes information from the muon detectors and the calorimeters to make the initial object reconstruction; in the next HLT stage, information from the pixel and strip detectors is used to do first fast-tracking and then full tracking online. This initial object reconstruction is used in further steps of the trigger system.

Events and preliminary reconstructed physics objects from HLT are sent to be fully reconstructed at the CERN computing center. Again, the pixel detector information provides high-quality seeds for the track reconstruction algorithm offline, primary vertex reconstruction, electron and photon identification, muon reconstruction, τ identification, and b-tagging. After full reconstruction, data sets are made available for offline analyses.

During the 2016-2017 technical stop, the L1 system was updated in order to improve the physics object identification by improving the algorithms and accounting for the increasing pile-up scenario.

3.3.9 CMS computing

After the data, coming from the experiment, are processed at several levels, they have to be stored and made available for further analysis; in order to cope all the tasks implied in the offline data processing, like transfer, simulation, reconstruction and reprocessing, among others, a big computing power is required. The CMS computing system is based on the distributed architecture concept, where users of the system and physical computer centers are distributed worldwide and interconnected by high-speed networks.

The worldwide LHC computing grid (WLCG) is the mechanism used to provide that distributed environment. WLCG is a tiered structure connecting computing centers around the world, which provides the necessary storage and computing facilities. The

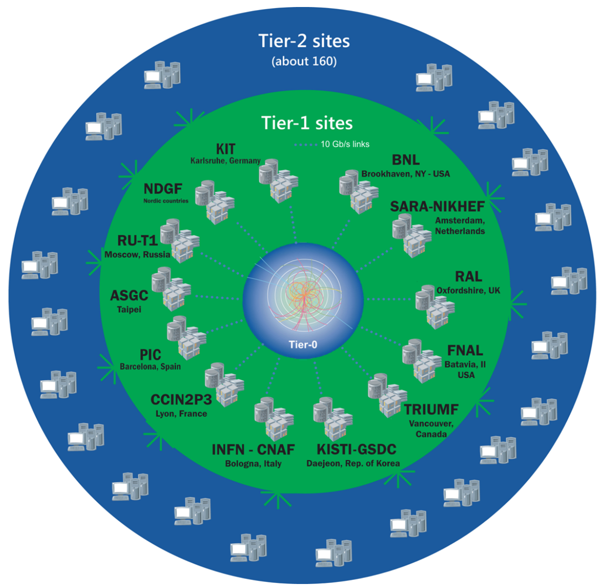

Figure 3.18: WLCG structure. The primary computer centers (Tier-0) are located at CERN (data center) and at the Wigner datacenter in Budapest. Tier-1 is composed of 13 centers and Tier-2 is composed of about 160 centers. [78].

primary computing centers of the WLCG are located at the CERN and the Wigner datacenter in Budapest and are known as Tier-0 as shown in figure 3.18. The main responsibilities for each tier level are [78]

- **Tier-0**: initial reconstruction of recorded events and storage of the resulting datasets, the distribution of raw data to the Tier-1 centers.
- **Tier-1**: provide storage capacity, support for the Grid, safe-keeping of a proportional share of raw and reconstructed data, large-scale reprocessing and safe-keeping of corresponding output, generation of simulated events, distribution of data to Tier 2s, safe-keeping of a share of simulated data produced at these Tier 2s.
- **Tier-2**: store sufficient data and provide adequate computing power for specific analysis tasks, provide analysis requirements and proportional share of simulated event production and reconstruction.

Aside from the general computing strategy to manage the huge amount of data produced by experiments, CMS uses a framework to perform a variety of processing, selection and analysis tasks. The central concept of the CMS data model referred to as “event data model” (EDM) is the “Event”; therefore, an event is the unit that contains the information from a single bunch crossing as well as any data derived from that information like the reconstructed objects, the details under which additional data are derived.

Events are passed as the input to the “physics modules” that obtain information from them and create new one; for instance, “event data producers” add new data into the events, “analyzers” produce an information summary from an event set, “filters” perform selection and triggering.

CMS uses several event formats with different levels of detail and precision

- **Raw format**: events in this format contain the full recorded information from the detector as well as trigger decision and other metadata. An extended version of raw data is used to store information from the CMS Monte Carlo simulation tools. Raw data are stored permanently, occupying about 2MB/event
- **RECO format**: events in this format correspond to raw data that have been submitted to reconstruction algorithms like primary and secondary vertex reconstruction, particle ID, track-finding. RECO events contain physical objects and all the information used to reconstruct them; average size is about 0.5 MB/event.
- **AOD format**: Analysis Object Data (AOD) is the data format used in the physics analyses given that it contains the parameters describing the high-level

physics objects in addition to enough information to allow a kinematic refitting if needed. AOD events are filtered versions of the RECO events to which skimming or other kind processes have been applied. Requires about 100 kB/event.

- **Non-event data** are data needed to interpret and reconstruct events. Some of the non-event data used by CMS contains information about the detector contraction and condition data like calibrations, alignment, and detector status.

Figure 3.19 shows the data flow scheme between CMS detector and hardware tiers.

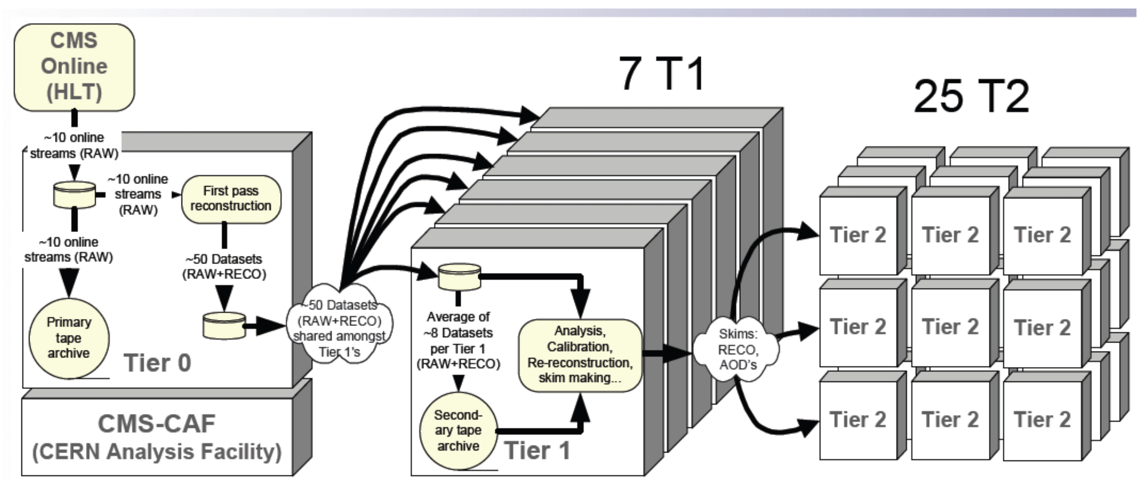

Figure 3.19: Data flow from CMS detector through hardware Tiers.

The whole collection of software built as a framework is referred to as "CMSSW". This framework provides the services needed by the simulation, calibration and alignment, and reconstruction modules that process event data, so that physicists can perform analysis. The CMSSW event processing model is composed of one executable, called cmsRun, and several plug-in modules which contains all the tools (calibration, reconstruction algorithms) needed to process an event. The same executable is used for both detector and Monte Carlo data [79].

Chapter 4

Event generation, simulation and reconstruction

The process of analyzing the data recorded by the CMS experiment involves several stages where the data are processed in order to interpret the information provided by all the detection systems; in those stages, the particles produced after the *pp* collision are identified by reconstructing their trajectories and measuring their features. In addition, the SM provides a set of predictions that have to be compared with the experimental results; however, in most of the cases, theoretical predictions are not directly comparable to experimental results due to the diverse source of uncertainties introduced by the experimental setup and theoretical approximations among others.

The strategy to face these conditions consist in using statistical methods implemented in computational algorithms to produce numerical results that can be contrasted with the experimental results. These computational algorithms are commonly known as Monte Carlo (MC) methods and, in the case of particle physics, they are designed to apply the SM rules and produce predictions about the physical observables measured in the experiments. Since particle physics is governed by quantum mechanics principles, predictions are not allowed for single events; therefore, a high number of events are "generated" and predictions are produced in the form of statistical distributions for the observables. Effects of the detector presence are included in the predictions by introducing simulations of the detector itself.

This chapter presents a description of the event generation strategy and the tools used to perform the detector simulation and physics objects reconstruction. A comprehensive review of event generators for LHC physics can be found in reference [80] on which this chapter is based.

4.1 Event generation

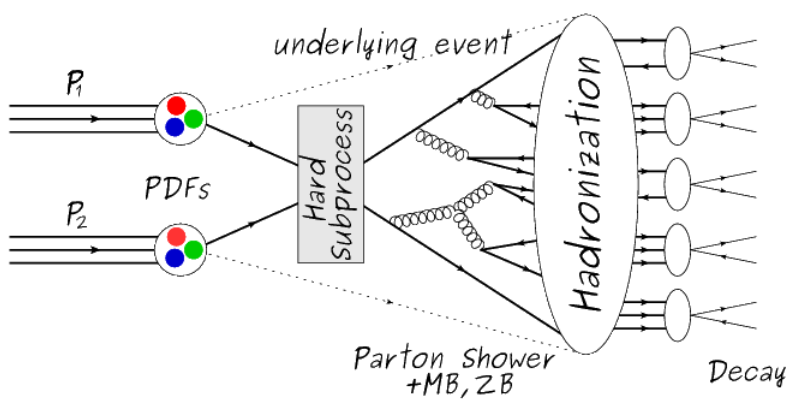

Figure 4.1: Event generation process. In the first step, the PDF of the colliding particles is considered so the specific interaction is described. The actual interaction is generated in the hard subprocess; the cross-section of the process is calculated from the matrix element connecting the initial and final states. The parton shower describes the evolution of the partons from the hard subprocess according to the DGLAP equations. At this step, the underlying event and PU effects are included in the generation. The resulting partons from the parton shower are recombined to form hadrons in the hadronization step; most of them are unstable, therefore, their decays are also generated in agreement to the known branching ratios. Modified from reference [81].

The event generation is intended to create events that mimic the behavior of actual events produced in the collisions; the obey a sequence of steps from the particles collision hard process to the decay process into the final state particles. Figure 4.1 shows a schematic view of the event generation process; the fact that the full process can be treated as several independent steps is based on the QCD factorization theorem.

Generation starts by taking into account the PDFs of the incoming particles. Event generators offer the option to chose from several PDF sets depending on the particular process under simulation[1]; in the following *pp* collisions will be considered. The *hard subprocess* describes the actual interaction between partons from the incoming protons; it is represented by the matrix element connecting the initial and final states of the interaction. Normally, the matrix element can be written as a sum over Feynman diagrams and consider interferences between terms in the summation. During the generation of the hard subprocess, the production cross section is calculated.

The order to which the cross section is calculated depends on the order of the Feynman diagrams involved in the calculation; therefore, radiative corrections are included by considering a higher order Feynman diagrams where QCD radiation dominates. Currently, cross sections calculated to LO do not offer a satisfactory description of the processes, i.e., the results are only reliable for the shape of distributions; therefore, NLO calculations have to be performed with the implication that the computing time needed is highly increased.

The final parton content of the hard subprocess is subjected to the *parton shower* which generates the gluon radiation. Parton shower evolves the partons; i.e., glouns

[1] Tool in Reference [82] allows to plot different PDF sets under customizable conditions.

split into quark-antiquark pairs and quarks of enough energy radiate gluons giving rise to further parton multiplication, following the DGLAP (Dokshitzer-Gribov-Lipatov-Altarelli-Parisi) equations. Showering continues until the energy scale is low enough to reach the non-perturbative limit.

In the simulation of LHC processes that involve b quarks like the single top quark or Higgs associated production, it is needed to consider that the b quark is heavier than the proton; in this sense, the QCD interaction description is made in two different schemes [83]

- four-flavor (4F) scheme. b quarks appear only in the final state because they are heavier than the proton and therefore they can be produced only from the splitting of a gluon into pairs or singly in association with a t quark in high energy-scale interactions. During the simulation, the b-PDFs are set to zero because it cannot be part of the proton. Calculations in this scheme are more complicated due to the presence of the second b quark but the full kinematics is considered already at LO and therefore the accuracy of the description is better.
- five-flavor (5F) scheme. b quarks are considered massless, therefore they can appear in both initial and final states since it can now be part of the proton; thus, during the simulation b-PDFs are not set to zero. In this scheme, calculations are simpler than in the 4F scheme and possible logarithmic divergences are absorbed by the PDFs through the DGLAP evolution.

In this thesis, the tHq events are generated using the 4F scheme in order to reduce uncertainties, while the tHW events are generated using the 5F scheme to eliminate LO interference with the $t\bar{t}H$ process [48].

Partons involved in the pp collision are the focus of the simulation, however, the rest of the partons inside the incoming protons are also affected because the remnants are colored objects; also, multiple parton interactions can occur. The hadronization of the remnants and multiple parton interactions are known as "underlying event" and it has to be included in the simulation. In addition, multiple pp collisions in the same bunch crossing (pile-up mentioned in 3.2) occurs, actually in two forms

- *in-time PU* which refers to multiple pp collision in the bunch crossing but that are not considered as primary vertices.
- *Out-of-time PU* which refers to overlapping pp collisions from consecutive bunch crossings; this can occurs due to the time-delays in the detection systems where information from one bunch crossing is assigned to the next or previous one.

While the underlying event effects are included in generation using generator-specific tools, PU effects are added to the generation by overlying Minimum-bias (MB) and Zero-bias (ZB) events to the generated events. MB events are inelastic events selected by using a loose (minimum bias) trigger with as little bias as possible, therefore accepting a large fraction of the overall inelastic event; ZB events correspond to random events recorded by the detector when collisions are likely. MB model in-time PU and ZB model out-of-time PU.

The next step in the generation process is called "hadronization". Since particles with a net color charge are not allowed to exits isolated, they have to recombine to form bound states. This is precisely the process by which the partons resulting from the parton shower arrange themselves as color singlets to form hadrons. At this step, the energy-scale is low and the strong coupling constant is large, therefore hadronization process is non-perturbative and the evolution of the partons is described using phenomenological models. Most of the baryons and mesons produced in the hadronization are unstable and hence they will decay in the detector.

The last step in the generation process corresponds to the decay of the unstable particles generated during hadronization; it is also simulated in the hadronization step, based on the known branching ratios.

4.2 Monte Carlo Event Generators.

The event generation described in the previous section has been implemented in several software packages for which a brief description is given.

- **PYTHIA 8**. It is a program designed to perform the generation of high energy physics events which describe the collisions between particles such as electrons, protons. Several theories and models are implemented in it, in order to describe physical aspects like hard and soft interaction, parton distributions, initial and final-state parton showers, multiple parton interactions, beam remnants, hadronization[2] and particle decay. Thanks to extensive testing, several optimized parametrizations, known as "tunings", have been defined in order to improve the description of actual collisions to a high degree of precision; for analysis at $\sqrt{s} = 13$ TeV, the underline event CUETP8M1 tune is employed [85]. The calculation of the matrix element is performed at LO which is not enough for the current required level of precision; therefore, pythia is often used for parton shower, hadronization and decays, while other event generators are used to generate the matrix element at NLO.

[2] based in the Lund string model [84]

- **MadGraph5_aMC@NLO**. MadGraph is a matrix element generator which calculates the amplitudes for all contributing Feynman diagrams of a given process but does not provide a parton shower while MC@NLO incorporate NLO QCD matrix elements consistently into a parton shower framework; thus, MadGraph5_aMC@NLO, as a merger of the two event generators MadGraph5 and aMC@NLO, is an event generator capable to calculate tree-level and NLO cross sections and perform the matching of those with the parton shower. It is one of the most frequently used matrix element generators; however, it has the particular feature of the presence of negative event weights which reduce the number of events used to reproduce the properties of the objects generated [86].

- **POWHEG**. It is an NLO matrix element generator where the hardest emission of color charged particles is generated in such a way that the negative event weights issue of MadGraph5_aMC@NLO is overcome; however, the method requires an interface with p_T-ordered parton shower or a parton shower generator where this highest emission can be vetoed in order to avoid double counting of this highest-energetic emission. PYTHIA is a commonly matched to POWHEG event generator [87].

Events resulting from the whole generation process are known as MC events.

4.3 CMS detector simulation.

After generation, MC events contain the physics of the collisions but they are not ready to be compared to the events recorded by the experiment since these recorded events correspond to the response of the detection systems to the interaction with the particles traversing them. The simulation of the CMS detector has to be applied on top of the event generation; it is simulated with a MC toolkit for the simulation of particles passing through matter called Geant4 which is also able to simulate the electronic signals that would be measured by all detectors inside CMS.

The simulation takes the generated particles contained in the MC events as input, makes them pass through the simulated geometry, and models physics processes that particles experience during their passage through matter. The full set of results from particle-matter interactions correspond to the simulated hit which contains information about the energy loss, momentum, position. Particles of the input event are called "primary", while the particles originating from GEANT4-modeled interactions of a primary particle with matter are called a "secondary". Simulated hits are the input of subsequent modules that emulate the response of the detector readout system and triggers. The output from the emulated detection systems and triggers is known as digitization [88, 89].

The modeling of the CMS detector corresponds to the accurate modeling of the interaction among particles, the detector material, and the magnetic field. This simulation procedure includes the following standard steps

- Modeling of the Interaction Region.
- Modeling of the particle passage through the hierarchy of volumes that compose CMS detector and of the accompanying physics processes.
- Modeling of the effect of multiple interactions per beam crossing and/or the effect of events overlay (Pile-Up simulation).

- Modeling of the detector's electronics response, signal shape, noise, calibration constants (digitization).

In addition to the full simulation, i.e. a detailed detector simulation, a faster simulation (FastSim) have been developed, that may be used where much larger statistics are required. In FastSim, detector material effects are parametrized and included in the hits; those hits are used as input of the same higher-level algorithms[3] used to analyze the recorded events. In this way, comparisons between fast and full simulations can be performed [91].

After the full detector simulation, the output events can be directly compared with events actually recorded in the CMS detector. The collection of MC events that reproduce the expected physics for a given process are known as MC samples.

4.4 Event reconstruction.

In contrast to MC samples for which all the particles' information is available from it's identity to its mass and energy, recorded events contain the electronic signals, provided by the CMS detection systems, encoding the interaction of physical particles with the detector matter; these electronic signals have to be combined in order to identify these particles and measure their features i.e., particles have to be "reconstructed" using the signals provided by the detection systems. The CMS experiment use the "particle-flow event reconstruction algorithm (PF)" to do the reconstruction of particles produced in *pp* collisions. Next sections will present a basic description

[3] track fitting, calorimeter clustering, b tagging, electron identification, jet reconstruction and calibration, trigger algorithms which will be considered in the next sections

of the *Elements* used by PF (tracker tracks, energy clusters, and muon tracks), based in the references [92, 93] where more detailed descriptions can be found.

4.4.1 Particle-Flow Algorithm.

Each of the several sub detection systems of the CMS detector is dedicated to identifying a specific type of particles, i.e., photons and electrons are absorbed by the ECAL and their reconstruction is based on ECAL information; hadrons are reconstructed from clusters in the HCAL while muons are reconstructed from hits in the muon chambers. PF is designed to correlate signals from all the detector layers (tracks and energy clusters) in order to reconstruct and identify each final state particle and its properties as sketched in figure 4.2.

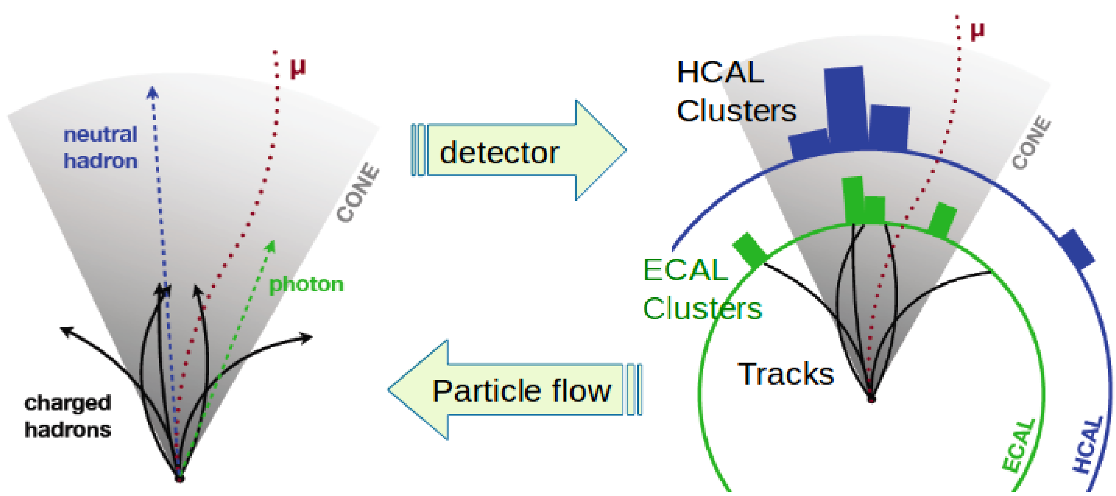

Figure 4.2: Particle flow algorithm. Information from the several CMS detection systems if provided as input to the algorithm which then combine it to identify and reconstruct all the particles in the final state and their properties. Reconstruction of simulated events is also performed by providing information from MC samples, detector and trigger simulation [94].

For instance, a charged hadron is identified by a geometrical connection, know as *link* between one or more calorimeter clusters and a track in the tracker provided there are no hits in the muon system; combining several measurements allows a better determination of the energy and charge sign of the charged hadron.

Charged-particle track reconstruction.

The strategy used by PF in order to reconstruct tracks is called "Iterative Tracking" which occurs in four steps

- Seed generation where initial track candidates are found by looking for a combination of hits in the pixel detector, strip tracker, and muon chambers. In total ten iterations are performed, each one with a different seeding requirement. Seeds are used to estimate the trajectory parameters and uncertainties at the time of the full track reconstruction. Seeds are also considered track candidates.

- Track finding using a tracking software known as Combinatorial Track Finder (CTF) [95]. The seed trajectories are extrapolated along the expected flight path of a charged particle, in agreement to the trajectory parameters obtained in the first step, in an attempt to find additional hits that can be assigned to the track candidates.

- Track-fitting where the found tracks are passed as input to a module which provides the best estimate of the parameters of each trajectory.

- Track selection where track candidates are submitted to a selection which discards those that fail a set of defined quality criteria.

Iterations differ in the seeding configuration and the final track selection as elaborated in references [92, 93]. In the first iteration, high p_T tracks and tracks produced near to the interaction region are identified and those hits are masked thereby reducing the combinatorial complexity. Next iterations search for more complicated tracks, like low p_T tracks and tracks from b hadron decays, which tend to be displaced from the interaction region.

Vertex reconstruction.

During the track reconstruction, an extrapolation toward to the calorimeters is performed in order to match energy deposits; that extrapolation is performed also toward the beamline in order to find the origin of the track known as *vertex*. The vertex reconstruction is performed by selecting from the available reconstructed tracks, those that are consistent with being originated in the interaction region where *pp* collisions are produced. The selection involves a requirement on the number of tracker (pixel and strip) hits and the goodness of the track fit.

Selected tracks are clustered using a "deterministic annealing algorithm (DA)"[4]. A set of candidate vertices and their associated tracks, resulting from the DA, are then fitted with an "adaptive vertex fitter (AVF)" to produce the best estimate of the vertices locations.

The p_T of the several tracks associated to a reconstructed vertex is added, squared and used to organize the vertices; the vertex with the highest squared sum is designated as the *primary vertex (PV)* while the rest are designated as PU vertices.

Calorimeter clustering.

After traversing the CMS tracker system, electrons, photons and hadrons deposit their energy in the ECAL and HCAL cells. The PF clustering algorithm aims to provide a high detection efficiency even for low-energy particles and an efficient distinction

[4] DA algorithm and AVF are described in detail in references [97, 98]

between close energy deposits. The clustering runs independently in the ECAL barrel and endcaps, HCAL barrel and endcaps, and the two preshower layers, following two steps

- cells with an energy larger than a given seed threshold and larger than the energy of the neighboring cells are identified as cluster seeds. The neighbor cells are those that either share a side with the cluster seed candidate, or the eight closest cells including cells that only share a corner with the seed candidate.

- cells with at least a corner in common with a cell already in the cluster seed and with an energy above a cell threshold are grouped into topological clusters.

Clusters formed in this way are known as *particle-flow clusters*. With this clustering strategy, it is possible to detect and measure the energy and direction of photons and neutral hadrons as well as differentiate these neutral particles from the charged hadron energy deposits. In cases involving charged hadrons for which the track parameters are not determined accurately, for instance, low-quality and high-p_T tracks, clustering helps in the energy measurements.

Electron track reconstruction.

Although the charged-particle track reconstruction described above works for electrons, they lose a significant fraction of their energy via bremsstrahlung photon radiation before reaching the ECAL; thus, the reconstruction performance depends on the ability to measure also the radiated energy. The reconstruction strategy, in this case, requires information from the tracking system and from the ECAL. Bremsstrahlung photons are emitted at similar η values to that of the electron but at different values of ϕ; therefore, the radiated energy can be recovered by grouping ECAL clusters in a η window over a range of ϕ around the electron direction. The group is called ECAL supercluster.

Electron candidates from the track-seeding and ECAL super clustering are merged into a single collection which is submitted to a full electron tracking fit with a Gaussian-sum filter (GSF) [96]. The electron track and its associated ECAL supercluster form a *particle-flow electron*.

Muon track reconstruction.

Given that the CMS detector is equipped with a muon spectrometer capable to identify and measure the momentum of the muons traversing it, the muon reconstruction is not specific to PF; therefore, three different muon types are defined

- *Standalone muon.* A clustering on the DTs or CSCs hits is performed to form track segments; those segments are used as seeds for the reconstruction in the muon spectrometer. All DTs, CSCs, and RPCs hits along the muon trajectory are combined and fitted to form the full track. The fitting output is called a *standalone-muon track*.
- *tracker muon.* Each track in the inner tracker with p_T larger than 0.5 GeV and a total momentum p larger than 2.5 GeV is extrapolated to the muon system. A *tracker muon track* corresponds to the extrapolated tracks that match at least one muon segment.
- *Global muon.* When tracks in the inner tracker (inner tracks) and standalone-muon tracks are matched and turn out being compatibles, their hits are combined and fitted to form a *global-muon track*.

Global muons sharing the same inner track with tracker muons are merged into a single candidate. PF muon identification uses the muon energy deposits in ECAL, HCAL, and HO associated with the muon track to improve the muon identification.

Particle identification and reconstruction.

PF elements are connected by a linker algorithm that tests the connection between any pair of elements; if they are found to be linked, a geometrical distance that quantifies the quality of the link is assigned. Two elements may be linked indirectly through common elements. Linked elements form *PF blocks* and a PF block may contain elements originating in one or more particles. Links can be established between tracks, between calorimeter clusters, and between tracks and calorimeter clusters. The identification and reconstruction start with a PF block and proceeds as follows

- Muons. An "isolated global muon" is identified by evaluating the presence of inner track and energy deposits close to the global muon track in the (η,ϕ) plane, i.e., in a particular point of the global muon track, inner tracks and energy deposits are sought within a radius of $\Delta R = 0.3$ (see eqn. 3.7) from the muon track; if they exit and the p_T of the found track added to the E_T of the found energy deposit does not exceed 10% of the muon p_T then the global muon is an isolated global muon. This isolation condition is stringent enough to reject hadrons misidentified as muons.

  "Non-isolated global muons" are identified using additional selection requirements on the number of track segments in the muon system and energy deposits along the muon track. Muons inside jets are identified with more stringent criteria in isolation and momentum as described in reference [99]. The PF elements associated with an identified muon are masked from the PF block.

- Electrons are identified and reconstructed as described above plus some additional requirements on fourteen variables like the amount of energy radiated, the distance between the extrapolated track position at the ECAL and the position of the associated ECAL supercluster among others, which are combined in a specialized multivariate analysis strategy that improves the electron identification. Tracks and clusters used to identify and reconstruct electrons are masked in the PF block.

- Isolated photons are identified from ECAL superclusters with E_T larger than 10 GeV, for which the energy deposited at a distance of 0.15, from the supercluster position on the (η,ϕ) plane, does not exceed 10% of the supercluster energy; note that this is an isolation requirement. In addition, there must not be links to tracks. Clusters involved in the identification and reconstruction are masked in the PF block.

- Bremsstrahlung photons and prompt photons tend to convert to electron-positron pairs inside the tracker, therefore, a dedicated finder algorithm is used to link tracks that seem to originate from a photon conversion; in case those two tracks are compatible with the direction of a bremsstrahlung photon, they are also linked to the original electron track. Photon conversion tracks are also masked in the PF block.

- The remaining elements in the PF block are used to identify hadrons. In the region $|\eta| \leq 2.5$, neutral hadrons are identified with HCAL clusters not linked to any track while photons from neutral pion decays are identified with ECAL clusters without links to tracks. In the region $|\eta| > 2.5$ ECAL clusters linked to HCAL clusters are identified with a charged or neutral hadron shower; ECAL clusters with no links are identified with photons. HCAL clusters not used yet, are linked to one or more unlinked tracks and to an unlinked ECAL in order to reconstruct charged-hadrons or a combination of photons and neutral hadrons according to certain conditions on the calibrated calorimetric energy.

- Charged-particle tracks may be liked together when they converge to a "secondary vertex (SV) " displaced from the interaction point where the PV and PU vertices are reconstructed; at least three tracks are needed in that case, of which at most one has to be an incoming track with hits in tracker region between a PV and the SV.

The linker algorithm, as well as the whole PF algorithm, has been validated and commissioned; results from that validation are presented in the references [92].

Jet reconstruction.

Quarks and gluons may be produced in the *pp* collisions, therefore, their hadronization will be seen in the detector as a shower of hadrons and their decay products in the form of a "jet". The anti-k_t algorithm [100] is used to perform the jet reconstruction by clustering those PF particles within a cone (see figure 4.3); previously, isolated electrons, isolated muons, and charged particles associated with other interaction vertices are excluded from the clustering.

The anti-k_t algorithm proceeds in a sequential recombination of PF particles; the distance between particles i and j (d_{ij}) and the distance between particles and the beam are defined as

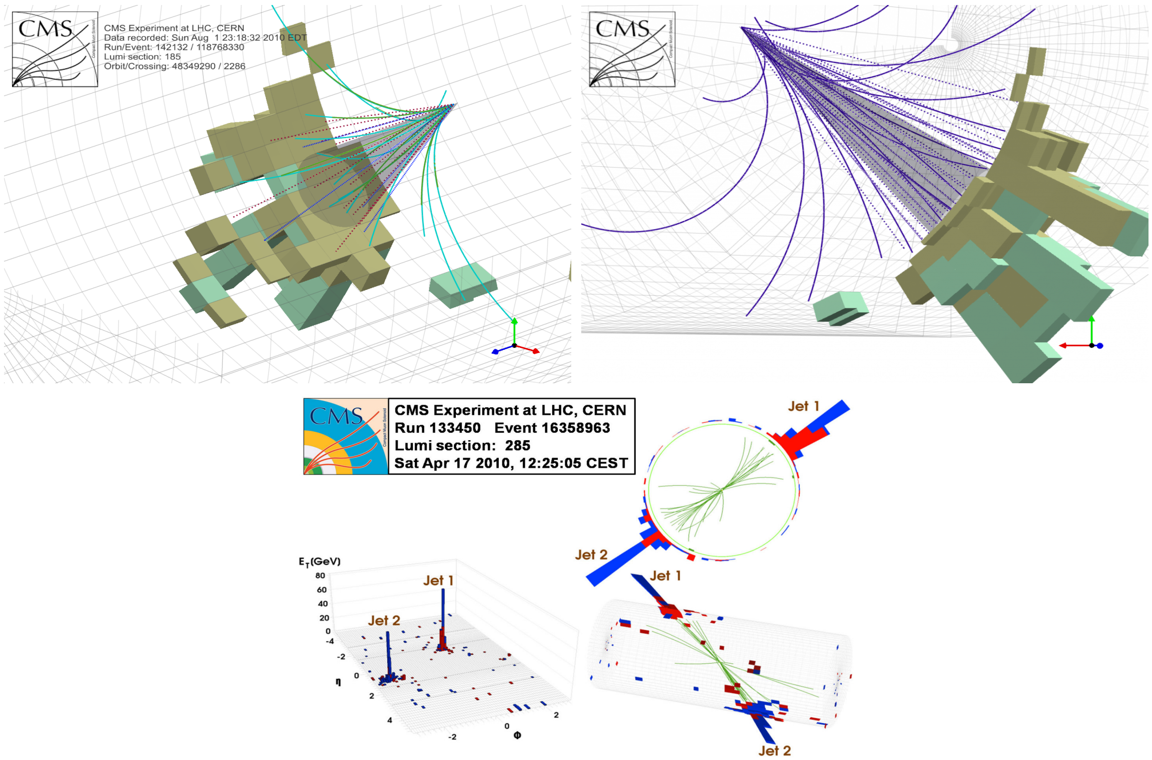

Figure 4.3: Jet reconstruction performed by the anti-k_t algorithm. Top: Two different views of a CMS recorded event are presented. Continuous lines correspond to the tracks left by charged particles in the tracker while dotted lines are the imaginary paths followed by neutral particles. The green cubes represent the ECAL cells while the blue ones represent the HCAL cells; in both cases, the height of the cube represent the amount of energy deposited in the cells [101]. Bottom: Reconstruction of a recorded event with two jets [102].

$$
\begin{aligned}
d_{ij} =& \min\left(\frac{1}{k_{ti}^2}, \frac{1}{k_{tj}^2}\right)\frac{\Delta_{ij}^2}{R^2} \\
d_{iB} =& \frac{1}{k_{ti}^2}
\end{aligned}
\tag{4.1}
$$

where $\Delta_{ij}^2 = (y_i - y_j)^2 + (\phi_i - \phi_j)^2$, k_{ti}, y_i and ϕ_i are the transverse momentum, rapidity and azimuth of particle i respectively and R is the called jet radius. For all the remaining PF particles, after removing the isolated ones, d_{ij} and d_{iB} are calculated[5] and the smallest is identified; if it is a d_{ij}, particles i and j are replaced with a new object whose momentum in the vectorial sum of the combined particles. If the smallest distance is a d_{iB} the clustering process ends, the object i (which at this stage should be a combination of several PF particles) is declared as a *Particle-flow-jet* (PF jet) and all the associated PF particles are removed from the detector. The clustering process is repeated until no PF particles remain.

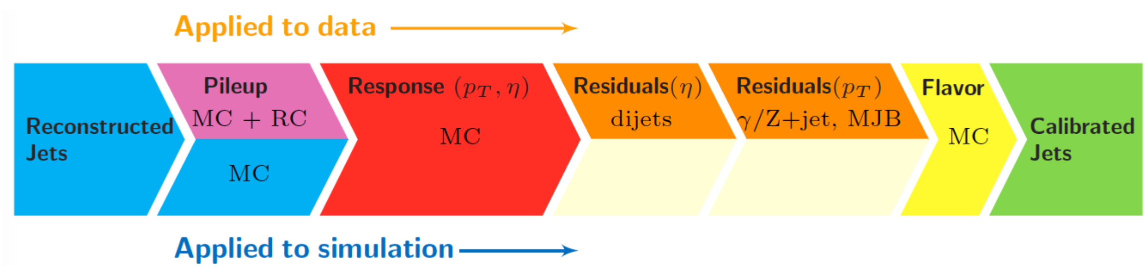

Figure 4.4: Jet energy correction diagram. Correction levels are applied sequentially in the indicated fixed order [104].

Even though jets can be reconstructed efficiently, there are some effects that are not included in the reconstruction and that lead to discrepancies between the reconstructed results and the predicted results; in order to overcome these discrepancies, a factorized model has been designed in the form of jet energy corrections (JEC) [103, 104] applied sequentially as shown in the diagram of figure4.4.

At each level, the jet four-momentum is multiplied by a scaling factor based on jet properties, i.e., η, flavor, etc.

- Level 1 correction removes the energy coming from pile-up. The scale factor is determined using a MC sample of QCD dijet events with and without pileup overlay; it is parametrized in terms of the offset energy density ρ, jet area A, jet η and jet p_T. Different corrections are applied to data and MC due to the detector simulation.

[5] Notice that this is a combinatorial calculation.

- MC-truth correction accounts for differences between the reconstructed jet energy and the MC particle-level energy. The correction is determined on a QCD dijet MC sample and is parametrized in terms of the jet p_T and η.

- Residuals correct remaining small differences within jet response in data and MC. The Residuals η-dependent correction compares jets of similar p_T in the barrel reference region. The Residuals p_T-dependent correct the jet absolute scale (JES vs p_T).

- Jet-flavor corrections are derived in the same way as MC-truth corrections but using QCD pure flavor samples.

b-tagging of jets.

A particular feature of the hadrons containing bottom quarks (b-hadrons) is that they have a lifetime long enough to travel some distance before decaying, but it is not as long as those of light quark hadrons; therefore, when looking at the hadrons produced in pp collisions, b-hadrons decay typically inside the tracker rather than reach the calorimeters as some light-hadrons do. As a result, a b-hadron decay gives rise to a displaced vertex (secondary vertex) with respect to the primary vertex as shown in figure 4.5; the SV displacement is in the order of a few millimeters. A jet resulting from the decay of a b-hadron is called b jet; other jets are called light jets.

Several methods to identify b-jets (b-tagging) have been developed; the method used in this thesis is known as "Combined Secondary Vertex" algorithm in its second version (CSVv2) [105]. By using information of the impact parameter, the reconstructed secondary vertices and the jet kinematics in a multivariate analysis that combines the discrimination power of each variable in one global discriminator variable, three

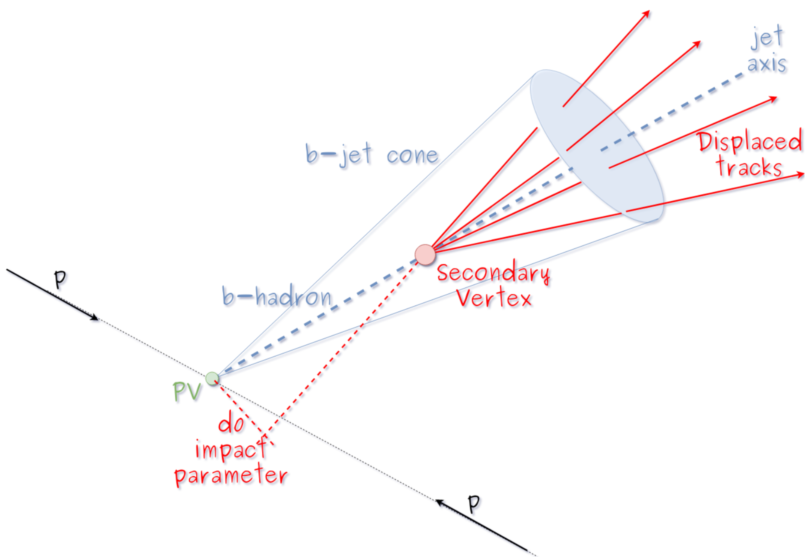

Figure 4.5: Secondary vertex in a b-hadron decay.

working points (references): loose, medium and tight, are defined which quantify the probabilities of mistag jets from light quarks as jets from b quarks; 10, 1 and 0.1 % respectively. Although the mistagging probability decrease with the working point strength, the efficiency to correctly tag b-jets also decrease as 83, 69 and 49 % for the respective working point; therefore, a balance needs to be achieved according to the specific requirements of the analysis.

4.4.1.1 Missing transverse energy.

The fact that proton bunches carry momentum along the $z$axis implies that for each event, momentum balance in the transverse plane is expected. Imbalances are quantified by the missing transverse energy (MET) and are attributed to several sources including particles escaping undetected through the beam pipe, neutrinos produced in weak interactions processes which do not interact with the detector and thus escaping without leaving a sign, or even undiscovered particles predicted by models beyond the SM.

The PF algorithm assign the negative sum of the momenta of all reconstructed PF particles to the *particle-flow MET* according to

$$\vec{\not{E}}_T = -\sum_i \vec{p}_{T,i} \tag{4.2}$$

JEC are propagated to the calculation of the $\vec{\not{E}}_T$ as described in the reference [106].

4.4.2 Event reconstruction examples

Figures 4.6-4.8 show the results of the reconstruction performed on 3 recorded events. Descriptions are taken directly from the source.

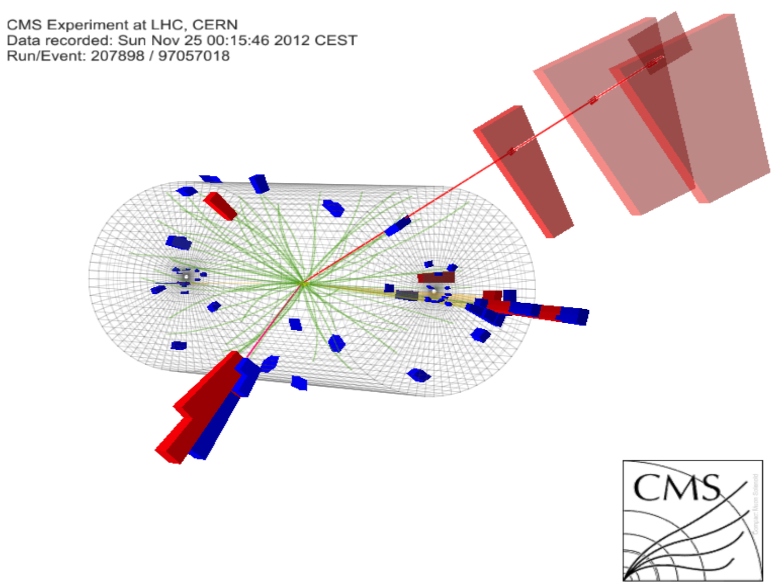

Figure 4.6: HIG-13-004 Event 1 reconstruction results; "HIG-13-004 Event 1: Event recorded with the CMS detector in 2012 at a proton-proton center-of-mass energy of 8 TeV. The event shows characteristics expected from the decay of the SM Higgs boson to a pair of τ leptons. Such an event is characterized by the production of two forward-going jets, seen here in opposite endcaps. One of the τ decays to a muon (red lines on the right) and neutrinos, while the other τ decays into a charged hadron and a neutrino." [**?**].

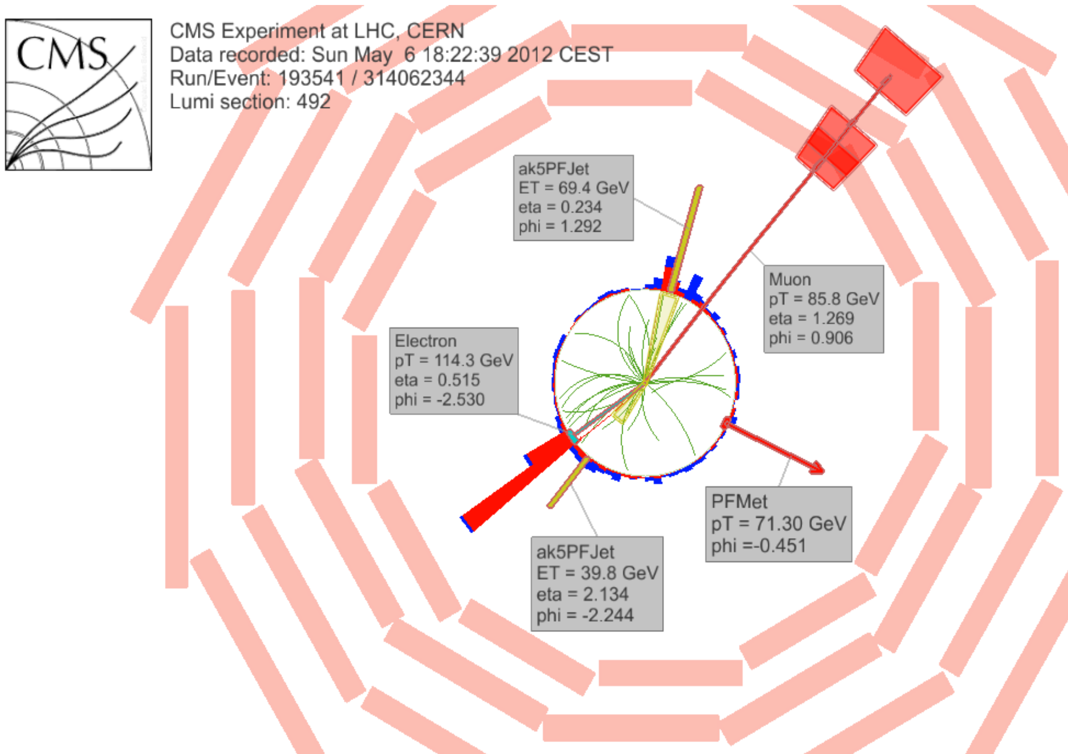

Figure 4.7: $e\mu$ event reconstruction results;"An $e\mu$ event candidate selected in 8 TeV data, as seen from the direction of the proton beams. The kinematics of the main objects used in the event selection are highlighted: two isolated leptons and two particle-flow jets. The reconstructed missing transverse energy is also displayed for reference" [**?**].

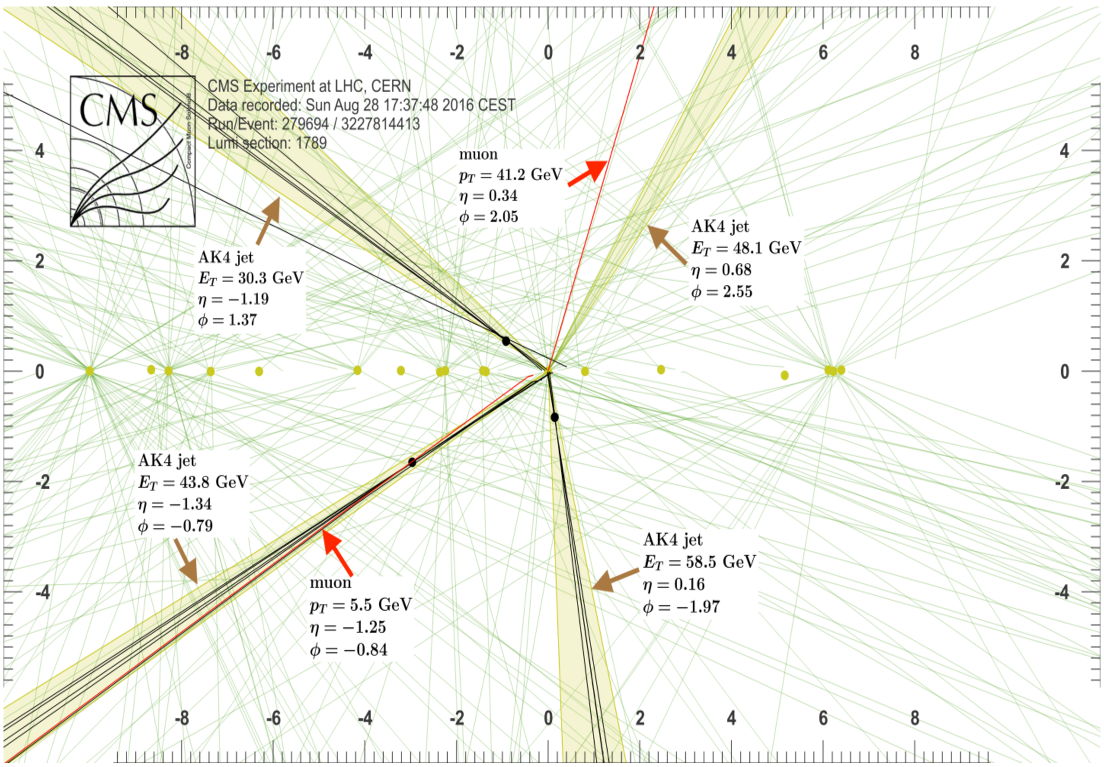

Figure 4.8: Recorded event reconstruction results;"Recorded event (ρ-z projection) with three jets with $p_T > 30$ GeV with one displaced muon track in 2016 data collected at 13 TeV. Each of the three jets has a displaced reconstructed vertex. The jet with $p_T(j) = 43.8$ GeV, $\eta(j) = -1.34$, $\phi(j) = -0.79$ contains muon with $p_T(\mu) = 5.5$ GeV, $\eta(\mu) = -1.25$, $\phi(\mu) = -0.84$. Event contains reconstructed isolated muon with $p_T(\mu) = 41.2$ GeV, $\eta(\mu) = 0.34$, $\phi(\mu) = 2.05$ and MET with $p_T = 72.5$ GeV, $\phi = -0.32$. Jet candidates for a b-jet from top quark leptonic and hadronic decays are tagged by CSVv2T algorithm. One of the other two jets is tagged by CharmT algorithm. Tracks with $p_T > 0.5$ GeV are shown. The number of reconstructed primary vertices is 18. Reconstructed m_T(W) is 101.8 GeV. Beam spot position correction is applied. Reconstructed primary vertices are shown in yellow color, while reconstructed displaced vertices and associated tracks are presented in black color. Dimensions are given in cm" [107].

Chapter 5

Statistical methods

In the course of analyzing the data sets provided by the CMS experiment and used in this thesis, several statistical tools have been employed; in this chapter, a description of these tools will be presented, starting with the general statement of the multivariate analysis method, followed by the particularities of the Boosted Decision Trees (BDT) method and its application to the classification problem. Statistical inference methods used will also be presented. This chapter is based mainly on the references [108–110].

5.1 Multivariate analysis

Multivariate data analysis (MVA) makes reference to statistical techniques that analyze data containing information of more than one variable, commonly taking into account the effects of all variables on the response of the particular variable under investigation, i.e., considering all the correlations between variables. MVA is employed in a variety of fields like consumer and market research, quality control and process optimization. From a MVA it is possible to identify the dominant patterns in the data, like groups, outliers and trends, and determine to which group a set of values belong; in the particle physics context, MVA methods are used to perform the selection of certain type of events, from a large data set, using a potentially large number of measurable properties for each event.

Processes with small cross section, as the tHq process, normally are hidden behind more common processes; therefore, the data set results in a subset of events with characteristic features of interest (signal) mixed in randomly with a much larger number of SM events that can mimic these features of interest (background) which implies that it is not possible to say with certainty that a given event is signal or background. In that sense, the problem can be formulated as one where a set of events have to be classified according to some features; these features correspond to the measurements of several parameters like energy or momentum, organized in a set of *input variables*. The measurements for each event can be written in a vector $\mathbf{x} = (x_1, ..., x_n)$ for which

- Signal hypotheses $\rightarrow f(\mathbf{x}|s)$ is the probability density (*likelihood function*) that $\mathbf{x}$ is the set of measured values given that the events is a signal event.

- Background hypotheses $\rightarrow f(\mathbf{x}|b)$ is the probability density (*likelihood function*) that $\mathbf{x}$ is the set of measured values given that the event is a background event.

Figure 5.1 shows three ways to perform a classification of events for which measurements of two properties, two input variables, have been performed; blue circles represent signal events while red triangles represent background events. The classification on (a) is *cut-based* requiring $x_1 < c_1$ and $x_2 < c_2$; usually the cut values are chosen according to some knowledge about the event process. In (b), the classification is performed by stating a cut involving a linear function of the input variables and so the boundary, while in (c) the the relationship between the input variables is not linear thus the boundary is not linear either.

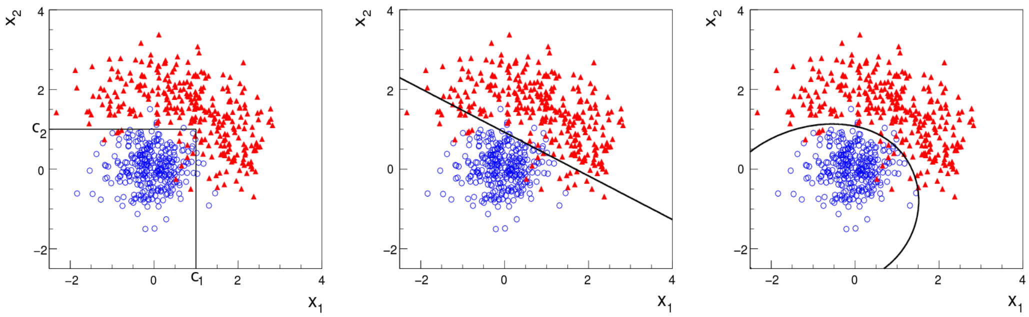

Figure 5.1: Scatter plots-MVA event classification. Distribution of two input variables x_1 and x_2 measured for a set of events; blue circles represent signal events and red triangles represent background events. The classification is based on (a) cuts, (b) linear boundary, and (c) nonlinear boundary [108]

The boundary can be parametrized in terms of the input variables such that the cut is set on the parametrization instead of on the variables, i.e., $y(\mathbf{x}) = y_{cut}$ with y_{cut} a constant; thus, the acceptance or rejection of an event is based on what side of the boundary is the event located. If $y(\mathbf{x})$ has functional form, it can be used to determine the probability distribution functions $p(y|s)$ and $p(y|b)$ and then perform a scalar test statistic with a single cut on the scalar variable y.

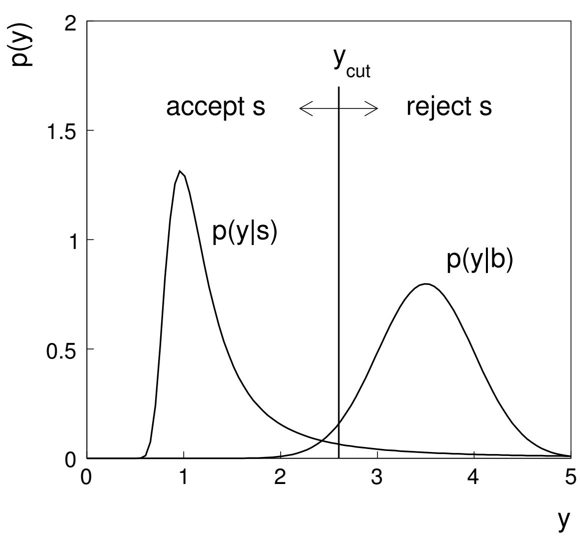

Figure 5.2: Distributions of the scalar test statistic $y(\mathbf{x})$ under the signal and background hypotheses. [108]

Figure 5.2 illustrates what would be the probability distribution functions under the signal and background hypotheses for a scalar test statistic with a cut on the classifier y. Notice that the tails of the distributions indicate that some signal events fall on the rejection region and some background events fall on the acceptance region; therefore, it is convenient to define the *efficiency* with which events of a given type are accepted, thus, the signal and background efficiencies are given by

$$\varepsilon_{\mathrm{s}} = P(\text{accept event}|\mathrm{s}) = \int_{\mathrm{A}} f(\mathbf{x}|\mathrm{s})\, d\mathbf{x} = \int_{-\infty}^{y_{\mathrm{cut}}} p(y|\mathrm{s})\, dy\ , \tag{5.1}$$

$$\varepsilon_{\mathrm{b}} = P(\text{accept event}|\mathrm{b}) = \int_{\mathrm{A}} f(\mathbf{x}|\mathrm{b})\, d\mathbf{x} = \int_{-\infty}^{y_{\mathrm{cut}}} p(y|\mathrm{b})\, dy\ , \tag{5.2}$$

where A is the acceptance region. Under these conditions, the background hypothesis corresponds to the *null hypothesis (H_0)*, the signal hypothesis corresponds to the *alternative hypothesis (H_1)*, the background efficiency is the significance level of the test, and signal efficiency is the power of the test; what is sought in an analysis is to maximize the power of the test relative to the significance level.

5.1.1 Decision trees

For this thesis, the implementation of the MVA strategy, described above, is performed through decision trees by using the TMVA software package [109] included in the the ROOT analysis framework [111]. In a simple picture, a decision tree classifies events according to their input variables values by setting a cut on each input variable and checking which events are on which side of the cut, just as proposed in the MVA strategy, but in addition, as a machine learning algorithm, decision trees offer the possibility to be trained and then perform the classification efficiently.

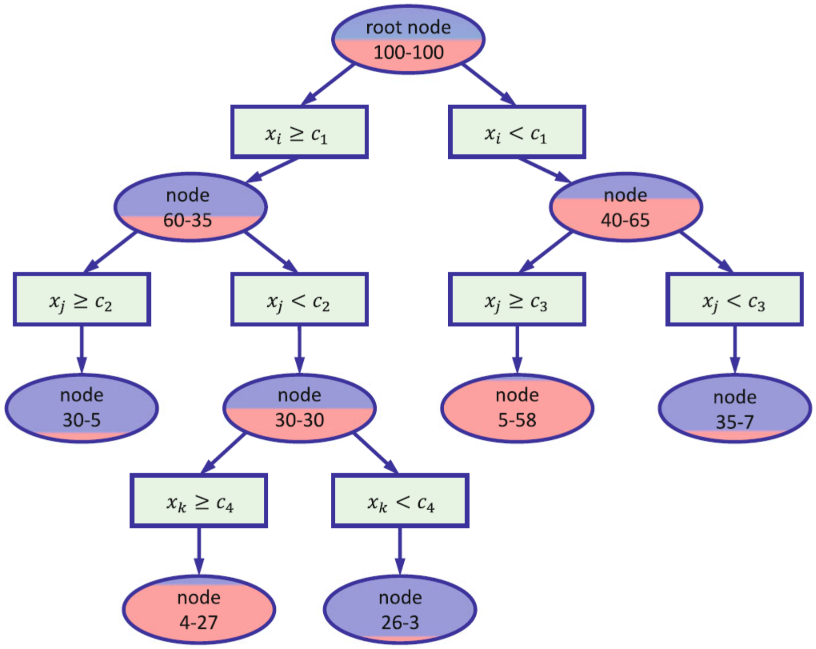

Figure 5.3: Example of a decision tree. Each node is fed with a MC sample mixing signal and background events (left-right numbers); nodes colors represent the relative amount of signal/background events [110].

The training or growing of a decision tree is the process that defines the rules for classifying events; this process is represented in figure5.3 and consist of several steps

- take MC samples of signal and background events and split them into two parts each; first parts form the training sample which will be used in the decision tree training, while the second parts form the test sample which will be used for testing the final classifier obtained from the training. Each event has associated a set of input variables $\mathbf{x} = (x_1, ..., x_n)$ which serve to distinguish between signal and background events. The training sample is taken in at the root *node*.

- pick one variable, say x_i

- pick one value of x_i, each event has its own value of x_i, and split the training sample into two subsamples B_1 and B_2; B_1 contains events for which $x_i < c_1$

while B_2 contains the rest of the training events;

- scan all possible values of x_i and find the splitting value that provides the *best* classification[1], i.e., B_1 is mostly made of signal events while B_2 is mostly made of background events.

- It is possible that variables other than the picked one produce a better classification, hence, all the variables have to be evaluated. Pick the next variable, say x_j, and repeat the scan over its possible values.

- At the end, all the variables and their values will have been scanned, the *best* variable and splitting value will have been identified, say x_1, c_1, and there will be two nodes fed with the subsamples B_1 and B_2.

Nodes are further split by repeating the decision process until: a given number of final nodes is obtained, nodes are largely dominated by either signal or background events, or nodes has too few events to continue. Final nodes are called *leaves* and they are classified as signal or background leaves according to the class of the majority of events in them. Each *branch* in the tree corresponds to a sequence of cuts.

The quality of the classification at each node is evaluated through a separation criteria; there are several of them but the *Gini Index (G)* is the one used in the decision trees trained for the analysis in this thesis. G is written in terms of the purity (P), i.e. the fraction of signal events, of the samples after the separation is made; it is given by

$$G = P(1-P) \tag{5.3}$$

[1] Quality of the classification will be treated in the next paragraph.

notice that P=0.5 at the root node while G=0 for pure leaves. For a node A split into two nodes B_1 and B_2 the G gain is

$$\Delta G = G(A) - G(B_1) - G(B_2) \tag{5.4}$$

the *best* classification corresponds to that for which the gain of G is maximized; hence, the scanning over all event's variables and their values is of capital importance.

In order to provide a numerical output for the classification, events in a signal(background) leaf are assigned an score of 1(-1) each, defining in this way the decision tree *classifier or weak learner* as

$$f(\mathbf{x}) = \begin{cases} 1 & \mathbf{x} \quad \text{in signal region,} \\ -1 & \mathbf{x} \quad \text{in background region.} \end{cases}$$

Figure 5.4shows an example of the classification of a sample of events, containing two variables, performed by a decision tree.

5.1.2 Boosted decision trees (BDT).

Event misclassification occurs when a training event ends up in the wrong leaf, i.e., a signal event ends up in a background leaf or a background event ends up in a signal leaf. A way to correct it is to assign a weight to the misclassified events and train a second tree using the reweighted events; the event reweighting is performed by a boosting algorithm, events with increased weight are known as *boosted* events, in such a way that when used in the training of a new decision tree they get correctly classified. The process is repeated iteratively adding a new tree to a forest and creating a set of classifiers which are combined to create the next classifier; the final classifier offers

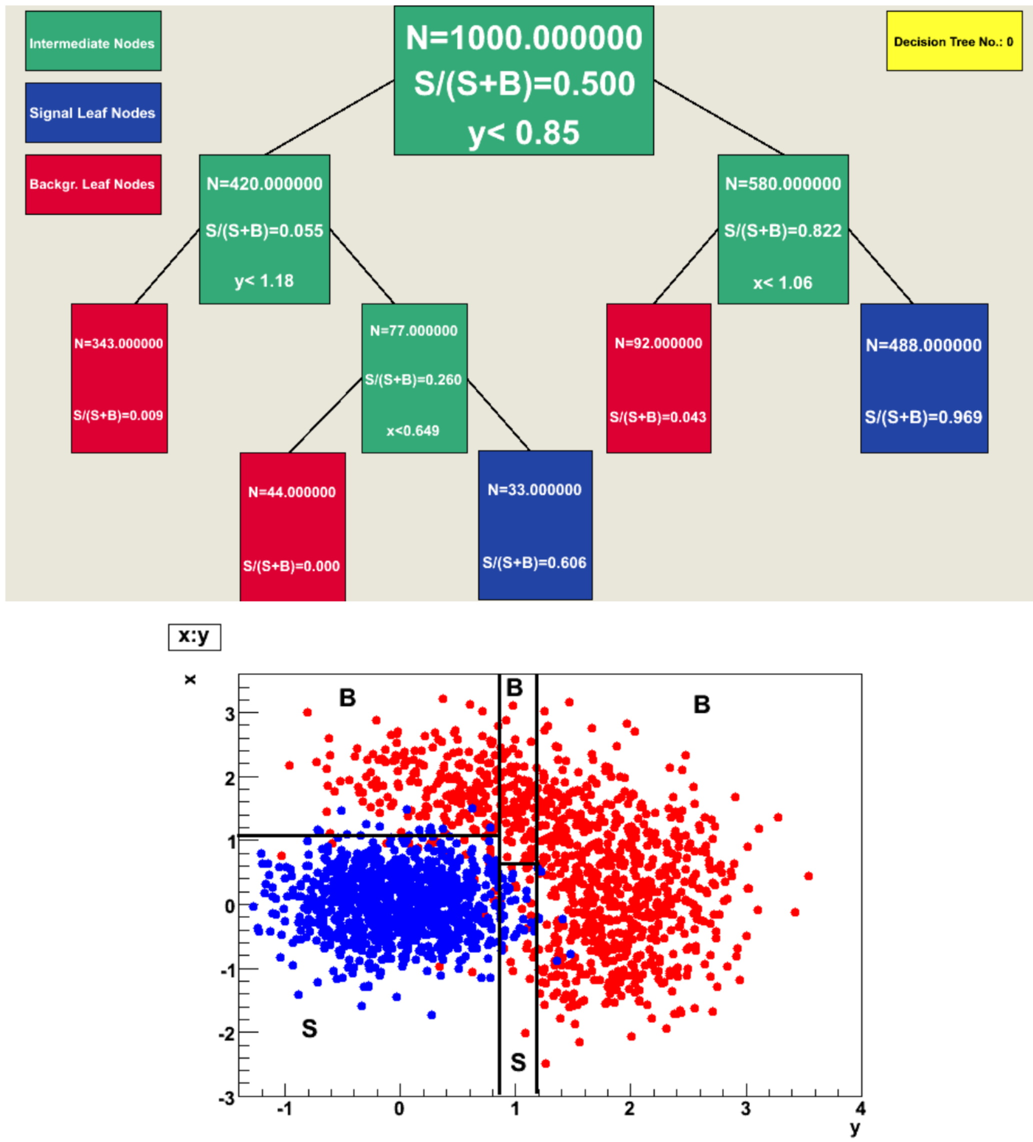

Figure 5.4: Example of a decision tree output. Each leaf, blue for signal events and red for background events, represent a region in the variables phase space [112].

more stability[2] and has a smaller misclassification rate than any individual ones. The resulting tree collection is known as a *boosted decision tree (BDT)*.

Thus, purity of the sample is generalized to

[2] Decision trees suffer from sensitivity to statistical fluctuations in the training sample which may leads to very different results with an small change in the training samples.

$$P = \frac{\sum_s w_s}{\sum_s w_s + \sum_b w_b} \tag{5.5}$$

where w_s and w_b are the weights of the events; the Gini index is also generalized

$$G = \left(\sum_i^n w_i\right) P(1-P) \tag{5.6}$$

with n the number of events in the node. The final score of an event, after passing through the forest, is calculated as the renormalized sum of all the individual (possibly weighted) scores; thus, high(low) score implies that the event is most likely signal(background).

The boosting procedure, implemented in the *Gradient boosting* algorithm used in this thesis, produce a classifier $F(\mathbf{x})$ which is the weighted sum of the individual classifiers obtained after each iteration,i.e.,

$$F(\mathbf{x}) = \sum_{m=1}^{M} \beta_m f(\mathbf{x}; a_m) \tag{5.7}$$

where M is the number of trees in the forest. The *loss function* $L(F,y)$ represent the deviation between the classifier $F(\mathbf{x})$ response and the true value y obtained from the training sample (1 for signal events and -1 for background event), according to

$$L(F,y) = \ln(1 + e^{-2F(\mathbf{x})y}) \tag{5.8}$$

thus, the reweighting is employed to ensure the minimization of the loss function; a more detailed description of the minimization procedure can be found in reference [113]. The final classifier output is later used as a final discrimination variable, labeled as *BDT output/response*.

5.1.3 Overtraining.

Decision trees offer the possibility to have as many nodes as wished in order to reduce the misclassification to zero (in theory); however, when a classifier is too much adjusted to a particular training sample, the classifier response to a slightly different sample may leads to a completely different classification results; this effect is know as *overtraining*.

An alternative to reduce the overtraining in BDTs consist in prunning the tree by removing statistically insignificant nodes after the tree growing is completed but this option is not available for BDTs with gradient boosting in the TMVA-toolkit, therefore, the overtraining has to be reduced by tuning the algorithm, number of nodes, minimum number of events in the leaves, etc. The overtraining can be evaluated by comparing the responses of the classifier when running over the training and test samples.

5.1.4 Variable ranking.

BDTs have the couple of particular advantages related to the input variables; on one side, they are relatively insensitive to the number of input variables used in the vector $\mathbf{x}$. The ranking of the BDT input variables is determined by counting the number of times a variable is used to split decision tree nodes; in addition, the separation gain-squared achieved in the splitting and the number of events in the node are accounted by applying a weighting to that number. Thus, those variables with small or no power to separate signal and background events are rarely chosen to split the nodes,i.e., are effectively ignored.

On the other side, variables correlations play an important role for some MVA methods like the Fisher discriminant algorithm in which the first step consist of performing a linear transformation to a phase space where the correlations between variables are removed; in case of BDT algorithm, correlations do not affect the performance.

5.1.5 BDT output example.

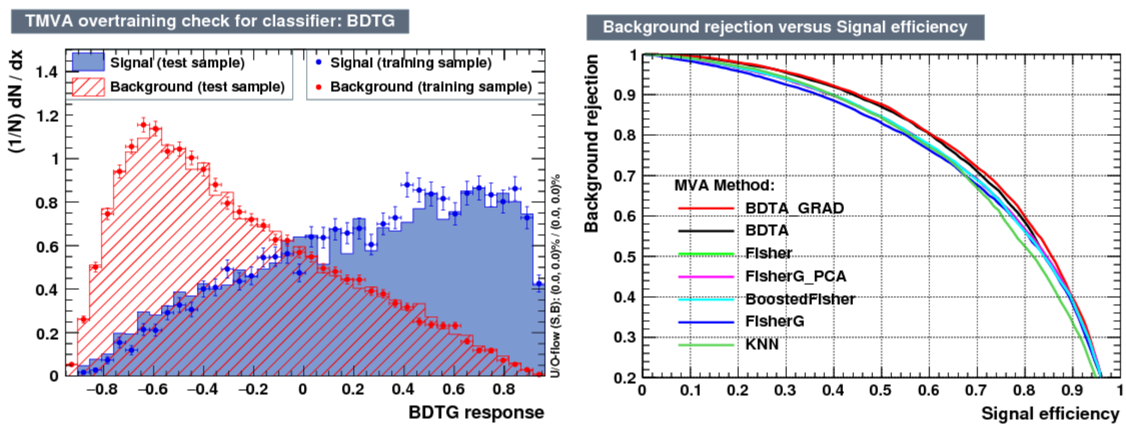

Figure 5.5: Left: Output distributions for the gradient boosted decision tree (BDTG) classifier using a sample of signal(pp *to* tHq) and background($pp \to t\bar{t}$) events. Right: Background rejection vs signal efficiency (ROC curves) for various MVA classifiers running over the same sample used to produce the plot on the left.

Left side of figure 5.5 shows the BDT output distributions for signal($pp \to tHq$) and background($pp \to t\bar{t}$) events; this plot is the equivalent to the one showed in figure 5.2. A forest with 800 trees, maximum depth per tree = 3, and gradient boosting have been used as training parameters. The BDTG classifier offers a good separation power; while there is a small overtraining in the signal distribution, the background distribution seems to be well predicted which might indicate that the sample is composed of more background than signal events.

Right side of figure 5.5 shows the background rejection vs signal efficiency curves for several combinations of MVA classifiers-boosting algorithms; these curves are known as ROC curves and give an indication of the performance of the classifier. The best performance is achieved with the BDTG classifier (BDTA_GRAD).

5.2 Statistical inference.

Once events are classified, the next step consists in finding the parameters that define the likelihood functions $f(\mathbf{x}|s), f(\mathbf{x}|b)$ for signal and background events respectively. In general, likelihood functions depend not only on the measurements but also on parameters (θ_m) that define their shapes; the process of estimating these *unknown parameters* and their uncertainties from the experimental data is called *inference.* The likelihood function for N the events the in a sample is the combination of all the likelihoods functions

$$L(\boldsymbol{\theta}) = \prod_{i=1}^{N} f(\mathbf{x}^i|\boldsymbol{\theta}) = \prod_{i=1}^{N} f(x_1^i,...,x_n^i;\theta_1,...,\theta_m) \tag{5.9}$$

Thus, the estimation of the unknown parameters from experimental data samples is written in terms of a central value using the notation

$$\theta = \hat{\theta} \pm \delta\theta \tag{5.10}$$

where the interval $[\hat{\theta}+\delta\theta, \hat{\theta}-\delta\theta]$ is called *confidence interval*; it is usually interpreted, in the limit of infinite number of experiments, as the interval where the true value of the unknown parameter θ is contained with a probability of 0.6827 (if no other convention is stated).

5.2.1 Nuisance parameters.

The unknown parameter vector $\boldsymbol{\theta}$ is made of two types of parameters: on one side, those parameters that provide information about the physical observables of interest for the experiment (*parameters of interest*); on the other side, the *nuisance parameters* that are not of direct interest for the experiment but that needs to be included in the analysis in order to achieve a satisfactory description of the data. They represent effects of the detector response like the finite resolutions of the detection systems, miscalibrations, and in general any source of uncertainty introduced in the analysis.

In some cases the nuisance parameters are estimated using dedicated data samples, for instance data from test beams for calibration purposes, when MC samples are not suitable. The nuisance parameter uncertainties produce *systematic uncertainties* while the uncertainties associated to fluctuations in data and related to the estimation of the parameters of interest produce *statistical uncertainties*.

5.2.2 Maximum likelihood estimation method

The function that produce the estimate of a parameter is called *estimator*, therefore, estimators are usually constructed using mathematical procedures encoded in algorithms. The estimation method used in this thesis is the *Maximum Likelihood Estimation* method (MLE); it is based on the combined likelihood function defined by eqn. 5.9 and the procedure seeks for the parameter set that corresponds to the maximum value of the combined likelihood function, i.e., the *maximum likelihood estimator* of the unknown parameter vector $\boldsymbol{\theta}$ is the function that produce the vector $\hat{\boldsymbol{\theta}}$ for which the likelihood function $L(\boldsymbol{\theta})$ evaluated at the measured sample $\mathbf{x}$ is maximum.

Usually, the logarithm of the likelihood function is used in the numerical algorithms implementations in order to avoid underflow the numerical precision of the computers due to the product of low likelihoods. In addition, it is usual minimize the negative logarithm of the likelihood function instead of maximizing the logarithm of it because in this way the procedure consist of differentiate a sum of therms and set the sum to zero; therefore

$$F(\boldsymbol{\theta}) = -\ln L(\boldsymbol{\theta}) = -\sum_{i=1}^{N} f(\mathbf{x}^i|\boldsymbol{\theta}). \tag{5.11}$$

The minimization process is performed by the software MINUIT [114] implemented in the ROOT analysis framework. In case of large data samples the computational resources needed to calculate the likelihood function are too big; therefore, the parameter estimation is performed using binned distributions of the variables of interest for which the *binned likelihood function* is given by

$$L(data|\mu,\theta) = \prod_{i=1} \frac{(\mu s_i(\theta) + b_i(\theta))^{n_i}}{n_i!} e^{-\mu s_i(\theta) - b_i(\theta)}, \tag{5.12}$$

with s_i and b_i the expected number of signal and background yields for bin i respectively, n_i is the observed number of events in the bin i and $\mu = \sigma/\sigma_{SM}$ is the signal strength. Notice that the number of entries per bin follows a Poisson distribution. The analysis presented in this thesis is based on the binned distribution of the ratio signal/background obtained from the BDT outputs.

5.2.3 Hypothesis test

The test statistic mentioned in section 5.1involving

; it is achieved, according to the Neyman-Pearson lemma [115],

by defining the acceptance region such that, for $\mathbf{x}$ inside the region, the likelihood ratio, i.e., the ratio of probability distribution functions for signal and background,

5.3 exclusion limits

5.4 asymptotic limits

Chapter 6

Search for production of a Higgs boson and a single top quark in multilepton final states in pp collisions at $\sqrt{s} = 13$ TeV

6.1 Introduction

The Higgs boson discovery, supported on experimental observations and theoretical predictions made about the SM, gives the clue of the way in that elementary particles acquire mass through the Higgs mechanism; therefore, knowing the Higgs mass, the Higgs-boson and Higgs-fermions couplings can be tested. In order to test the Higgs-top coupling, several measurements have been performed, as stated in the chapter 2, but they are limited to measure the square of the coupling; however, the production of a Higgs boson in association with a single top quark (tH) not only offers access to the sign of the coupling, but also, to the CP phase of the Higgs couplings.

This chapter presents the search for the associated production of a Higgs boson and a single top quark events, focusing on leptonic signatures provided by the Higgs decay modes to WW, ZZ, and $\tau\tau$; the 13 TeV dataset produced in 2016, which corresponds to an integrated luminosity of $35.9 fb^{-1}$, is used. Constraints on the sign of the Higgs- top coupling (y_t) have been derived from the decay rate of Higgs bosons to photon pairs [40] and from the cross section for associated production of Higgs and Z bosons via gluon fusion [116], with recent results disfavoring negative signs of the coupling [51, 53, 117]. It expands previous analyses performed at 8 TeV [118, 119] and searches for associated production of $t\bar{t}$ pair and a Higgs boson in the multilepton final state channel [120]; it also complements searches in other decay channels targeting $H \to b\bar{b}$ [121].

As shown in section 2.4, the SM cross section of the associated production of a Higgs boson and a single top quark (tHq) process is driven by a destructive interference between two contributions (see Figure 2.13), where the Higgs couples to either the W boson or the top quark; however, if the sign of the Higgs-top coupling is flipped with respect to the SM prediction, a large enhancement of the cross section occurs, making this analysis sensitive to such deviation. A second process, where the Higgs boson and top quark are accompanied by a W boson (tHW) has similar behavior, albeit with a weaker interference pattern and lower contribution to the tHcross section, therefore, a combination of both processes would increase the sensitivity; in this analysis both contributions are combined and referred as tHchannel. A third contribution comes from $t\bar{t}H$ process. The purpose of this analysis is to investigate the exclusion of the presence of the tH+ $t\bar{t}H$ processes under the assumption of the anomalous Higgs-top coupling modifier (κ_t=-1). The analysis exploits signatures with three leptons in the final state.

The first sections present the characteristic tHq signature as well as the expected backgrounds. The MC samples, data sets, and the physics object definitions are then defined. Following, the background predictions, the signal extraction, and the statistical treatment of the selected events as well as the systematic uncertainties are described. The final section present the results for the exclusion limits as a function of the ratio of κ_t and the dimensionless modifier of the Higgs-vector boson κ_V.

6.2 tHq signature

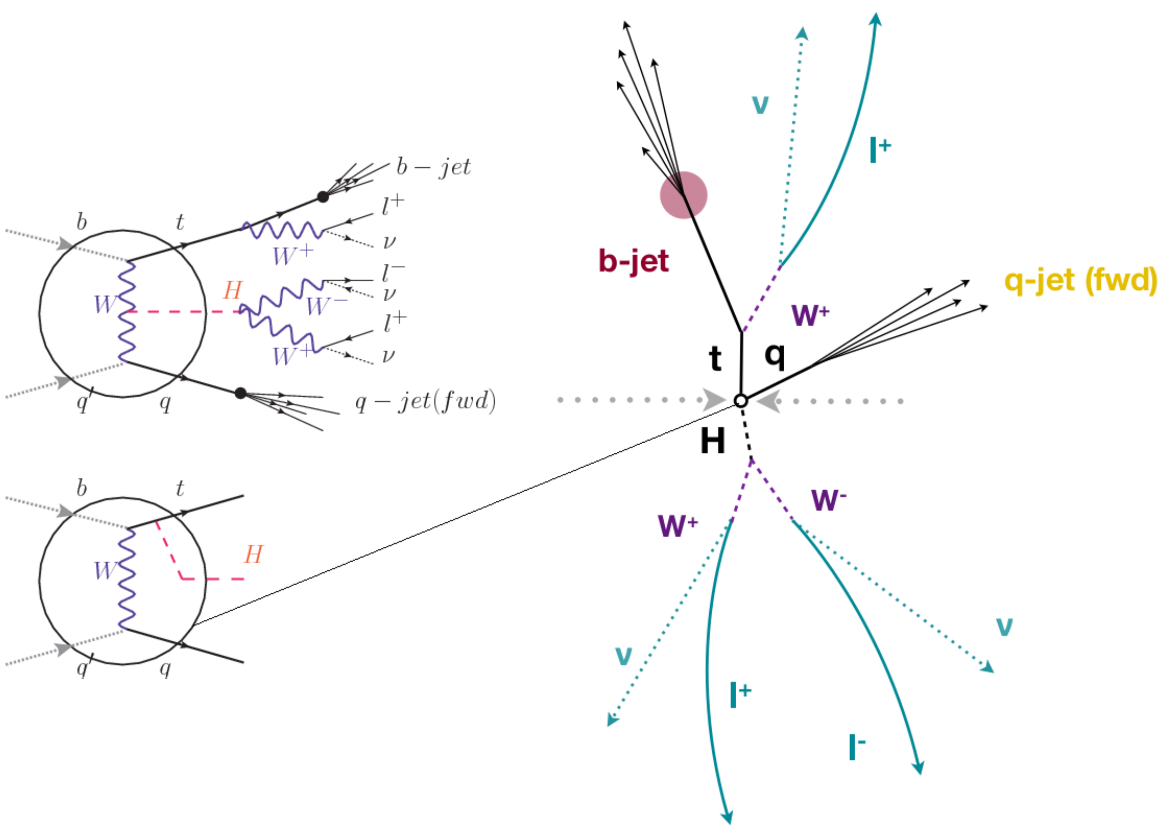

Figure 6.1: tHq event signature. Letf: Feynman diagram including the whole evolution up to the final state for the case of the Higgs boson emitted by the W boson (top); feynman diagram for the case where the Higgs boson is emitted by the top quark. Right: Schematic view as it would be seen in the detector; The circle in the feynman diagrams on the left corresponds to the circle in the center of the schematic view as indicated by the line connecting them.

In order to select events of tHq process, its features are translated into a set of selection rules; figure 6.1 shows the Feynman diagram and an schematic view of the tHq process from the pp collision to the final state configuration. A single top quark is produced accompanied by a light quark, denoted as q; this light quark is produced predominantly in the forward region of the detector. The Higgs boson which can be either emitted by the exchanged W boson or directly by the singly produced top quark.

The top quark and Higgs boson decay after their production in the detector due to their high masses/low lifetimes. The Higgs boson is required to decay into a W boson pair[1]. The top quark almost always decays into a bottom quark and a W boson, as encoded in the CMK matrix. The W bosons are required to decay leptonically while τ leptons are not reconstructed separately and only their leptonic decays into either electrons or muons are considered in this analysis.

In summary, the signal process is characterized by a the final state with one light-flavored forward jet, one central b-jet, three leptons (muons, electrons or a combination of them), three neutrinos and no central light-flavored jets. The presence of neutrinos is inferred from the presence of MET. The analysis has been made public by CMS as a Physics Analysis Summary [122] combining the result for the three lepton and two lepton same-sign channels. Currently, an effort to turn the analysis into a paper is ongoing.

6.3 Background processes

The background processes are those that can mimic the signal signature or at least can be reconstructed as that as a result of certain circumstances. The backgrounds

[1] ZZ and $\tau\tau$ decays are also include in the analysis but they are not separately reconstructed

can be classified as

- Irreducible backgrounds where genuine prompt leptons are produced in on-shell W and Z boson decays; they can be reliantly estimated directly from MC simulated events, using higher-order cross sections or data control regions for the overall normalization.

- Reducible backgrounds where at least one of the leptons is *non-prompt*, i.e., produced within a hadronic jet, either a genuine lepton from heavy flavor decays. Mis-reconstructed jets, also known as *mis-ID leptons* or *fake leptons*, are considered non-prompt leptons as well. These non-prompt leptons leave tracks and hits in the detection systems as would a prompt lepton, but correlating those hits with nearby jets could be a way of removing them. Reducible backgrounds are not well predicted by simulation, and are estimated using data-driven methods.

The main sources of background events in the case of tHq process are $t\bar{t}$ process and $t\bar{t} + X(X = W, Z, \gamma)$ processes, here represented together as $t\bar{t}$Vprocess. Figure 6.2 shows the signature for $t\bar{t}$ and $t\bar{t}W$processes;

The largest contribution to irreducible backgrounds involving prompt leptons comes from $t\bar{t}W$, $t\bar{t}Z$, processes for which the number of ($b-$)jets (($b-$)jet multiplicity) is higher than that of the signal events, while for other contributing background events, WZ, ZZ, and rare SM processes like $W^{\pm}W^{\pm}qq$, $t\bar{t}t\bar{t}$, tZq, tZW, WWW, WWZ, WZZ, ZZZ, the ($b-$)jet multiplicity is lower compared to that of the signal events. None of the irreducible backgrounds present activity in the forward region of the detector.

On the side of the reducible backgrounds, the largest contribution comes from the $t\bar{t}$ events which have a very similar signature to the signal events but does no present

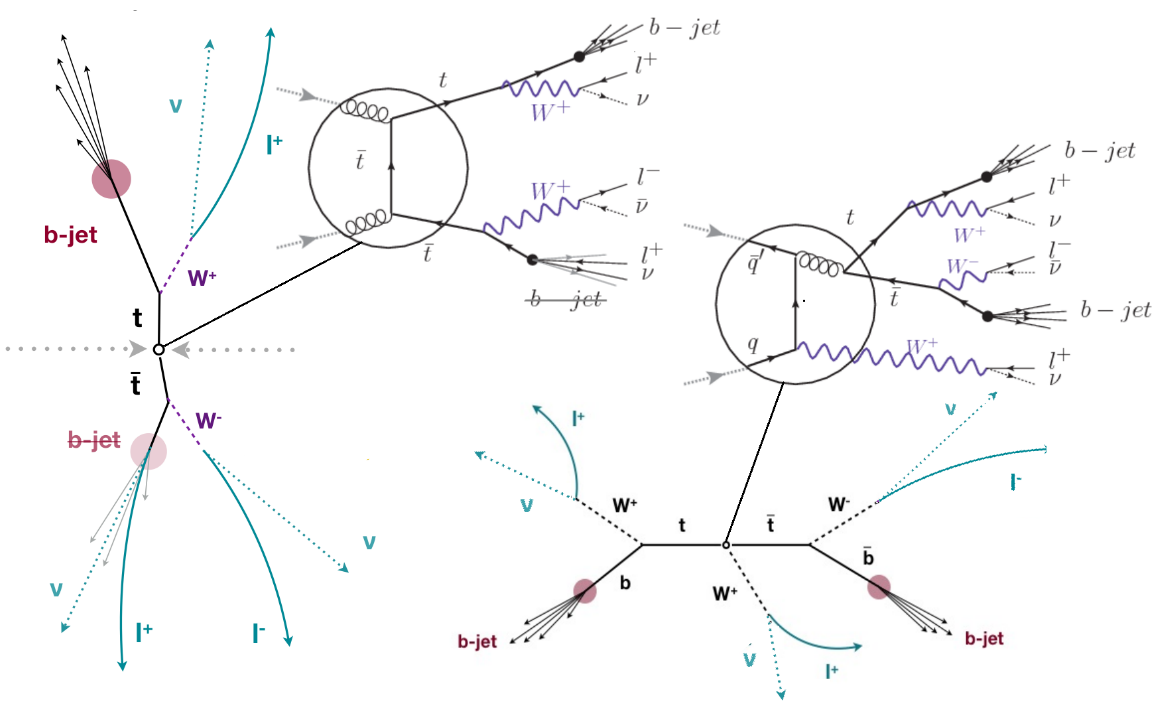

Figure 6.2: $t\bar{t}$ (left) and $t\bar{t}W$ (right) events signature as they would be seen in the detector; the feynman diagrams including the whole evolution up to the final state are also showed. The $t\bar{t}$ process signature is very similar to that of the signal process with one fake lepton and non forward activity. The $t\bar{t}W$ process present a higher b-jet multiplicity compared to the signal process, a prompt lepton and no forward activity.

activity in the forward region of the detector either; A particular feature of the $t\bar{t}$ events is their charge-symmetry which is also a difference with the signal events.

6.4 Object Identification and event selection

In this section, the specific definitions of the physical objects in terms of the numerical values assigned to the reconstruction parameters are presented; thus, the provided details summarize and complement the descriptions presented in previous chapters.

6.4.1 Jets and b tagging.

In this analysis, jets are reconstructed by clustering PF candidates using the anti-k_t algorithm with parameter distance $\Delta R = 0.4$; those charged hadrons that are not consistent with the selected primary vertex are discarded from the clustering. The jet energy is then corrected for the varying response of the detector as a function of transverse momentum p_T and pseudorapidity η. Jets are selected for use in the analysis only if they have $p_T > 25$ GeV and are separated from any selected leptons by $\Delta R > 0.4$.

Jets coming from the primary vertex and jets coming from pile-up vertices are distinguished using a MVA discriminator based on the differences in the jet shapes, in the relative multiplicity of charged and neutral components, and in the different fraction of transverse momentum which is carried by the hardest components. Jet tracks are also required to be compatible with the primary vertex.

Jets originated from the hadronization of a b quark are selected using a MVA likelihood discriminant which uses track-based lifetime information and reconstructed secondary vertices (CSV algorithm). Only jets within the CMS tracker acceptance ($\eta < 2.4$) are identified with this tool. Data samples are used to measure the efficiency of the b tagging and the probability to misidentify jets from light quarks or gluons; in both cases the measurements are parametrized as a function of the jet p_T and η and later used to correct differences between the data and MC simulation in the b tagging performance, by applying per-jet weights to the simulation, dependent on the jet p_T, η, b tagging discriminator, and flavor (from simulation truth) [123]. The per-event weight is taken as the product of the per-jet weights, including those of the jets associated to the leptons. The weights are derived on $t\bar{t}$ and Z+jets events.

Two working points are defined, based on the CSV algorithm output: *loose'* working point (CSV>0.46) with a b signal tagging efficiency of about 83% and a mistagging rate of about 8%; and *medium* working point (CSV>0.80) with $b-$tagging efficiency of about 69% and mistagging rate of order 1% [124]. Tagging of jets from charm quarks have efficiencies of about 40% and 18% for loose and medium working points respectively. Separate scale factors are applied to jets originating from bottom/charm quarks and from light quarks in simulated events to match the tagging efficiencies measured in the data.

6.4.2 Missing Energy MET.

As stated in section 4.4.1.1, the MET vector is calculated as the negative of the vector sum of transverse momenta of all PF candidates in the event and its magnitude is referred to as E_T^{miss}. Due to pile-up interactions, the performance in determining MET is degraded; in order to correct for that, the energy from the selected jets and leptons that compose the event is assigned to the variable H_T^{miss}. It is calculated in the same way as E_T^{miss} and although it has worse resolution than E_T^{miss}, it is more robust in the sense that it does not rely on the soft part of the event. The event selection uses a linear discriminator based on the two variables given by [125]

$$E_T^{miss} LD = 0.00397 * E_T^{miss} + 0.00265 * H_T^{miss} \tag{6.1}$$

taking advantage of the fact that the correlation between E_T^{miss} and H_T^{miss} is less for events with instrumental missing energy than for events with real missing energy. The working point $E_T^{miss} LD > 0.2$ was chosen to ensure a good signal efficiency while keeping a good background rejection.

6.4.3 Lepton identification

Two types of leptons are defined in this analysis: *signal leptons* are those coming from W, Z and τ decays which usually are isolated from other particle; *background leptons* are defined as leptons produced in b hadron decays, light-jets misidentification, and photon conversions. The reconstruction and identification of electron and muon candidates was described in chapter4, therefore, the advanced identification criteria used in order to retain the highest possible efficiency for signal leptons while rejecting background leptons will be described in this section.

Muon candidates are reconstructed by combining information from the silicon tracker and the outer muon spectrometer of CMS in a global fit [25]. The quality of the spatial matching be- tween the individual measurements in the tracker and the muon system is used to discriminate genuine prompt muons from hadrons punching through the calorimeters and from muons pro- duced by in-flight decays of kaons and pions. In the analysis, muon candidates are considered if they have p T > 5 GeV and | Îů | < 2.4. In the same-sign dilepton event categories, the relative uncertainty in the muon p T from the fit is required to be better than 20charge measurement. Electrons are reconstructed using information from the tracker and from the electromagnetic calorimeter [26]. Genuine electrons are identified by a multivariate algorithm using the shape

of the calorimetric shower and the quality of the reconstructed track. Furthermore, to reject electrons produced in photon conversions, candidates with missing hits in the innermost track- ing layers or matched to a conversion secondary vertex are discarded. Electrons are selected for the analysis if they have p T > 7 GeV and | Îů | < 2.5. To suppress electrons with a mis- assigned electric charge in the same-sign dilepton categories, candidates are required to have consistent charge measurements from three independent observables based on the calorimeter energy deposits and the track curvature.

Electrons and muons passing the criteria described above are referred to as âĂIJloose leptonsâĂİ in the following. A further discrimination between prompt signal leptons (i.e. from W and Z bo- son decays and from leptonic ÏĎ decays) and non-prompt and spurious leptons from b hadron decays, decays-in-flight, and photon conversions is crucial in light of the overwhelming back- ground from tt production. The small probabilities of having the second type of leptons results in a sizable number of back- ground events since the rate of tt production is much larger than the signal. To maximally exploit the available information in each event to that end, a multivariate discriminator based on a boosted decision tree (BDT) algorithm is built, taking as input not just observables related directly to the reconstructed leptons themselves, but also to the clustered energy deposits and charged particles in a cone around the lepton direction. The jet reconstruc- tion and b-tagging algorithms are run on these, and their output is used to train the algorithm. In particular, the ratio between the lepton p T and the reconstructed jet p T , and the transverse momentum of the lepton with respect to the jet axis provide good separation power in addition to more traditional observables like the relative isolation of the lepton (calculated in a variable cone size depending on the lepton p T [27, 28]), and the impact parameters of the lepton trajec- tory. The BDT algorithm is trained on prompt leptons in simulated ttH signal and non-prompt leptons in tt background events and validated using data in various control regions. Leptons are then selected for the final analysis if they pass a given threshold of the BDT output, and are referred to as âĂIJtight leptonsâĂİ in the following.

The lepton reconstruction and selection is identical to that used in the $t\bar{t}H$ multilepton analysis, as documented in Refs. [120,125]. For details on the reconstruction

Cut	Loose	Fakeable object	Tight
$\lvert\eta\rvert < 2.4$	✓	✓	✓
p_T	$> 5GeV$	$> 15GeV$	$> 15GeV$
$\lvert d_{xy}\rvert < 0.05$ (cm)	✓	✓	✓
$\lvert d_z\rvert < 0.1$ (cm)	✓	✓	✓
$\mathrm{SIP}_{3D} < 8$	✓	✓	✓
$I_{\mathrm{mini}} < 0.4$	✓	✓	✓
is Loose Muon	✓	✓	✓
jet CSV	–	< 0.8484	< 0.8484
is Medium Muon	–	–	✓
tight-charge	–	–	✓
lepMVA > 0.90	–	–	✓

Table 6.1: Requirements on each of the three muon selections. In the cases where the cut values change between the selections, those values are listed in the table. Otherwise, whether the cut is applied is indicated. For the two p_T^{ratio} and CSV rows, the cuts marked with a † are applied to leptons that fail the lepton MVA cut, while the loose cut value is applied to those that pass the lepton MVA cut.

algorithms, isolation, pileup mitigation, and a description of the lepton MVA discriminator and validation plots thereof, we refer to that document since they are out of the scope of this thesis. Three different selections are defined both for the electron and muon object identification: the *Loose*, *Fakeable Object*, and *Tight* selection. As described in more detail later, these are used for event level vetoes, the fake rate estimation application region, and the final signal selection, respectively. The p_T of fakeable objects is defined as $0.85 \times p_T(\mathrm{jet})$, where the jet is the one associated to the lepton object. This mitigates the dependence of the fake rate on the momentum of the fakeable object and thereby improves the precision of the method.

Tables 6.1 and 6.2 list the full criteria for the different selections of muons and electrons.

In addition, jets are required to be separated from any lepton candidates passing the fakeable object selections (see Tables 6.1 and 6.2) by $\Delta\mathrm{R} > 0.4$.

Cut	Loose	Fakeable Object	Tight
$\|\eta\| < 2.5$	✓	✓	✓
p_T	$> 7GeV$	$> 15GeV$	$> 15GeV$
$\|d_{xy}\| < 0.05$ (cm)	✓	✓	✓
$\|d_z\| < 0.1$ (cm)	✓	✓	✓
$\mathrm{SIP}_{3D} < 8$	✓	✓	✓
$I_{\mathrm{mini}} < 0.4$	✓	✓	✓
MVA ID $> (0.0, 0.0, 0.7)$	✓	✓	✓
$\sigma_{i\eta i\eta} < (0.011, 0.011, 0.030)$	–	✓	✓
H/E $< (0.10, 0.10, 0.07)$	–	✓	✓
$\Delta\eta_{in} < (0.01, 0.01, 0.008)$	–	✓	✓
$\Delta\phi_{in} < (0.04, 0.04, 0.07)$	–	✓	✓
$-0.05 < 1/E - 1/p < (0.010, 0.010, 0.005)$	–	✓	✓
p_T^{ratio}	–	$> 0.5\dagger$ / –	–
jet CSV	–	$< 0.3\dagger$ / < 0.8484	< 0.8484
tight-charge	–	–	✓
conversion rejection	–	–	✓
Number of missing hits	< 2	$== 0$	$== 0$
lepMVA > 0.90	–	–	✓

Table 6.2: Criteria for each of the three electron selections. In cases where the cut values change between selections, those values are listed in the table. Otherwise, whether the cut is applied is indicated. In some cases, the cut values change for different η ranges. These ranges are $0 < |\eta| < 0.8$, $0.8 < |\eta| < 1.479$, and $1.479 < |\eta| < 2.5$ and the respective cut values are given in the form (value$_1$, value$_2$, value$_3$).

6.4.4 Lepton selection efficiency

Efficiencies of reconstruction and selecting loose leptons are measured both for muons and electrons using a tag and probe method on both data and MC, using $Z \to \ell^+\ell^-$. Corresponding scale factors are derived from the ratio of efficiencies and applied to the selected These. Events are produced for the leptonic SUSY analyses using equivalent lepton selections and recycled for the $t\bar{t}H$ analysis as well as for this analysis. The efficiencies of applying the tight selection as defined in Tables 6.1 and 6.2, on the loose leptons are determined again by using a tag and probe method on a sample of DY-enriched events. They are documented for the $t\bar{t}H$ analysis in Ref. [125] and are exactly equivalent for this analysis.

.

.

.

.

.

.

.

.

.

. . .

The analysis is designed to efficiently identify and select prompt leptons from on-shell W and

Z boson decays and to reject non-prompt leptons from b quark decays and spurious lepton

signatures from hadronic jets. Events are then selected in the various lepton channels, and are

required to contain hadronic jets, some of which must be consistent with b quark hadronization. Finally, the signal yield is extracted by simultaneously fitting the output of two dedicated

multivariate discriminants (trained to separate the tHq signal from the two dominant backgrounds) in all categories

. Multivariate techniques are used to discriminate the signal from the dominant backgrounds. The analysis yields a 95% confidence level (C.L.) upper limit on the combined tH + ttH production cross section times branching ratio of 0.64 pb, with an expected limit of 0.32 pb, for a scenario with kt = âĹŠ1.0 and kV = 1.0. Values of kt outside the range of âĹŠ1.25 to +1.60 are excluded at 95% C.L., assuming kV

= 1.0.

Dont forget to mention previous constrains to ct check reference **??** and references https://link.springer.com/content/pdf/10.1007%2FJHEP01%282013%29088.pdf (paragraph after eq 2)

We selects events with three leptons and a b tagged jet in the final state. The tHq signal contribution is then determined in a fit of the observed data to two multivariate classifier outputs, each trained to discriminate against one of the two dominant backgrounds of events with non-prompt leptons from $t\bar{t}$ and of associated production of $t\bar{t}$ and vector bosons ($t\bar{t}W$, $t\bar{t}Z$). The fit result is then used to set an upper limit on the combined $t\bar{t}H$, tHq and tHWproduction cross section, as a function of the relative coupling strengths of Higgs and top quark and Higgs and W boson, respectively.

6.5 Data and MC Samples

The data considered in this analysis were collected by the CMS experiment during 2016 and correspond to a total integrated luminosity of $35.9 fb^{-1}$. Only periods when the CMS magnet was on were considered when selecting the data samples, that corresponds to the 23 Sep 2016 (Run B to G) and PromptReco (Run H) versions of the datasets. The MC samples used in this analysis correspond to the RunIISummer16MiniAODv2 campaign produced with CMSSW 80X. The two signal samples (for tHq and tHW) were produced with MG5_aMC@NLO (version 5.222), in leading-order order mode, and are normalized to next-to-leading-order cross sections, see Tab. 6.3.Each sample is generated with a set of event weights corresponding to different values of κ_t and κ_{V} couplings as shown in Tab. 6.4.

Sample	σ [pb]	BF
/THQ_Hincl_13TeV-madgraph-pythia8_TuneCUETP8M1/	0.7927	0.324
/THW_Hincl_13TeV-madgraph-pythia8_TuneCUETP8M1/	0.1472	1.0

Table 6.3: Signal samples and their cross section and branching fraction used in this analysis. See Ref. [126] for more details.

6.5.1 Full 2016 dataset and MC samples

Different MC generators were used to generate the background processes. The dominant sources ($t\bar{t}$, $t\bar{t}W$, $t\bar{t}Z$, $t\bar{t}H$) were produced using aMC@NLO interfaced to PYTHIA8, and are scaled to NLO cross sections. Other processes are simulated using POWHEG interfaced to PYTHIA, or bare PYTHIA (see table 6.5 and [120] for more details).

6.5.2 Triggers

We consider online-reconstructed events triggered by one, two, or three leptons. Single-lepton triggers are included to boost the acceptance of events where the p_T of the sub-leading lepton falls below the threshold of the double-lepton triggers. Additionally, by including double-lepton triggers in the ≥ 3 lepton category, as well as single-lepton triggers in all categories, we increase the efficiency, considering the logical "or" of the trigger decisions of all the individual triggers in a given category. Tab. 6.7 shows the lowest-threshold non-prescaled triggers present in the High-Level Trigger (HLT) menus for both Monte-Carlo and data in 2016.

6.5.2.1 Trigger efficiency scale factors

The efficiency of events to pass the trigger is measured in simulation (trivially using generator information) and in the data (using event collected by an uncorrelated MET trigger). Small differences between the data and MC efficiencies are corrected

		tHq		tHW		
κ_V	κ_t	sum of weights	cross section [pb]	sum of weights	cross section [pb]	LHE weights
1.0	-3.0	35.700022	2.991	11.030445	0.6409	LHEweight_wgt[446]
1.0	-2.0	20.124298	1.706	5.967205	0.3458	LHEweight_wgt[447]
1.0	-1.5	14.043198	1.205	4.029093	0.2353	LHEweight_wgt[448]
1.0	-1.25	11.429338	0.9869	3.208415	0.1876	LHEweight_wgt[449]
1.0	-1.0		0.7927		0.1472	
1.0	-0.75	7.054998	0.6212	1.863811	0.1102	LHEweight_wgt[450]
1.0	-0.5	5.294518	0.4723	1.339886	0.07979	LHEweight_wgt[451]
1.0	-0.25	3.818499	0.3505	0.914880	0.05518	LHEweight_wgt[452]
1.0	0.0	2.627360	0.2482	0.588902	0.03881	LHEweight_wgt[453]
1.0	0.25	1.719841	0.1694	0.361621	0.02226	LHEweight_wgt[454]
1.0	0.5	1.097202	0.1133	0.233368	0.01444	LHEweight_wgt[455]
1.0	0.75	0.759024	0.08059	0.204034	0.01222	LHEweight_wgt[456]
1.0	1.0	0.705305	0.07096	0.273617	0.01561	LHEweight_wgt[457]
1.0	1.25	0.936047	0.0839	0.442119	0.02481	LHEweight_wgt[458]
1.0	1.5	1.451249	0.1199	0.709538	0.03935	LHEweight_wgt[459]
1.0	2.0	3.335034	0.2602	1.541132	0.08605	LHEweight_wgt[460]
1.0	3.0	10.516125	0.8210	4.391335	0.2465	LHEweight_wgt[461]
1.5	-3.0	45.281492	3.845	13.426212	0.7825	LHEweight_wgt[462]
1.5	-2.0	27.606715	2.371	7.809713	0.4574	LHEweight_wgt[463]
1.5	-1.5	20.476088	1.784	5.594971	0.3290	LHEweight_wgt[464]
1.5	-1.25	17.337465	1.518	4.635978	0.2749	LHEweight_wgt[465]
1.5	-1.0	14.483302	1.287	3.775902	0.2244	LHEweight_wgt[466]
1.5	-0.75	11.913599	1.067	3.014744	0.1799	LHEweight_wgt[467]
1.5	-0.5	9.628357	0.874	2.352505	0.1410	LHEweight_wgt[468]
1.5	-0.25	7.627574	0.702	1.789184	0.1081	LHEweight_wgt[469]
1.5	0.0	5.911882	0.5577	1.324946	0.08056	LHEweight_wgt[470]
1.5	0.25	4.479390	0.4365	0.959295	0.05893	LHEweight_wgt[471]
1.5	0.5	3.331988	0.3343	0.692727	0.04277	LHEweight_wgt[472]
1.5	0.75	2.469046	0.2558	0.525078	0.03263	LHEweight_wgt[473]
1.5	1.0	1.890565	0.2003	0.456347	0.02768	LHEweight_wgt[474]
1.5	1.25	1.596544	0.1689	0.486534	0.02864	LHEweight_wgt[475]
1.5	1.5	1.586983	0.1594	0.615638	0.03509	LHEweight_wgt[476]
1.5	2.0	2.421241	0.2105	1.170602	0.06515	LHEweight_wgt[477]
1.5	3.0	7.503280	0.5889	3.467546	0.1930	LHEweight_wgt[478]
0.5	-3.0	27.432685	2.260	8.929074	0.5136	LHEweight_wgt[479]
0.5	-2.0	13.956013	1.160	4.419093	0.2547	LHEweight_wgt[480]
0.5	-1.5	8.924438	0.7478	2.757611	0.1591	LHEweight_wgt[481]
0.5	-1.25	6.835341	0.5726	2.075247	0.1204	LHEweight_wgt[482]
0.5	-1.0	5.030704	0.4273	1.491801	0.08696	LHEweight_wgt[483]
0.5	-0.75	3.510528	0.2999	1.007273	0.05885	LHEweight_wgt[484]
0.5	-0.5	2.274811	0.1982	0.621663	0.03658	LHEweight_wgt[485]
0.5	-0.25	1.323555	0.1189	0.334972	0.01996	LHEweight_wgt[486]
0.5	0.0	0.656969	0.06223	0.147253	0.008986	LHEweight_wgt[487]
0.5	0.25	0.274423	0.02830	0.058342	0.003608	LHEweight_wgt[488]
0.5	0.5	0.176548	0.01778	0.068404	0.003902	LHEweight_wgt[489]
0.5	0.75	0.363132	0.03008	0.177385	0.009854	LHEweight_wgt[490]
0.5	1.0	0.834177	0.06550	0.385283	0.02145	LHEweight_wgt[491]
0.5	1.25	1.589682	0.1241	0.692099	0.03848	LHEweight_wgt[492]
0.5	1.5	2.629647	0.2047	1.097834	0.06136	LHEweight_wgt[493]
0.5	2.0	5.562958	0.4358	2.206057	0.1246	LHEweight_wgt[494]
0.5	3.0	14.843102	1.177	5.609519	0.3172	LHEweight_wgt[495]

Table 6.4: κ_V and κ_t combinations generated for the two signal samples and their NLO cross sections. The tHq cross section is multiplied by the branching fraction of the enforced leptonic decay of the top quark (0.324). See also Ref. [126].

Sample	σ [pb]
TTWJetsToLNu_TuneCUETP8M1_13TeV-amcatnloFXFX-madspin-pythia8	0.2043
TTZToLLNuNu_M-10_TuneCUETP8M1_13TeV-amcatnlo-pythia8	0.2529
ttHJetToNonbb_M125_13TeV_amcatnloFXFX_madspin_pythia8_mWCutfix	0.2151
/store/cmst3/group/susy/gpetrucc/13TeV/u/TTLL_m1to10_LO_NoMS_for76X/	0.0283
WGToLNuG_TuneCUETP8M1_13TeV-madgraphMLM-pythia8	585.8
ZGTo2LG_TuneCUETP8M1_13TeV-amcatnloFXFX-pythia8	131.3
TGJets_TuneCUETP8M1_13TeV_amcatnlo_madspin_pythia8	2.967
TGJets_TuneCUETP8M1_13TeV_amcatnlo_madspin_pythia8	2.967
TTGJets_TuneCUETP8M1_13TeV-amcatnloFXFX-madspin-pythia8	3.697
WpWpJJ_EWK-QCD_TuneCUETP8M1_13TeV-madgraph-pythia8	0.03711
ZZZ_TuneCUETP8M1_13TeV-amcatnlo-pythia8	0.01398
WWZ_TuneCUETP8M1_13TeV-amcatnlo-pythia8	0.1651
WZZ_TuneCUETP8M1_13TeV-amcatnlo-pythia8	0.05565
WW_DoubleScattering_13TeV-pythia8	1.64
tZq_ll_4f_13TeV-amcatnlo-pythia8_TuneCUETP8M1	0.0758
ST_tWll_5f_LO_13TeV-MadGraph-pythia8	0.01123
TTTT_TuneCUETP8M1_13TeV-amcatnlo-pythia8	0.009103
WZTo3LNu_TuneCUETP8M1_13TeV-powheg-pythia8	4.4296
ZZTo4L_13TeV_powheg_pythia8	1.256
TTJets_SingleLeptFromTbar_TuneCUETP8M1_13TeV-madgraphMLM-pythia8	182.1754
TTJets_SingleLeptFromT_TuneCUETP8M1_13TeV-madgraphMLM-pythia8	182.1754
TTJets_DiLept_TuneCUETP8M1_13TeV-madgraphMLM-pythia8	87.3
DYJetsToLL_M-10to50_TuneCUETP8M1_13TeV-amcatnloFXFX-pythia8	18610
DYJetsToLL_M-50_TuneCUETP8M1_13TeV-madgraphMLM-pythia8	6024
WJetsToLNu_TuneCUETP8M1_13TeV-amcatnloFXFX-pythia8	61526.7
ST_tW_top_5f_inclusiveDecays_13TeV-powheg-pythia8_TuneCUETP8M1	35.6
ST_tW_antitop_5f_inclusiveDecays_13TeV-powheg-pythia8_TuneCUETP8M1	35.6
ST_t-channel_4f_leptonDecays_13TeV-amcatnlo-pythia8_TuneCUETP8M1	70.3144
ST_t-channel_antitop_4f_leptonDecays_13TeV-powheg-pythia8_TuneCUETP8M1	26.2278
ST_s-channel_4f_leptonDecays_13TeV-amcatnlo-pythia8_TuneCUETP8M1	3.68064
WWTo2L2Nu_13TeV-powheg	10.481

Table 6.5: List of background samples used in this analysis (CMSSW 80X). In the first section of the table are listed the samples of the processes for which we use the simulation to extract the final yields and shapes, in the second section the samples of the processes we will estimate from data. The MC simulation is used to design the data driven methods and derive the associated systematics.

Sample	σ [pb]
ttWJets_13TeV_madgraphMLM	0.6105
ttZJets_13TeV_madgraphMLM	0.5297/0.692

Table 6.6: Leading-order $t\bar{t}W$ and $t\bar{t}Z$ samples used in the signal BDT training.

Three lepton and Four lepton
HLT_DiMu9_Ele9_CaloIdL_TrackIdL_v*
HLT_Mu8_DiEle12_CaloIdL_TrackIdL_v*
HLT_TripleMu_12_10_5_v*
HLT_Ele16_Ele12_Ele8_CaloIdL_TrackIdL_v*
HLT_Mu23_TrkIsoVVL_Ele8_CaloIdL_TrackIdL_IsoVL_v*
HLT_Mu23_TrkIsoVVL_Ele8_CaloIdL_TrackIdL_IsoVL_DZ_v*
HLT_Mu8_TrkIsoVVL_Ele23_CaloIdL_TrackIdL_IsoVL_v*
HLT_Mu8_TrkIsoVVL_Ele23_CaloIdL_TrackIdL_IsoVL_DZ_v*
HLT_Ele23_Ele12_CaloIdL_TrackIdL_IsoVL_DZ_v*
HLT_Mu17_TrkIsoVVL_Mu8_TrkIsoVVL_DZ_v*
HLT_Mu17_TrkIsoVVL_TkMu8_TrkIsoVVL_DZ_v*
HLT_IsoMu22_v*
HLT_IsoTkMu22_v*
HLT_IsoMu22_eta2p1_v*
HLT_IsoTkMu22_eta2p1_v*
HLT_IsoMu24_v*
HLT_IsoTkMu24_v*
HLT_Ele27_WPTight_Gsf_v*
HLT_Ele25_eta2p1_WPTight_Gsf_v*
HLT_Ele27_eta2p1_WPLoose_Gsf_v*

Table 6.7: Table of high-level triggers that we consider in the analysis.

Category	Scale Factor
ee	1.01 ± 0.02
eμ	1.01 ± 0.01
$\mu\mu$	1.00 ± 0.01
3l	1.00 ± 0.03

Table 6.8: Trigger efficiency scale factors and associated uncertainties, shown here rounded to the nearest percent.

by applying scale factors as shown in Tab. 6.8. The exact procedure and control plots are documented in [125] for the current analysis.

6.6 Background predictions

The modeling of reducible and irreducible backgrounds in this analysis uses the exact methods, analysis code, and ROOT trees used for the $t\bar{t}H$ multilepton analysis. We give a brief description of the methods and refer to the documentation of that analysis in Refs. [120, 125] for any details.

The backgrounds in three-lepton final states can be split in two broad categories: irreducible backgrounds with genuine prompt leptons (i.e. from on-shell W and Z boson decays); and reducible backgrounds where at least one of the leptons is "non-prompt", i.e. produced within a hadronic jet, either a genuine lepton from heavy flavor decays, or simply mis-reconstructed jets.

Irreducible backgrounds can be reliantly estimated directly from Monte-Carlo simulated events, using higher-order cross sections or data control regions for the overall normalization. This is done in this analysis for all backgrounds involving prompt leptons: $t\bar{t}W$, $t\bar{t}Z$, $t\bar{t}H$, WZ, ZZ, $W^{\pm}W^{\pm}qq$, $t\bar{t}t\bar{t}$, tZq, tZW, WWW, WWZ, WZZ, ZZZ.

Reducible backgrounds, on the other hand, are not well predicted by simulation, and are estimated using data-driven methods. In the case of non-prompt leptons, a fake rate method is used, where the contribution to the final selection is estimated by extrapolating from a sideband (or "application region") with a looser lepton definition (the fakeable object definitions in Tabs. 6.1 and 6.2) to the signal selection. The tight-to-loose ratios (or "fake rates") are measured in several background dominated data events with dedicated triggers, subtracting the residual prompt lepton contribution using MC. Non-prompt leptons in our signal regions are predominantly produced in $t\bar{t}$ events, with a much smaller contribution, from Drell–Yan production. The systematic uncertainty on the normalization of the non-prompt background estimation is on the order of 50%, and thereby one of the dominant limitations on the performance of multilepton analyses in general and this analysis in particular. It consists of several individual sources, such as the result of closure tests of the method using simulated events, limited statistics in the data control regions due to necessary prescaling of lepton triggers, and the uncertainty in the subtraction of residual prompt leptons from the control region.

The fake background where the leptons pass the looser selection are weighted according to how many of them fail the tight criteria. Events with a single failing lepton are weighted with the factor $f/(1-f)$ for the estimate to the tight selection region, where f is the fake rate. Events with two failing leptons are given the negative weight $-f_i f_j/(1-f_i)(1-f_j)$, and for three leptons the weight is positive and equal to the product of $f/(1-f)$ factor evaluated for each failing lepton.

Figures 6.3 show the distributions of some relevant kinematic variables, normalized to the cross section of the respective processes and to the integrated luminosity.

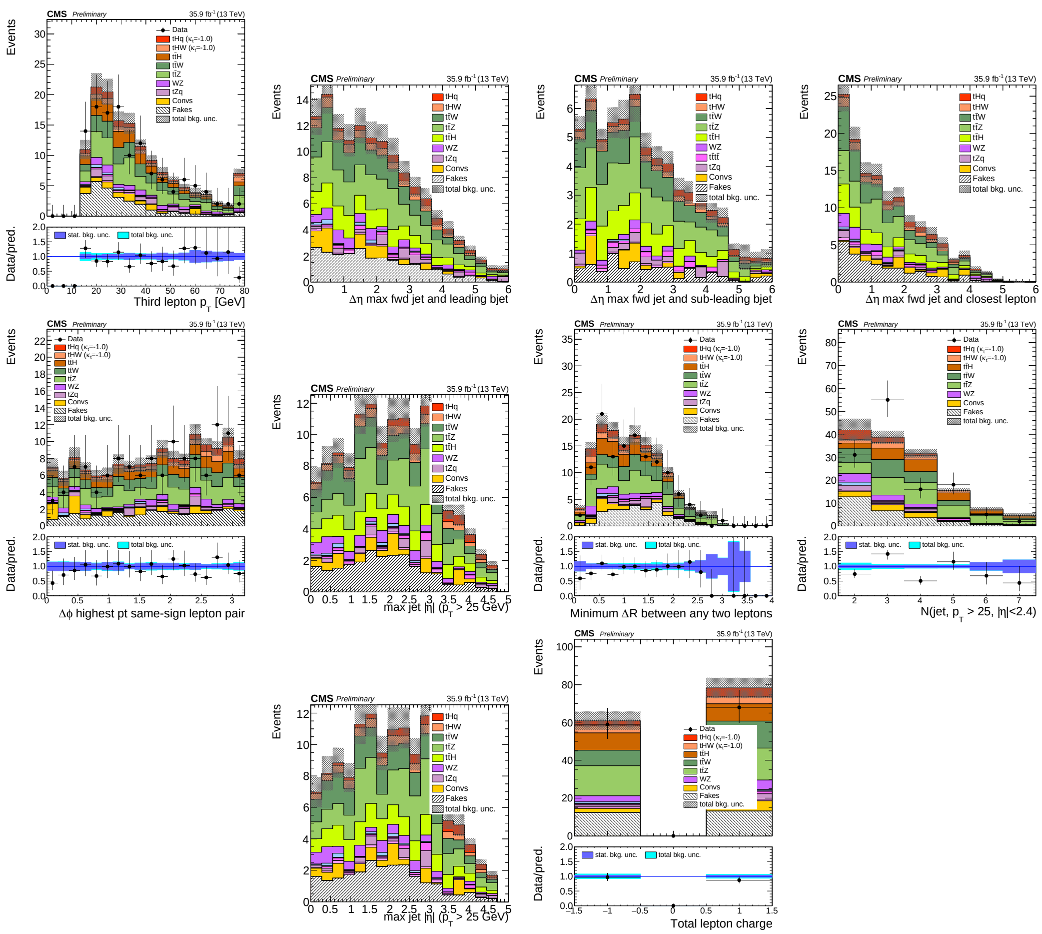

Figure 6.3: Distributions of input variables to the BDT for signal discrimination, three lepton channel, normalized to their cross section and to $35.9fb^{-1}$.

6.7 Signal discrimination

The tHq signal is separated from the main backgrounds using a boosted decision tree (BDT) classifier, trained on simulated signal and background events. A set of discriminating variables are given as input to the BDT which produces a output distribution maximizing the discrimination power. Table 6.9 lists the input variables used while Figures 6.4 show their distributions for the relevant signal and background samples, for the three lepton channel. Two BDT classifiers are trained for the two main backgrounds expected in the analysis: events with prompt leptons from $t\bar{t}W$ and $t\bar{t}Z$ (also referred to as $t\bar{t}$V), and events with non-prompt leptons from $t\bar{t}$. The datasets used in the training are the tHq signal (see Tab. 6.3), and LO MADGRAPH samples of $t\bar{t}W$ and $t\bar{t}Z$, in an admixture proportional to their respective cross sections (see Tab. 6.6).

Variable name	Description
nJet25	Number of jets with $p_T > 25$ GeV, $\|\eta\| < 2.4$
MaxEtaJet25	Maximum $\|\eta\|$ of any (non-CSV-loose) jet with $p_T > 25$ GeV
totCharge	Sum of lepton charges
nJetEta1	Number of jets with $\|\eta\| > 1.0$, non-CSV-loose
detaFwdJetBJet	$\Delta\eta$ between forward light jet and hardest CSV loose jet
detaFwdJet2BJet	$\Delta\eta$ between forward light jet and second hardest CSV loose jet (defaults to -1 in events with only one CSV loose jet)
detaFwdJetClosestLep	$\Delta\eta$ between forward light jet and closest lepton
dphiHighestPtSSPair	$\Delta\phi$ of highest p_T same-sign lepton pair
minDRll	minimum ΔR between any two leptons
Lep3Pt/Lep2Pt	p_T of the 3^{rd} lepton (2^{nd} for ss2l)

Table 6.9: MVA input discriminating variables

The MVA analysis consist of two stages: first a “training” where the MVA method is trained to discriminate between simulated signal and background events, then a “test” stage where the trained algorithm is used to classify different events from

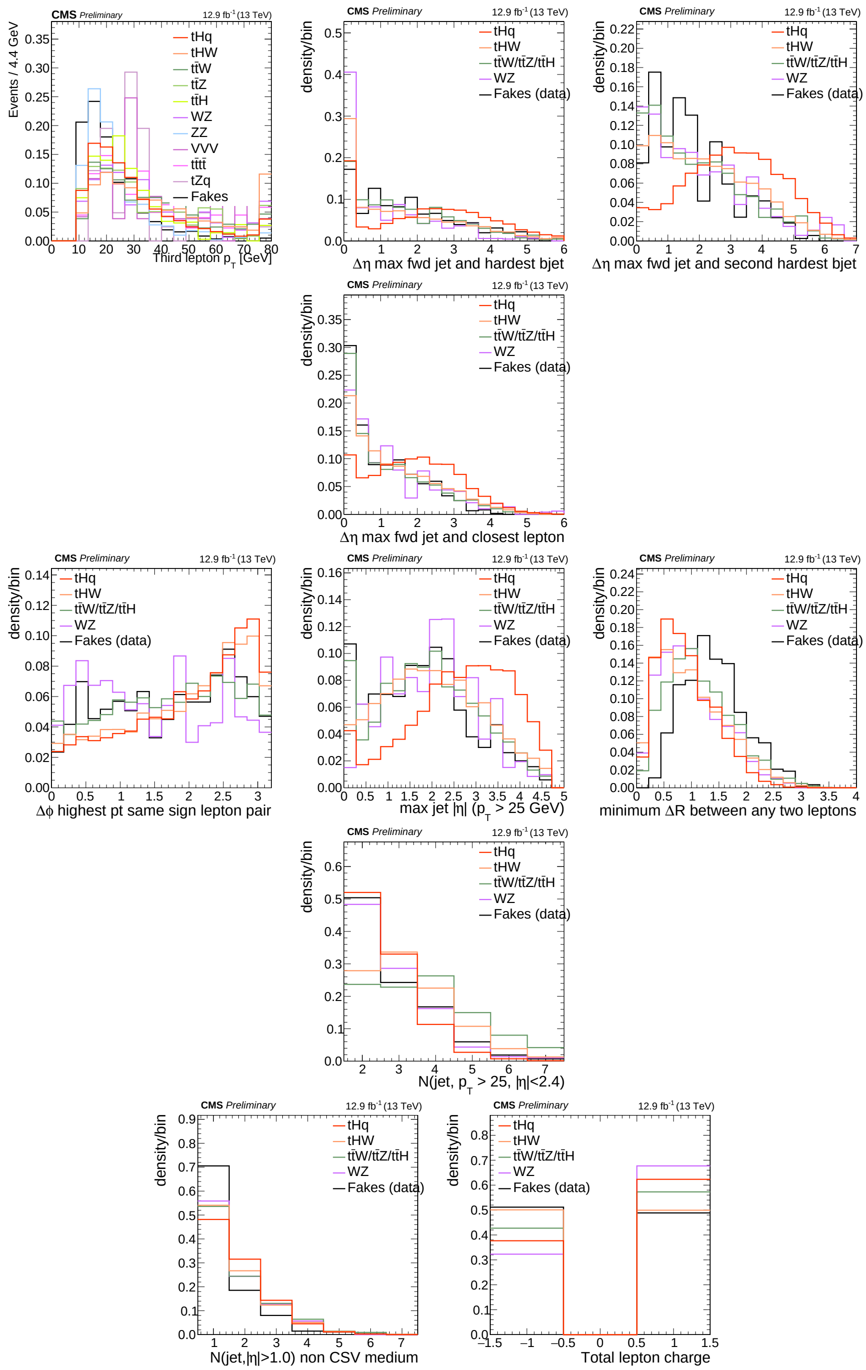

Figure 6.4: Distributions of input variables to the BDT for signal discrimination, three lepton channel.

the samples. The sample is obtained from a pre-selection (see Tab. **??** with pre-selection cuts). Figures 6.5 show the input variables distributions as seen by the

MVA algorithm. Note that in contrast to the distributions in Fig. 6.4 only the main backgrounds ($t\bar{t}$ from simulation, $t\bar{t}$V) are included.

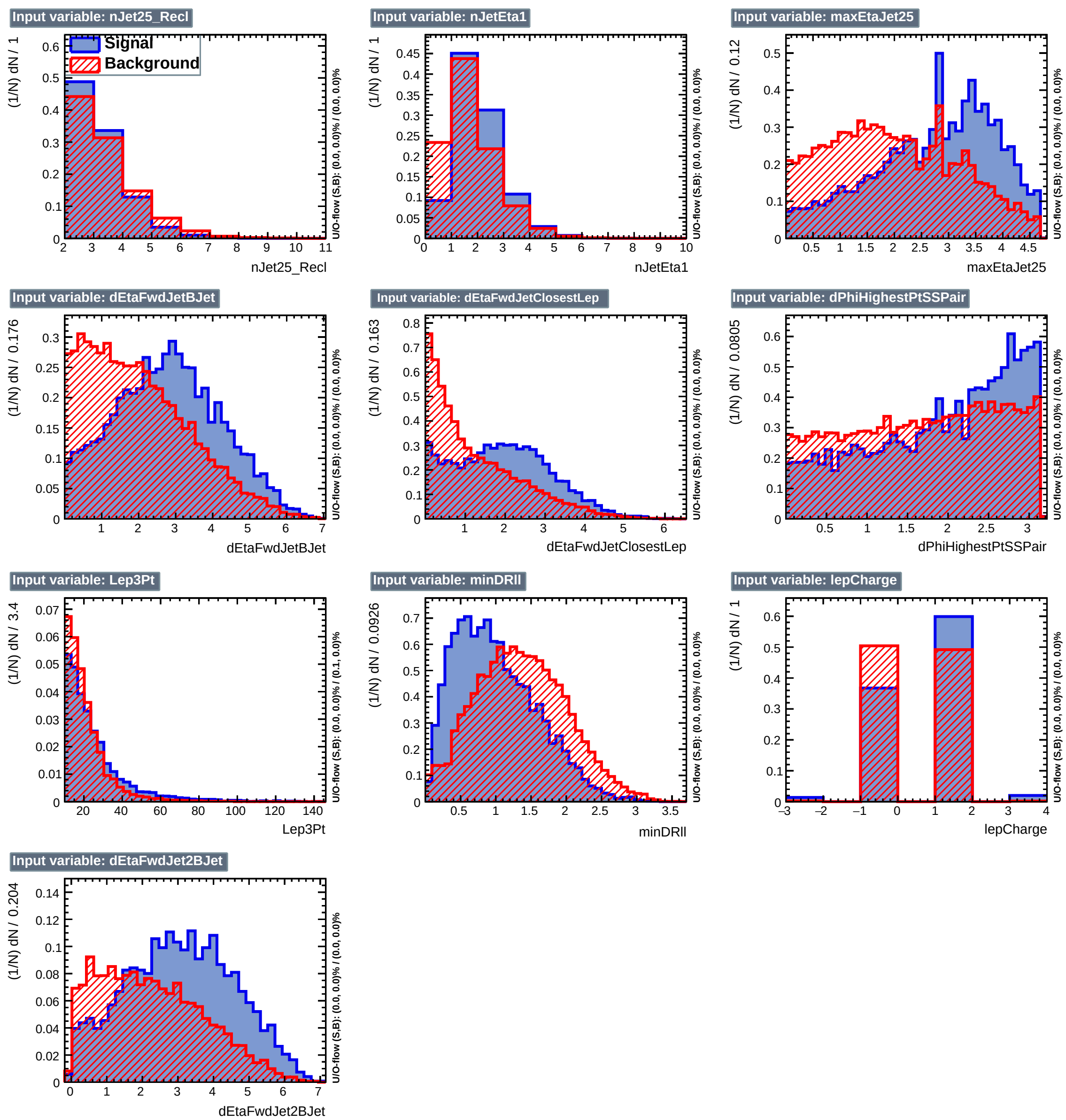

Figure 6.5: BDT inputs as seen by TMVA (signal, in blue, is tHq, background, in red, is $t\bar{t}$) for the three lepton channel, discriminated against $t\bar{t}$ (fakes) background.

Note that splitting the training in two groups reveals that some variables show opposite behavior for the two background sources; potentially screening the discrimi-

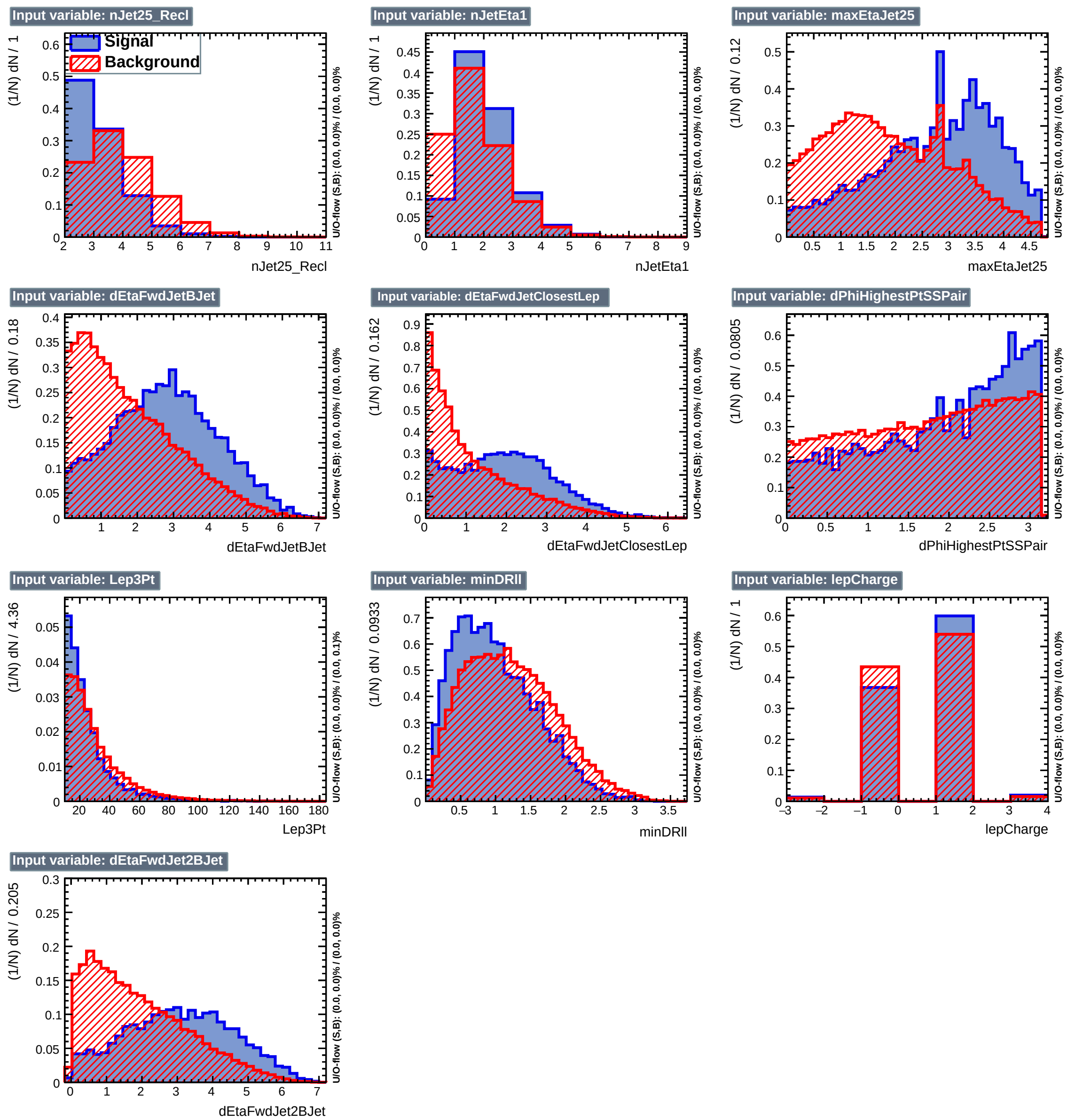

Figure 6.6: BDT inputs as seen by TMVA (signal, in blue, is tHq, background, in red, is $t\bar{t}W + t\bar{t}Z$) for the three lepton channel, discriminated against $t\bar{t}$V background.

nation power if they were to be used in a single discriminant. For some other variables the distributions are similar in both background cases.

From table 6.9, it is clear that the input variables are correlated to some extend. These correlations play an important role for some MVA methods like the Fisher discriminant method in which the first step consist of performing a linear transformation to an phase space where the correlations between variables are removed. In case a boosted decision tree (BDT) method however, correlations do not affect the performance. Figure 6.7 show the linear correlation coefficients for signal and background for the two training cases (the signal values are identical by construction). As expected, strong correlations appears for variables related to the forward jet activity. Same trend is seen in case of the same sign dilepton channel in Figure **??**.

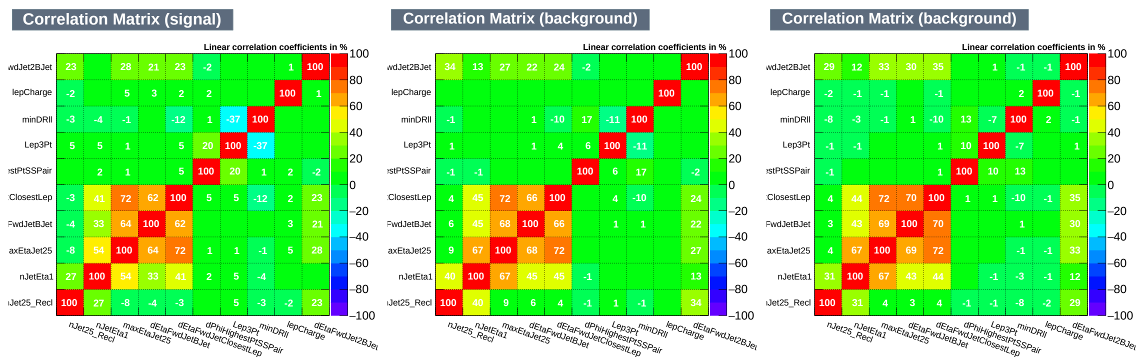

Figure 6.7: Signal (left), $t\bar{t}$ background (middle), and $t\bar{t}$V background (right.) correlation matrices for the input variables in the TMVA analysis for the three lepton channel.

6.7.1 Classifiers response

Several MVA algorithms were evaluated to determine the most appropriate method for this analysis. The plots in Fig. 6.8 (top) show the background rejection as a function of the signal efficiency for $t\bar{t}$ and $t\bar{t}$V trainings (ROC curves) for the different algorithms that were evaluated.

In both cases the gradient boosted decision tree ("BDTA_GRAD") classifier offers the best results, followed by an adaptive BDT classifier ("BDTA"). The BDTA_GRAD classifier output distributions for signal and backgrounds are shown on the bottom of Fig. 6.8. As expected, a good discrimination power is obtained using default discriminator parameter values, with minimal overtraining. TMVA provides a ranking of the input variables by their importance in the classification process, shown in Tab. 6.10.

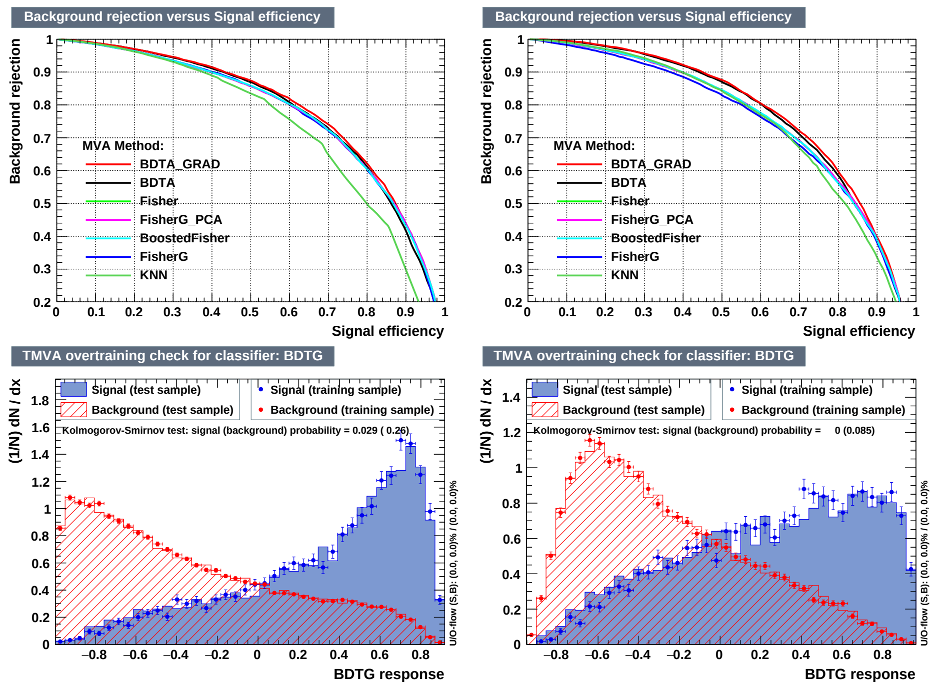

Figure 6.8: Top: background rejection vs signal efficiency (ROC curves) for various MVA classifiers (top) in the three lepton channel against $t\bar{t}$V (left) and $t\bar{t}$ (right). Bottom: classifier output distributions for the gradient boosted decision trees, for training against $t\bar{t}$V (left) and against $t\bar{t}$ (right).

	ttbar training		ttV training	
Rank	Variable	Importance	Variable	Importance
1	minDRll	1.329e-01	dEtaFwdJetBJet	1.264e-01
2	dEtaFwdJetClosestLep	1.294e-01	Lep3Pt	1.224e-01
3	dEtaFwdJetBJet	1.209e-01	maxEtaJet25	1.221e-01
4	dPhiHighestPtSSPair	1.192e-01	dEtaFwdJet2BJet	1.204e-01
5	Lep3Pt	1.158e-01	dEtaFwdJetClosestLep	1.177e-01
6	maxEtaJet25	1.121e-01	minDRll	1.143e-01
7	dEtaFwdJet2BJet	9.363e-02	dPhiHighestPtSSPair	9.777e-02
8	nJetEta1	6.730e-02	nJet25_Recl	9.034e-02
9	nJet25_Recl	6.178e-02	nJetEta1	4.749e-02
10	lepCharge	4.701e-02	lepCharge	4.116e-02

Table 6.10: TMVA input variables ranking for BDTA_GRAD method for the trainings in the three lepton channel. For both trainings the rankings show almost the same 5 variables in the first places.

The TMVA settings used in the BDT training are shown in Tab. 6.11.

`TMVA.Types.kBDT`
`NTrees=800`
`BoostType=Grad`
`Shrinkage=0.10`
`!UseBaggedGrad`
`nCuts=50`
`MaxDepth=3`
`NegWeightTreatment=PairNegWeightsGlobal`
`CreateMVAPdfs`

Table 6.11: TMVA configuration used in the BDT training.

6.8 Additional discriminating variables

Two additional discriminating variables were tested considering the fact that the forward jet in the background could come from the pileup; since we have a real forward jet in the signal, it could give some improvement in the discriminating power. The additional variables describe the forward jet momentum (fwdJetPt25) and the forward jet identification(fwdJetPUID). Distributions for these variables in the three lepton channel are shown in the figure 6.9. The forward jet identification distribution show that for both, signal and background, jets are mostly real jets.

The testing was made including in the MVA input one variable at a time, so we can evaluate the dicrimination power of each variable, and then both simultaneously. fwdJetPUID was ranked in the last place in importance (11) in both training (ttV and tt) while fwdJetPt25 was ranked 3 in the ttV training and 7 in the tt training. When training using 12 variables, fwdJetPt25 was ranked 5 and 7 in the ttV and tt trainings respectively, while fwdJetPUID was ranked 12 in both cases.

The improvement in the discrimination performance provided by the additional variables is about 1%, so it was decided not to include them in the procedure. Table 6.12 show the ROC-integral for all the testing cases we made.

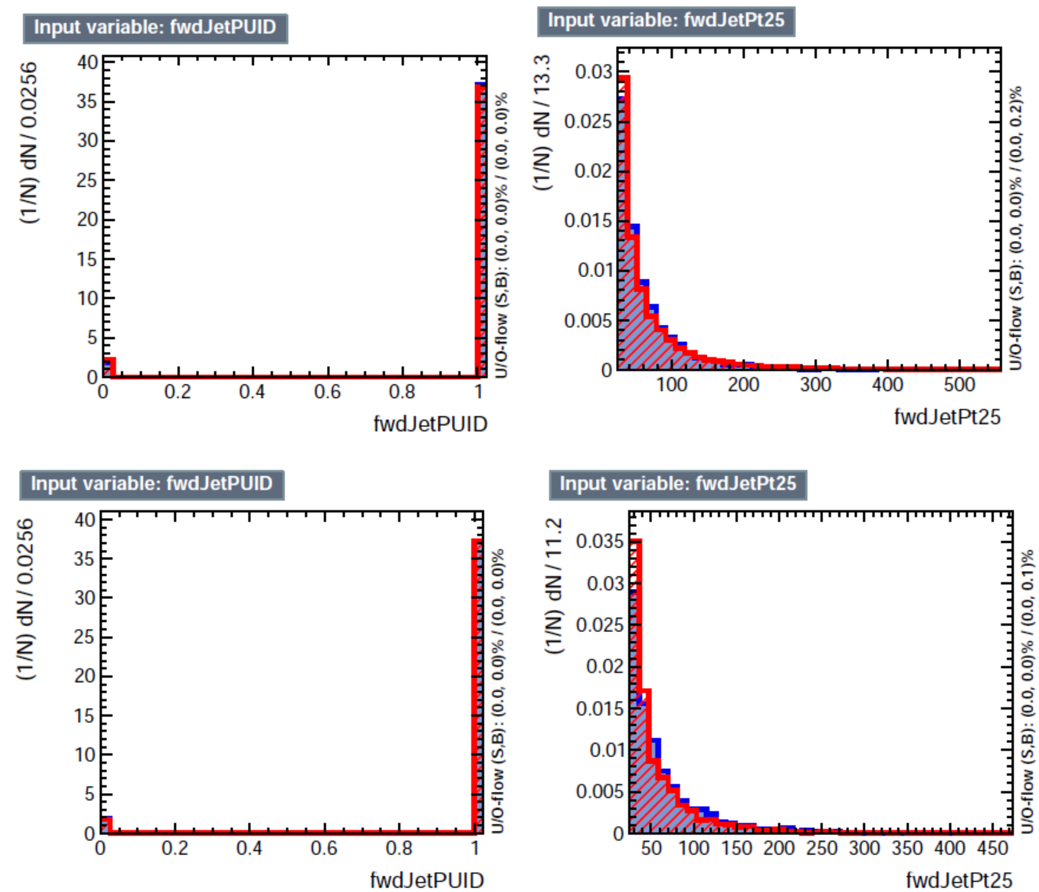

Figure 6.9: Additional discriminating variables distributions for ttv training(Top row) and tt training (bottom row) in the three lepton channel. The origin of the jets in the forward jet identification distribution is tagged as 0 for "pileup jets" while "real jets" are tagged as 1.

	ROC-integral
base 10 var ttv	0.848
+ fwdJetPUID ttv	0.849
+ fwdJetPt25 ttv	0.856
12 var ttv	0.856
base 10 var tt	0.777
+ fwdJetPUID tt	0.777
+ fwdJetPt25 tt	0.787
12 var	0.787

Table 6.12: ROC-integral for all the testing cases we made in the evaluation of the additional variables discriminating power. The improvement in the discrimination performance provided by the additional variables is about 1%

References

[1] J. Schwinger. “Quantum Electrodynamics. I. A Covariant Formulation”. Physical Review. 74 (10): 1439-61, (1948).

[2] R. P. Feynman. “Space-Time Approach to Quantum Electrodynamics”. Physical Review. 76 (6): 769-89, (1949).

[3] S. Tomonaga. “On a Relativistically Invariant Formulation of the Quantum Theory of Wave Fields”. Progress of Theoretical Physics. 1 (2): 27-42, (1946).

[4] D.J. Griffiths, “Introduction to electrodynamics”. 4th ed. Pearson, (2013).

[5] F. Mandl, G. Shaw. “Quantum field theory.” Chichester: Wiley (2009).

[6] F. Halzen, and A.D. Martin, “Quarks and leptons: An introductory course in modern particle physics”. New York: Wiley, (1984) .

[7] File: Standard_Model_of_Elementary_Particle_dark.svg. (2017, June 12) Wikimedia Commons, the free media repository. Retrieved November 27, 2017 from https://www.collegiate-advanced-electricity.com/single-post/2017/04/10/The-Standard-Model-of-Particle-Physics.

[8] E. Noether, “Invariante Variationsprobleme”, Nachrichten von der Gesellschaft der Wissenschaften zu Göttingen, mathematisch-physikalische Klasse, vol. 1918, pp. 235-257, (1918).

[9] C. Patrignani et al. (Particle Data Group), Chin. Phys. C, 40, 100001 (2016) and 2017 update.

[10] M. Goldhaber, L. Grodzins, A.W. Sunyar “Helicity of Neutrinos”, Phys. Rev. 109, 1015 (1958).

[11] Palanque-Delabrouille N et al. “Neutrino masses and cosmology with Lyman-alpha forest power spectrum”, JCAP 11 011 (2015).

[12] M. Gell-Mann. “A Schematic Model of Baryons and Mesons”. Physics Letters. 8 (3): 214-215 (1964).

[13] G. Zweig. “An SU(3) Model for Strong Interaction Symmetry and its Breaking” (PDF). CERN Report No.8182/TH.401 (1964).

[14] G. Zweig. “An SU(3) Model for Strong Interaction Symmetry and its Breaking: II” (PDF). CERN Report No.8419/TH.412(1964).

[15] M. Gell-Mann. “The Interpretation of the New Particles as Displaced Charged Multiplets”. Il Nuovo Cimento 4: 848. (1956).

[16] T. Nakano, K, Nishijima. “Charge Independence for V-particles”. Progress of Theoretical Physics 10 (5): 581-582. (1953).

[17] N. Cabibbo, “Unitary symmetry and leptonic decays” Physical Review Letters, vol. 10, no. 12, p. 531, (1963).

[18] M.Kobayashi, T.Maskawa, “CP-violation in the renormalizable theory of weak interaction,” Progress of Theoretical Physics, vol. 49, no. 2, pp. 652-657, (1973).

[19] File: Weak Decay (flipped).svg. (2017, June 12). Wikimedia Commons, the free media repository. Retrieved November 27, 2017 from

https://commons.wikimedia.org/w/index.php?title=File:Weak_Decay_(flipped).svg&oldid=247498592.

[20] Georgia Tech University. Coupling Constants for the Fundamental Forces(2005). Retrieved January 10, 2018, from http://hyperphysics.phy-astr.gsu.edu/hbase/Forces/couple.html#c2

[21] M. Strassler. (May 31, 2013).The Strengths of the Known Forces. Retrieved January 10, 2018, from https://profmattstrassler.com/articles-and-posts/particle-physics-basics/the-known-forces-of-nature/the-strength-of-the-known-forces/

[22] S.L. Glashow. "Partial symmetries of weak interactions", Nucl. Phys. 22 579-588, (1961).

[23] A. Salam, J.C. Ward. "Electromagnetic and weak interactions", Physics Letters 13 168-171, (1964).

[24] S. Weinberg, "A model of leptons", Physical Review Letters, vol. 19, no. 21, p. 1264, (1967).

[25] M. Peskin, D. Schroeder, "An introduction to quantum field theory". Perseus Books Publishing L.L.C., (1995).

[26] A. Pich. "The Standard Model of Electroweak Interactions" https://arxiv.org/abs/1201.0537

[27] F.Bellaiche. (2012, 2 September). "What's this Higgs boson anyway?". Retrieved from: https://www.quantum-bits.org/?p=233

[28] M. Endres et al. Nature 487, 454-458 (2012) doi:10.1038/nature11255

[29] F. Englert, R. Brout. “Broken Symmetry and the Mass of Gauge Vector Mesons”. Physical Review Letters. 13 (9): 321-23.(1964) doi:10.1103/PhysRevLett.13.321

[30] P.Higgs. “Broken Symmetries and the Masses of Gauge Bosons”. Physical Review Letters. 13 (16): 508-509,(1964). doi:10.1103/PhysRevLett.13.508.

[31] G.Guralnik, C.R. Hagen and T.W.B. Kibble. “Global Conservation Laws and Massless Particles”. Physical Review Letters. 13 (20): 585-587, (1964). doi:10.1103/PhysRevLett.13.585.

[32] CMS collaboration. “Observation of a new boson at a mass of 125 GeV with the CMS experiment at the LHC”. Physics Letters B. 716 (1): 30-61 (2012). arXiv:1207.7235. doi:10.1016/j.physletb.2012.08.021

[33] ATLAS collaboration. “Observation of a New Particle in the Search for the Standard Model Higgs Boson with the ATLAS Detector at the LHC”. Physics Letters B. 716 (1): 1-29 (2012). arXiv:1207.7214. doi:10.1016/j.physletb.2012.08.020.

[34] ATLAS collaboration; CMS collaboration (26 March 2015). “Combined Measurement of the Higgs Boson Mass in pp Collisions at âĹŽs=7 and 8 TeV with the ATLAS and CMS Experiments”. Physical Review Letters. 114 (19): 191803. arXiv:1503.07589. doi:10.1103/PhysRevLett.114.191803.

[35] LHC InternationalMasterclasses“When protons collide”. Retrieved from `http://atlas.physicsmasterclasses.org/en/zpath_protoncollisions.htm`

[36] CMS Collaboration, “SM Higgs Branching Ratios and Total Decay Widths (update in CERN Report4 2016)”. `https://twiki.cern.ch/twiki/bin/view/LHCPhysics/CERNYellowReportPageBR` , last accessed on 17.12.2017.

[37] R.Grant V. "Determination of Higgs branching ratios in $H \to W^+W^- \to l\nu jj$ and $H \to ZZ \to l^+l^-jj$ channels". Physics Department, University of Tennessee (Dated: October 31, 2012). Retrieved from http://aesop.phys.utk.edu/ph611/2012/projects/Riley.pdf

[38] LHC Higgs Cross Section Working Group, Denner, A., Heinemeyer, S. et al. "Standard model Higgs-boson branching ratios with uncertainties". Eur. Phys. J. C (2011) 71: 1753. https://doi.org/10.1140/epjc/s10052-011-1753-8

[39] F. Maltoni, K. Paul, T. Stelzer, and S. Willenbrock, "Associated production of Higgs and single top at hadron colliders", Phys.Rev. D64 (2001) 094023, [hep-ph/0106293].

[40] S. Biswas, E. Gabrielli, F. Margaroli, and B. Mele, "Direct constraints on the top-Higgs coupling from the 8 TeV LHC data," Journal of High Energy Physics, vol. 07, p. 073, (2013).

[41] M. Farina, C. Grojean, F. Maltoni, E. Salvioni, and A. Thamm, "Lifting degeneracies in Higgs couplings using single top production in association with a Higgs boson," Journal of High Energy Physics, vol. 05, p. 022, (2013).

[42] T.M. Tait and C.-P. Yuan, "Single top quark production as a window to physics beyond the standard model", Phys. Rev. D 63 (2000) 014018 [hep-ph/0007298].

[43] F. Demartin, F. Maltoni, K. Mawatari, and M. Zaro, "Higgs production in association with a single top quark at the LHC," European Physical Journal C, vol. 75, p. 267, (2015).

[44] CMS Collaboration, “Modelling of the single top-quark production in association with the Higgs boson at 13 TeV.” https://twiki.cern.ch/twiki/bin/viewauth/CMS/SingleTopHiggsGeneration13TeV, last accessed on 16.01.2018.

[45] CMS Collaboration, “SM Higgs production cross sections at $\sqrt{s}$ = 13 TeV.” https://twiki.cern.ch/twiki/bin/view/LHCPhysics/CERNYellowReportPageAt13TeV, last accessed on 16.01.2018.

[46] S. Dawson, The effective W approximation, Nucl. Phys. B 249 (1985) 42.

[47] S. Biswas, E. Gabrielli and B. Mele, JHEP 1301 (2013) 088 [arXiv:1211.0499 [hep-ph]].

[48] F. Demartin, B. Maier, F. Maltoni, K. Mawatari, and M. Zaro, “tWH associated production at the LHC”, European Physical Journal C, vol. 77, p. 34, (2017). arXiv:1607.05862

[49] LHC Higgs Cross Section Working Group, “Handbook of LHC Higgs Cross Sections: 4.Deciphering the Nature of the Higgs Sector”, arXiv:1610.07922.

[50] J. Ellis, D. S. Hwang, K. Sakurai, and M. Takeuchi.“Disentangling Higgs-Top Couplings in Associated Production”, JHEP 1404 (2014) 004, [arXiv:1312.5736].

[51] CMS Collaboration, V. Khachatryan et al., “Precise determination of the mass of the Higgs boson and tests of compatibility of its couplings with the standard model predictions using proton collisions at 7 and 8 TeV,” arXiv:1412.8662.

[52] ATLAS Collaboration, G. Aad et al., “Updated coupling measurements of the Higgs boson with the ATLAS detector using up to 25 fbâĹŠ1 of proton-proton collision data”, ATLAS-CONF-2014-009.

[53] ATLAS and CMS Collaborations, “Measurements of the Higgs boson production and decay rates and constraints on its couplings from a combined ATLAS and CMS analysis of the LHC pp collision data at $\sqrt{s} = 7$ and 8 TeV,” (2016). CERN-EP-2016-100, ATLAS-HIGG-2015-07, CMS-HIG-15-002.

[54] File:Cern-accelerator-complex.svg. Wikimedia Commons, the free media repository. Retrieved January, 2018 from https://commons.wikimedia.org/wiki/File:Cern-accelerator-complex.svg

[55] J.L. Caron , “Layout of the LEP tunnel including future LHC infrastructures.”, (Nov, 1993). A C Collection. Legacy of AC. Pictures from 1992 to 2002. Retrieved from https://cds.cern.ch/record/841542

[56] M. Vretenar, “The radio-frequency quadrupole”. CERN Yellow Report CERN-2013-001, pp.207-223 DOI:10.5170/CERN-2013-001.207. arXiv:1303.6762

[57] L.Evans. P. Bryant (editors). “LHC Machine”. JINST 3 S08001 (2008).

[58] CERN Photographic Service.“Radio-frequency quadrupole, RFQ-1”, March 1983, CERN-AC-8303511. Retrieved from https://cds.cern.ch/record/615852.

[59] CERN Photographic Service “Animation of CERN’s accelerator network”, 14 October 2013. DOI: 10.17181/cds.1610170 Retrieved from https://videos.cern.ch/record/1610170

[60] C.Sutton. “Particle accelerator”.Encyclopedia Britannica. July 17, 2013. Retrieved from https://www.britannica.com/technology/particle-accelerator.

[61] L.Guiraud. “Installation of LHC cavity in vacuum tank.”. July 27 2000. CERN-AC-0007016. Retrieved from https://cds.cern.ch/record/41567.

[62] J.L. Caron, “Magnetic field induced by the LHC dipole’s superconducting coils”. March 1998. AC Collection. Legacy of AC. Pictures from 1992 to 2002. LHC-PHO-1998-325. Retrieved from https://cds.cern.ch/record/841511

[63] AC Team. “Diagram of an LHC dipole magnet”. June 1999. CERN-DI-9906025 retrieved from https://cds.cern.ch/record/40524.

[64] CMS Collaboration “Public CMS Luminosity Information”. https://twiki.cern.ch/twiki/bin/view/CMSPublic/LumiPublicResults#2016_proton_proton_13_TeV_collis, last accessed 24.01.2018

[65] J.L Caron. “LHC Layout” AC Collection. Legacy of AC. Pictures from 1992 to 2002. September 1997, LHC-PHO-1997-060. Retrieved from https://cds.cern.ch/record/841573.

[66] J.A. Coarasa. “The CMS Online Cluster:Setup, Operation and Maintenance of an Evolving Cluster”. ISGC 2012, 26 February - 2 March 2012, Academia Sinica, Taipei, Taiwan.

[67] CMS Collaboration. “The CMS experiment at the CERN LHC” JINST 3 S08004 (2008).

[68] CMS Collaboration. “CMS detector drawings 2012” CMS-PHO-GEN-2012-002. Retrieved from http://cds.cern.ch/record/1433717.

[69] R. Breedon. “View through the CMS detector during the cooldown of the solenoid on February 2006. CMS Collection”, February 2006, CMS-PHO-OREACH-2005-004, Retrieved from https://cds.cern.ch/record/930094.

[70] A. Dominguez et. al. “CMS Technical Design Report for the Pixel Detector Upgrade”, CERN-LHCC-2012-016. CMS-TDR-11.

[71] CMS Collaboration. “Description and performance of track and primary-vertex reconstruction with the CMS tracker,” Journal of Instrumentation, vol. 9, no. 10, p. P10009,(2014).

[72] CMS Collaboration and M. Brice. “Images of the CMS Tracker Inner Barrel”, November 2008, CMS-PHO-TRACKER-2008-002. Retrieved from https://cds.cern.ch/record/1431467.

[73] M. Weber. “The CMS tracker”. 6th international conference on hyperons, charm and beauty hadrons Chicago, June 28-July 3 2004.

[74] CMS Collaboration. “Projected Performance of an Upgraded CMS Detector at the LHC and HL-LHC: Contribution to the Snowmass Process”. Jul 26, 2013. arXiv:1307.7135

[75] L. Veillet. “End assembly of HB with EB rails and rotation inside SX ”,January 2002. CMS-PHO-HCAL-2002-002. Retrieved from https://cds.cern.ch/record/42594.

[76] J. Puerta-Pelayo.“First DT+RPC chambers installation round in the UX5 cavern.”. January 2007, CMS-PHO-OREACH-2007-001. Retrieved from https://cds.cern.ch/record/1019185

[77] X. Cid Vidal and R. Cid Manzano. “CMS Global Muon Trigger” web site: Taking a closer look at LHC. Retrieved from https://www.lhc-closer.es/taking_a_closer_look_at_lhc/0.lhc_trigger

[78] WLCG Project Office, “Documents & Reference - Tiers - Structure,” (2014). http://wlcg.web.cern.ch/documents-reference , last accessed on 30.01.2018.

[79] CMS Collaboration. "CMSSW Application Framework", https://twiki.cern.ch/twiki/bin/view/CMSPublic/WorkBookCMSSWFramework, last accesses 06.02.2018

[80] A. Buckleya, J. Butterworthb, S. Giesekec, et. al. "General-purpose event generators for LHC physics". arXiv:1101.2599v1 [hep-ph] 13 Jan 2011

[81] A. Quadt. "Top Quark Physics at Hadron Colliders". Advances in the Physics of Particles and Nuclei. Springer-Verlag Berlin Heidelberg. DOI: 10.1007/978-3-540-71060-8 (2007)

[82] DurhamHep Data Project, "The Durham HepData Project - PDF Plotter." http://hepdata.cedar.ac.uk/pdf/pdf3.html , last accessed on 02.02.2018.

[83] F. Maltoni, G. Ridolfi, and M. Ubiali, "b-initiated processes at the LHC: a reappraisal," Journal of High Energy Physics, vol. 07, p. 022, (2012).

[84] B. Andersson, G. Gustafson, G.Ingelman and T. Sjostrand, "Parton fragmentation and string dynamics", Physics Reports, Vol. 97, No. 2-3, pp. 31-145, 1983.

[85] CMS Collaboration, "Event generator tunes obtained from underlying event and multiparton scattering measurements;" European Physical Journal C, vol. 76, no. 3, p. 155, (2016).

[86] J. Alwall et. al., "The automated computation of tree-level and next-to-leading order differential cross sections, and their matching to parton shower simulations," Journal of High Energy Physics, vol. 07, p. 079, (2014).

[87] S. Frixione, P. Nason, and C. Oleari, "Matching NLO QCD computations with Parton Shower simulations: the POWHEG method," Journal of High Energy Physics, vol. 11, p. 070, (2007).

[88] S. Agostinelli et al., "GEANT4: A Simulation toolkit," Nuclear Instruments and Methods in Physics, vol. A506, pp. 250âĂŞ303, (2003).

[89] J.Allison et.al.,"Recent developments in Geant4", Nuclear Instruments and Methods in Physics Research A 835 (2016) 186-225.

[90] CMS Collaboration "Full Simulation Offline Guide", `https://twiki.cern.ch/twiki/bin/view/CMSPublic/SWGuideSimulation`, last accessed 04.02.2018

[91] A. Giammanco. "The Fast Simulation of the CMS Experiment" J. Phys.: Conf. Ser. 513 022012 (2014)

[92] A.M. Sirunyan et. al. "Particle-flow reconstruction and global event description with the CMS detector", JINST 12 P10003 (2017) `https://doi.org/10.1088/1748-0221/12/10/P10003`.

[93] The CMS Collaboration. " Description and performance of track and primary vertex reconstruction with the CMS tracker". JINST 9 P10009 (2014). doi:10.1088/1748-0221/9/10/P10009

[94] J. Incandela. "Status of the CMS SM Higgs Search" July 4, 2012. Pdf slides. Retrieved from `https://indico.cern.ch/event/197461/contributions/1478917/attachments/290954/406673/CMS_4July2012_Final.pdf`

[95] P. Billoir and S. Qian, "Simultaneous pattern recognition and track fitting by the Kalman filtering method", Nucl. Instrum. Meth. A 294 219. (1990).

[96] W. Adam, R. Fruhwirth, A. Strandlie and T. Todorov, "Reconstruction of electrons with the Gaussian sum filter in the CMS tracker at LHC", eConf C 0303241 (2003) TULT009 [physics/0306087].

[97] K. Rose, "Deterministic Annealing for Clustering, Compression, Classification, Regression and related Optimisation Problems", Proc. IEEE 86 (1998) 2210.

[98] R. Fruhwirth, W. Waltenberger and P. Vanlaer, " Adaptive Vertex Fitting", CMS Note 2007-008 (2007).

[99] CMS collaboration, "Performance of CMS muon reconstruction in pp collision events at $\sqrt{s} = 7$ TeV ", JINST 7 P10002 2012, [arXiv:1206.4071].

[100] M. Cacciari, G. P. Salam, and G. Soyez, "The anti-k_t jet clustering algorithm," Journal of High Energy Physics, vol. 04, p. 063, (2008).

[101] B. Dorney. "Anatomy of a Jet in CMS". Quantum Diaries. June 1st, 2011. Retrieved from https://www.quantumdiaries.org/2011/06/01/anatomy-of-a-jet-in-cms/

[102] The CMS Collaboration."Event Displays from the high-energy collisions at 7 TeV", May 2010, CMS-PHO-EVENTS-2010-007, Retrieved from https://cds.cern.ch/record/1429614.

[103] The CMS collaboration. "Determination of jet energy calibration and transverse momentum resolution in CMS". JINST 6 P11002 (2011). http://dx.doi.org/10.1088/1748-0221/6/11/P11002

[104] The CMS Collaboration, "Introduction to Jet Energy Corrections at CMS.". https://twiki.cern.ch/twiki/bin/view/CMS/IntroToJEC, last accessed 10.02.2018.

[105] CMS Collaboration Collaboration. “Identification of b quark jets at the CMS Experiment in the LHC Run 2”. Tech. rep. CMS-PAS-BTV-15-001. Geneva: CERN, (2016). https://cds.cern.ch/record/2138504.

[106] CMS Collaboration Collaboration. “Performance of missing energy reconstruction in 13 TeV pp collision data using the CMS detector”. Tech. rep. CMS-PAS-JME16-004. Geneva: CERN, 2016. https://cds.cern.ch/record/2205284.

[107] K. Skovpen. “Event displays highlighting the main properties of heavy flavour jets in the CMS Experiment”, Aug 2017, CMS-PHO-EVENTS-2017-006. Retrieved from https://cds.cern.ch/record/2280025.

[108] G. Cowan. “Topics in statistical data analysis for high-energy physics”. arXiv:1012.3589v1

[109] A. Hoecker et al., “TMVA-Toolkit for multivariate data analysis” arXiv:physics/0703039v5 (2009)

[110] L. Lista. “Statistical Methods for Data Analysis in Particle Physics”, 2nd ed. Springer International Publishing. (2017) https://dx.doi.org/10.1007/978-3-319-62840-0

[111] I. Antcheva et al., “ROOT-A C++ framework for petabyte data storage, statistical analysis and visualization ,” Computer Physics Communications, vol. 182, no. 6, pp. 1384âĂŞ1385, (2011).

[112] Y. Coadou. “Boosted decision trees”, ESIPAP, Archamps, 9 February 2016. Lecture. Retrieved from https://indico.cern.ch/event/472305/contributions/1982360/attachments/1224979/1792797/ESIPAP_MVA160208-BDT.pdf

[113] J.H. Friedman. "Greedy function approximation: A gradient boosting machine". Ann. Statist. Volume 29, Number 5 (2001), 1189-1232. https://projecteuclid.org/download/pdf_1/euclid.aos/1013203451.

[114] F. James, M. Roos, "MINUIT: Function minimization and error analysis". Cern Computer Centre Program Library, Geneve Long Write-up No. D506, 1989

[115] J. Neyman and E. S. Pearson, "On the problem of the most efficient tests of statistical hypotheses". Philosophical Transactions of the Royal Society of London. Series A, Containing Papers of a Mathematical or Physical Character. Vol. 231 (1933), pp. 289-337

[116] B. Hespel, F. Maltoni, and E. Vryonidou, "Higgs and Z boson associated production via gluon fusion in the SM and the 2HDM", JHEP 06 (2015) 065, doi:10.1007/JHEP06(2015)065, arXiv:1503.01656.

[117] ATLAS Collaboration, "Measurements of Higgs boson production and couplings in diboson final states with the ATLAS detector at the LHC", Phys. Lett. B726 (2013) 88âĂŞ119, doi:10.1016/j.physletb.2014.05.011,10.1016/j.physletb.2013.08.010, arXiv:1307.1427. [Erratum: Phys. Lett.B734,406(2014)].

[118] CMS Collaboration, "Search for the associated production of a Higgs boson with a single top quark in proton-proton collisions at $\sqrt{s} = 8$ TeV", JHEP 06 (2016) 177,doi:10.1007/JHEP06(2016)177, arXiv:1509.08159.

[119] B. Stieger, C. Jorda Lope et al., "Search for Associated Production of a Single Top Quark and a Higgs Boson in Leptonic Channels", CMS Analysis Note CMS AN-14-140, 2014.

[120] M. Peruzzi, C. Mueller, B. Stieger et al., “Search for ttH in multilepton final states at $\sqrt{s} = 13$ TeV”, CMS Analysis Note CMS AN-16-211, 2016.

[121] CMS Collaboration, “Search for H to bbar in association with a single top quark as a test of Higgs boson couplings at $\sqrt{s} = 13$ TeV”, CMS Physics Analysis Summary CMS-PAS-HIG-16-019, 2016.

[122] CMS Collaboration, “Search for production of a Higgs boson and a single top quark in multilepton final states in proton collisions at $\sqrt{s} = 13$ TeV”, CMS Physics Analysis Summary CMS-PAS-HIG-17-005, 2016.

[123] B. WG, “BtagRecommendation80XReReco”, February, 2017. `https://twiki.cern.ch/twiki/bin/view/CMS/BtagRecommendation80XReReco`.

[124] CMS Collaboration, “Identification of b quark jets at the CMS Experiment in the LHC Run 2”, CMS Physics Analysis Summary CMS-PAS-BTV-15-001, 2016.

[125] M. Peruzzi, F. Romeo, B. Stieger et al., “Search for ttH in multilepton final1 states at $\sqrt{s} = 13$ TeV”, CMS Analysis Note CMS AN-17-029, 2017.

[126] B. Maier, “SingleTopHiggProduction13TeV”, February, 2016. https://twiki.cern.ch/twiki/bin/viewauth/CMS/SingleTopHiggsGeneration13TeV.